

FINAL REPORT

ESO Contract: 47724/VLT/96/6384/MST

Feasibility study of seeing prevision using the MESO-NH meteorological model

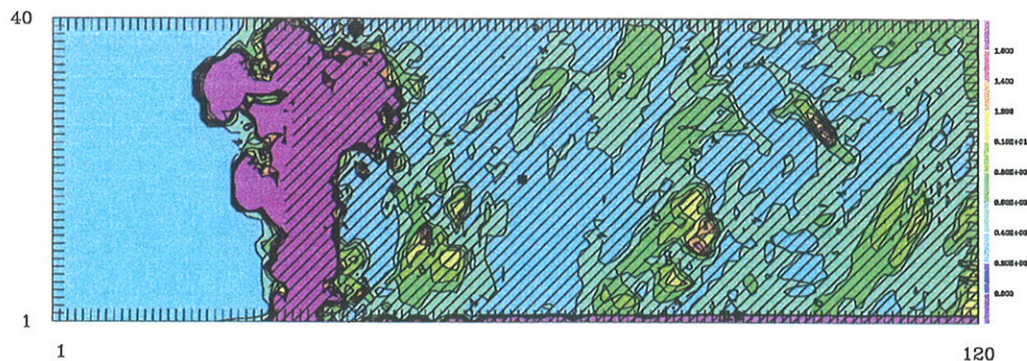
DECEMBER 1997

E. Masciadri *, J. Vernin *

P. Bougeault **

* *U.M.R. 6525 Astrophysique, Université de Nice - Sophia Antipolis, Parc
Valrose, 06108 Nice Cedex 2, France*

** *Centre National de Recherches Meteorologiques,
42, Av. G. Coriolis, 31057 Toulouse, France*



Contents

1	Introduction	6
1.1	Seeing forecast: a challenge for a modern ground-based astronomy . .	6
1.2	Feasibility study	10
1.3	Simulation principle	11
2	MESO-NH characteristics	11
2.1	General characteristics	11
2.2	Dynamical turbulence parameterization	12
2.3	Optical turbulence parameterization	14
2.4	Optical turbulence code for Astronomy	15
2.5	Technical informations	16
3	MESO-NH simulation	16
3.1	Pre-processing products	16
3.1.1	Orographic model	16
3.1.2	ECMWF analysis and Antofagasta radiosoundings	17
3.1.3	Initialization criterion	19
3.1.4	Spatio-temporal x,y,z,t initialization	19
3.1.5	Radiosounding reliability	20
3.2	Output products	21
3.2.1	Implementation of new astronomical parameters	21
3.2.2	Numeric outputs	22
3.2.3	Graphic outputs	23
4	Simulated nights	23
4.1	Nights selection	23
4.2	Analysis of PARSCA93 campaign	23
4.3	Statistical analysis Scidar/Meso-Nh	24
4.3.1	Method A	26
4.3.2	Method B	26
4.3.3	Signification of statistical estimators	27
4.3.4	Simulations calibration	28
5	Discussion	28
5.1	Statistical reliability	29
5.2	Adaptation time	30
5.3	Radiative transfer contribution	30
5.4	Optimization of the ECMWF product utilization	30
5.5	Simulation price	31
6	Conclusions and Perspectives	32
7	ACKNOWLEDGMENTS	34

In the Messenger of June 1996, A. Renzini in the article "The Early Universe with the VLT" wrote:

"...a large variety of observational capability is required to make progress in observational cosmology... ...and VLT instrumentation plan offers, in fact, the needed diversification. However, the explosion we are now witnessing thanks primarily to HST and Keck can only accelerate further as more 8-10 class telescopes come into line. Hence, tuning becomes essential. With progress being so fast, maintaining the schedule and deploying focal instruments in the shortest possible time is a top project...."

In the Messenger of December 1995, R. Giacconi Director General of ESO wrote in the editorial

"...the construction of large telescopes is a condition necessary but not sufficient to ensure the competitiveness of European astronomy. It is useless to build large telescopes, if we don't use them effectively. This implies the construction of forefront instrumentation and its proper use. A proper use includes: strategies for telescopes utilization, ranging from traditional modes to service and remote observing; scheduling of observation (both long and short term) to best utilize the seeing qualities of the site..."

List of Figures

1	Orographic model - 2000 x 2000 m resolution - 120 x 120 km	47
2	Orographic model - 500 m x 500 m resolution - 60 km x 60 km	48
3	Orographic model - 500 m x 500 m resolution - 60 km x 20 km	49
4	Orographic model - 1000 m x 1000 m resolution - 60 km x 20 km	49
5	Observing time at Antofagasta meteorologic station	50
6	Pre-processing namelist	51
7	Simulation namelist	52
8	Post-processing namelist	52
9	Radiosounding emagram - 26/5/93 - 12:00 T.U.	56
10	Analysis emagram - 26/5/93 - 12:00 U.T.	57
11	Wind direction correlations Antofagasta radiosoundings/ECMWF analyses	58
12	C_N^2 profile above Paranal obtained by radiosounding - 25/5/93 - Time: 30 min	58
13	C_N^2 profile above Paranal obtained by analysis - 25/5/93 - Time: 30 min	59
14	Initialization Emagram - 26/5/93	60
15	C_N^2 corrected profile above Paranal - 25/5/93 - Time 30 min	61
16	4 h time seeing evolution over Paranal on 25/5/93	62
17	4 h time seeing evolution over Paranal on 16/5/93	62
18	16/5/93 C_N^2 vertical profile above Paranal mountain after 4 h simulation time	63
19	26/5/93 4 h time seeing evolution above Paranal.	63
20	26/5/93 Potential temperature vertical profile over Paranal mountain at time t=0 sec	64
21	26/5/93 Potential temperature east-west vertical section across Paranal mountain after 30 min simulation time	64
22	26/5/93 Vertical wind fluctuations east-west vertical section across Paranal mountain after 30 min simulation time	65
23	26/5/93 Turbulent kinetic energy east-west vertical section across Paranal mountain after 30 min simulation time	65
24	26/5/93 Richardson number vertical profile over Paranal mountain after 30 min simulation time	66
25	26/5/93 Seeing east-west vertical section across Paranal mountain after 30 min simulation time	66
26	26/5/93 Seeing horizontal section over Paranal mountain after 30 min simulation time	67
27	26/5/93 Seeing east-west vertical section over Paranal mountain after (30 min + 19.37 sec)	67
28	26/5/93 4 h time seeing evolution over Paranal with initialize temperature profile modified	68
29	13/5/93 4 h time seeing evolution above Paranal.	68
30	13/5/93 Potential temperature vertical profile above Paranal mountain at time t=0 sec	69

31	13/5/93 Zonal wind vertical profile above Paranal mountain after 200 sec simulation time	69
32	13/5/93 Richardson number vertical profile above Paranal mountain after 200 sec simulation time	70
33	13/5/93 C_N^2 vertical profile above Paranal mountain after 30 min simulation time	70
34	13/5/93 Initialization emagram. Same as Fig.(9)	71
35	Horizontal seeing map - 14/5/93 - Simulation time: 4 h	72
36	Horizontal seeing map - 14/5/93 - Simulation time: 4 h	72
37	Horizontal seeing map - 16/5/93 - Simulation time: 4 h	73
38	Horizontal seeing map - 17/5/93 - Simulation time: 4 h	73
39	Horizontal seeing map - 18/5/93 - Simulation time: 4 h	74
40	Horizontal seeing map - 19/5/93 - Simulation time: 4 h	74
41	Horizontal seeing map - 23/5/93 - Simulation time: 4 h	75
42	Horizontal seeing map - 25/5/93 - Simulation time: 4 h	75
43	Time seeing evolution during the 14/5/93 night	76
44	Time seeing evolution during the 15/5/93 night	76
45	Time seeing evolution during the 16/5/93 night	77
46	Time seeing evolution during the 17/5/93 night	77
47	Time seeing evolution during the 18/5/93 night	78
48	Time seeing evolution during the 19/5/93 night	78
49	Time seeing evolution during the 23/5/93 night	79
50	Time seeing evolution during the 25/5/93 night	79
51	14/5/93 night: C_N^2 profiles comparison from Scidar and Meso-Nh . .	80
52	15/5/93 night: C_N^2 profiles comparison from Scidar and Meso-Nh . .	80
53	16/5/93 night: C_N^2 profiles comparison from Scidar and Meso-Nh . .	81
54	17/5/93 night: C_N^2 profiles comparison from Scidar and Meso-Nh . .	81
55	18/5/93 night: C_N^2 profiles comparison from Scidar and Meso-Nh . .	82
56	19/5/93 night: C_N^2 profiles comparison from Scidar and Meso-Nh . .	82
57	23/5/93 night: C_N^2 profiles comparison from Scidar and Meso-Nh . .	83
58	25/5/93 night: C_N^2 profiles comparison from Scidar and Meso-Nh . .	83
59	14/5/93 night - Initialize emagram.	84
60	14/5/93 night - Richardson number vertical profile over Paranal at time $t=0$	84
61	14/5/93 night - Richardson number vertical profile above Paranal at time $t=4$ h	85
62	15/5/93 night - Initialize emagram.	85
63	15/5/93 night. C_N^2 vertical profile at the first time step	86
64	23/5/93 night. Vertical wind fluctuations above Paranal mountain after 4 h simulation time	86
65	23/5/93 night. Wind intensity vertical profile over Paranal mountain after 4 h simulation time	87
66	PARSCA93 campaign - Seeing measurements from SCIDAR and ESO-DIMM	87
67	Statistical analysis following the Method A - Optimized time interval	88
68	Statistical analysis summary - Method B (I). Total seeing ε_{Tot}	90

69	Statistical analysis summary - method B (I). Boundary layer seeing ε_{BL}	90
70	Statistical analysis summary - method B (I). Free atmosphere seeing ε_{FA}	91
71	Statistical analysis summary - method B (II). Total seeing ε_{Tot}	91
72	Statistical analysis summary - method B (II). Boundary layer ε_{BL} . .	92
73	Statistical analysis summary - method B (II). Free Atmosphere Seeing	92
74	25/3/92 night.	93
75	16/5/93 night. Temporal seeing evolution over 4 h simulations time above the Paranal and mountain and the chilean coast.	93
76	Statistical analysis comparison between the forecast by persistence and the numeric method.	94
77	16/5/93 night. C_N^2 profiles comparison Scidar/Meso-Nh with $\beta = 1.81$	95
78	16/5/93 night. C_N^2 profiles comparison Scidar/Meso-Nh with $\beta = 2.86$	95
79	16/5/93 night. C_N^2 profiles comparison Scidar/Meso-nh with $\beta = 4.48$	95
80	16/5/93 Radiatif transfer simulation	96
81	Vertical east-west section of earth orography	96
82	Potential temperature profiles issued from ECMWF analysis extracted by different grid points	97
83	Absolute temperature profiles issued from ECMWF analysis extracted by different grid points	97
84	Price simulations	98

List of Tables

1	Real seeing nowcasting probability (%)	7
2	Real 'good' seeing nowcasting probability (%)	7
3	24-hour ahead statistical forecast of ground temperature	8
4	Data file names. <i>dd</i> refers to the day	23
5	Analysis of the 14/5 night	39
6	Analysis of the 15/5 night.	39
7	Analysis of the 16/5 night.	40
8	Analysis of the 17/5 night.	40
9	Analysis of the 18/5 night.	40
10	Analysis of the 19/5 night.	41
11	Analysis of the 23/5 night.	41
12	Analysis of the 25/5 night.	41
13	Analysis of the 14/5 night.	41
14	Analysis of the 15/5 night.	42
15	Analysis of the 16/5 night.	42
16	Analysis of the 17/5 night.	42
17	Analysis of the 18/5 night.	43
18	Analysis of the 19/5 night.	43
19	Analysis of the 23/5 night.	43
20	Analysis of the 25/5 night.	43

21	Orographic model resolution - Table of binary files	53
22	PARSCA93 campaign summary (I) - Antofagasta radiosoundings/ECMWF analyses	54
23	PARSCA93 campaign summary (II) - Antofagasta radiosoundings/ECMWF analyses	55
24	Wind intensity correlations Antofagasta radiosoundings/ECMWF anal- yses	57
25	Summary of the statistical analysis following the Method A	88
26	Statistical analysis summary following the Method B (I)	89
27	Statistical analysis summary following the Method B (II)	89

1 Introduction

1.1 Seeing forecast: a challenge for a modern ground-based astronomy

One of the most important problems for the ground astronomy is the limiting resolution of the image imposed by the atmospheric turbulence in addition to the limit imposed by the optical instrument. The large diameter of the new telescope generation increases the light collected by the instrument but it can not help to get a better spatial resolution in the image. The atmospheric turbulence modifies in a stochastic way the amplitude and the phase of the incoming wavefront and the images appear degraded. Different parameters are used to characterize the turbulence intensity in the atmosphere: the Fried's parameter r_0 , the seeing ϵ , the C_n^2 profiles, the outer scale \mathcal{L}_0 , the isoplanetic angles θ , the speckle boiling time τ_s and the wavefront coherence time τ_c . Each of these parameters have a relevance for particular astronomical applications. The outer scale \mathcal{L}_0 , for example, is fundamental for the Stellar Interferometry and, in general, for the large-ground-base Interferometry as soon as the baseline is of the order or larger than \mathcal{L}_0 . The isoplanetic angle θ is a critical parameter for the Adaptive Optics and the Laser Guide Star technic. The seeing is universally used to characterize the image quality [4] and it is defined as the width at the half height of a star image at the focus of a large diameter telescope. Actually, there are many reliable technic (direct and indirect) and instruments used to measure the seeing. We recall the DIMM [1], the SCIDAR[2],[3],[4] (optical measurements) and the instrumented balloons (*in situ* measurements). We know that these instruments are expensive, need a lot of mean-power, provide the relevant parameter in only one site or one line of sight and have no predicting capability. In order to overcome these restrictions, we propose to use a meteorological model coupled with a set of equations which links optical turbulence and the air flow. In the past, few attempts have been made in the study of seeing prevision but any experimented technic gave, singularly, exhaustive results. The reasons of this lack is principally due to the difficulty of the problem. The seeing value is correlated to meteorological parameters like the temperature, wind intensity and direction and to geophysical parameters like the orography. The problem is that the spatial and temporal fluctuation scales of the seeing are much smaller than the maximum resolution attained by typical meteorological forecasts. This is the reason why we often use the term "micro-meteorology" referring to the seeing or the optical turbulence in general.

We summarize, here, some of the most significant approaches provided by the literature.

- STATISTICAL TECHNIC

A multiple regression technic (nearest-neighbor regression) was applied to Paranal and La Silla sites in [5]. This technic is not a true prediction but rather a '*nowcasting*'. It tries to relate seeing measurements to meteorological and environmental conditions at the same time or in the near past. This technic gives interesting results for 24-hours temperature forecasting at ground

and one can have a prediction error smaller than 0.5 Celsius in 62% of cases. If the accuracy of prediction is relaxed to 2 Celsius, then a correct temperature forecast is obtained in 85% of cases. Beside that we know [7] that a 2 Celsius temperature difference between the telescope and the outside air is detrimental for observations at all wavelengths (local seeing greater than 1 arcsec in the visible). The main limit of this technic is that it can not forecast an abrupt temperature shift of 2 to 6 degrees in 24 hours, which occurs about 15% of the time at Paranal during the season studied. (89-90 Summer). For what concern the seeing nowcasting, the results obtained are interesting but some limitations are quoted hereafter. It was calculated, for example, that some particular combination of parameter values could give an estimation of ‘good’ seeing of about 93% but, on the other hand, the probability to have this particular combination is only 10%. Moreover, if we analyze how often one can make any prediction, that is how many times we have a set of meteorological configurations happening more than 4 times (i.e statistical reliable data) we find the following results at Paranal

Seasons	Real seeing nowcasting possibility (%)
Spring	38.8
Summer	46.5
Autumn	43.8
Winter	75.4

Table 1: Real seeing nowcasting probability (%) computed on the (1989-1991) period [5]

and if we are interested only in the probability to find ‘good’ seeing we have the following results:

Seasons	Real seeing nowcasting possibility (%)
Spring	12.5
Summer	8.9
Autumn	20.4
Winter	32.2

Table 2: Real ‘good’ seeing nowcasting probability (%) computed on the (1989-1991) period [5]

These results indicate that this technic can give an important support to the gestion of a modern telescope but it is not exhaustive.

- DYNAMICAL RECURRENT NEURAL NETWORKS TECHNIC

Dynamical recurrent neural networks were applied to astronomy prevision [6]. The principle of artificial neural networks is based on a great number of parallel interaction that reach an auto-adaptation in a dynamic and interactive way named 'apprentissage'. The advantage of dynamic recurrent neural networks when compared to a static one is that the first has a sort of inside memory that is the possibility to re-assimilate not only the recent data but also the data of the past. This potential advantage is contrasted with the realistic limit caused by a strong temporal discontinuity of the input data sequence. The results obtained with the technic are not particularly encouraging as shown in the Table.(3). The performances are similar to the forecast by persistence technic and clearly inferior to a nearest-neighbor technic.

Prediction error ($\circ C$)	≤ 2	≤ 1	≤ 0.5
Best Nearest Neighbor	84%	73%	62%
Best Neural Network	71 %	43%	22%
Forecast by persistence $t_n = t_{n-1}$	63%	36%	19%

Table 3: 24-hour ahead statistical forecast of ground temperature at each hour of the day: hit rate of nearest neighbor and neural network methods over 18000 observations corresponding to Summer 89-90 at Paranal. Nearest neighbor predictions were carried out on a 5-tuple set of the type $[t_{n-1}, t_{n-2}, t_{n-3}, p_{n-1}, p_{n-2}]$ [7]

- EMPIRICAL TECHNIC

In [8] the author analyses the relation between the seeing and the wind speed blowing at 200 hPa (10km about). The author assumes that the more rapid the wind at these altitude, the steeper the vertical wind gradient and thus the stronger the turbulence throughout the whole atmosphere. A good statistical correlation between the V_{200hPa} and the seeing was found at least in two observatories, Mauna Kea and La Silla [8]. The conclusion is that, statistically, sub-arcsec seeing might be encountered when the V_{200hPa} is less than 20 m/sec. A site located near the equator is, thus, potentially performant because the wind at this latitude and altitude is particularly low.

- PHYSICAL MODEL TECHNIC

In [11] the authors proposed a new approach based on the measurements of the outer scale of turbulence. They show that, from the knowledge of the profile of the vertical gradient of the potential temperature, and assuming an universal behavior of the outer scale versus altitude, it was possible to deduce the vertical profile of the optical turbulence C_N^2 . This model was first applied to seeing prevision [9], [10]. The last authors found a good agreement from

a statistical point of view, between simultaneous seeing measurements and meteorological temperature balloon profiles but a poor correlation is noticed for night to night comparisons.

A different approach was tested by VanZandt [12],[13]. In the absence of any estimation of L_0 , the authors developed a stochastic model based on a statistical treatment of the atmospheric vertical 'fine structure'. It is well known that the vertical structure of the temperature, wind and C_N^2 varies on scales as small as 25-50 m that are not detected by the usual technic. The turbulence regime is describe by the Richardson number R_i , parameter that expresses the balance between the dynamic unstable flows and the stable shears. During the night time, the atmosphere is generally characterized by stable conditions ($R_i > 1/4$) and it is difficult to put into evidence dynamic instability generating the typical fine layers strongly stratified in the horizontal direction. The authors tried to represent the dynamic atmospheric balance with a statistical function. Instead of using the deterministic function (R_i), they introduced a probability density function depending on the two unstable and stable factors estimated on the basis of the known climatological data. This model was first used for astronomical purpose by [14] and leads to a poor correlation due to the lack of quantitative measurements of seeing at this time and to the boundary layer turbulence.

• METEOROLOGICAL MODELS

In a pioneering article in this domain [15], the author invited to undertake the way of the numerical modelisation. More recently, in [16], the authors implemented the hydrostatic numerical model PERIDOT to forecast the seeing above a French site (Mt. Lachens). The model had a 3 km x 3 km resolution and it was supported by the French radiosounding network, enabling a good initialization of the model. It gave satisfactory results but, anyway, some limitations can be quoted:

- 1) The simulations bring a lot of information but many discrepancies are still observed
- 2) The poor spatial correlation is probably due to a lack of resolution of the model
- 3) The model can discriminate between good and bad seeing but only on a qualitative way. The model has not been applied yet to a high quality site. The best sites in the word have a mean seeing value of [0.5 - 1] arcsec with a very small fluctuation range of about [0.4 - 1.5] arcsec. Can numerical models forecast such low values? Can they forecast seeing with such a high precision to discriminate values in such a little range?

In our opinion, the above mentioned limitations are due to the fact that these meteorological models are hydrostatic models and they can make a significant error on the small scale component of the vertical velocity. It is true that in the most cases, over flat terrain, one can assume a pure horizontal flow (hydrostatic hypothesis). Good observatories are generally installed on the top of high mountains and local effects are expected since the horizontal flux hits steep slopes. At observatory altitudes, ranging mainly between 2000 and 4000 meters, one can find strong winds that induce

lee waves close to the summit and gravity waves can be encountered at higher altitudes, from say 5 to 15 km. It is known [17], [18], [20], [19] that optical turbulence is triggered by phenomena such as lee waves, gravity waves, jet stream on wind shear. Hence, it seems mandatory to us to discard the hydrostatic hypothesis and use non hydrostatic equations in the predicting model. Furthermore, many authors already noticed that most of the optical turbulence is concentrated in the boundary layer (the first kilometer). In order to well modelize this ground turbulence one will have to use both non-hydrostatic flow and fine horizontal grid size.

Why we should be interesting in seeing forecasting using a numeric technic?

SITE TESTING Find the best place to install the large modern generation telescopes (≥ 8 m) is fundamental to attain the best efficiency of a telescope. Beside an accurate climatology, and a nowcasting technic[5], a numerical simulation model could be an useful tool for site testing.

FLEXIBLE SCHEDULING As one can deduce reading the extracts in the front page of this report, the scientific potential of the new generation telescopes is measured not only by the performances of the instruments placed at the focus of the telescope but by their proper use. The optimization of the 'observing time programs' is mandatory to make competitive a telescope [21], [22],[7]. This justifies the interest for the subject. If a very good seeing is predicted in the next hours, an optimized management of the observatory might induce to place a High Angular Resolution instrument instead of a photometric one. Beside that, we must admit that this is not an easy goal: seeing measurements obtained during the past years campaigns show an average temporal variability of the order of few hours. We intend to evaluate if an optimized configuration of a numeric model could supply an help in nightly programming of telescope observing time.

"GLOBAL" OPTICAL TURBULENCE CHARACTERIZATION With a numerical technic we could obtain, for a given time t_0 , 3-D map of ALL the parameters characterizing the optical turbulence in a region around the telescope and we could estimate their values along different line of sight. This is the reason why it should be better to talk about an 'Optical Turbulence Forecast' instead of a simple 'Seeing Forecast'.

1.2 Feasibility study

This document is the final report of the ESO-DA-CNRM contract 47724/VLT/96/6384/MST: '*Seeing Prevision using the CNRM-LA Meso-Nh Meteorological Model*', the objective of which is to provide ESO with an assessment of the potential and limitations of seeing prediction in the context of a flexible operation mode for the VLT. In order to verify the technical feasibility, we intend to compare the model simulations with the optical measurements obtained during the PARSCA93 campaign at Paranal by the team of Nice University of J.Vernin and by M.Sarazin of ESO (contract VLT-TRE-UNI-17400-0001). During this campaign the seeing was assessed and C_N^2 profiles also. These profiles will be, thus compared to profiles issued by Meso-Nh profiles. To our knowledge, it is the first time that such a detailed com-

parison is intended. In a first phase of the study [23] we analyzed the most efficient configurations for an optimal exploitation of the numerical technic. Systematic analysis has been made of two nights of data obtained during the PARSCA93 campaign, comparing not only the seeing measurements, but also the C_N^2 profiles taken from the Scidar and from the Meso-Nh simulations. The seeing contributions from the boundary layer (BL) and from the free atmosphere (FA) were analyzed in order to study the model sensitivity to orographic effects. In the second phase we analyzed some problems not yet solved during the first one, such as the model adaptation time and the simulation duration, and we dedicated our efforts to a complete statistical analysis of the whole PARSCA93 campaign. We followed two different approaches to better characterize the model precision and sensibility (Chapter 4). Seeing contributions from the BL and the FA were computed for all the nights and at different simulation time ranging from 1 to 4 hours. A linear regression law was applied, after calibrating the model. Different kinds of statistical estimators were applied to study the efficiency of the numerical model. A final discussion is dedicated to the interpretation of the results. Final recommendations about the opportunity to use Meso-Nh model on an operational way will be given in order to fulfil the flexible scheduling requirements.

1.3 Simulation principle

The *principle of simulation* that we used is the following: We first initialize the numerical model with orographically unperturbed meteorological data provided by both Antofagasta station radiosoundings and ECMWF (European Center for Medium Weather Forecast) data analysis computed in the nearest grid point to the meteorological station. Both the station and the analysis grid point are located at north-west of the Paranal mount. Knowing that the wind blows prevalently in NW-SE direction, we can reasonably consider that the atmosphere above the Antofagasta station is unperturbed by orography. We consider, at the initial instant t_0 , a constant distribution of meteorological parameters over all the geographic surface analyzed by the numerical model. Then we simulate a selected realistic conditions introducing the orographic effects. After a lapse of time, the system converges to a stable condition or it oscillates around an equilibrium condition. We can finally compare simulation results with optical measurements (realized with a SCIDAR and DIMM techniques) related to a precise night, hour and for a selected time interval.

2 MESO-NH characteristics

2.1 General characteristics

The Meso-Nh Atmospheric Simulation System can simulate the time evolution of the atmospheric three dimensional motions ranging from the large meso-alpha scale (100km) down to the typical microscale of the Large Eddy Simulation (LES) models (50m). It can forecast several 3D meteorological variables: the three components of the wind, the temperature, the moisture, the pressure and the turbulence kinetic energy as detailed in Section 2.2. An optical turbulence scheme has been added later

and is sketched in Section 2.3 (seeing, C_N^2 profiles, isoplanetic angle and wavefront coherence time). Meso-Nh is a model [24] based on the Lipps and Hemler form of the anelastic approximation. The principal characteristic of this approximation is that all acoustic waves are filtered as in a standard hydrostatic model but nevertheless, the model can represent accurately the gravity waves responsible of the buoyancy dynamical instability in the atmosphere. The lee waves occurring downstream of the mountain ranges and resulting in flow deceleration are particularly well simulated by this model. These waves can perturb the flow and increase the level of the turbulence activity. We can deduce, so, that a high model resolution is a necessary but not sufficient element to improve the low atmosphere simulation.

Only a non-hydrostatic model can solve the orographic effects in the turbulence development and obtain a correct estimation of the turbulent kinetic energy because only such a model describes this physical phenomenon. The input data required by the model are:

- a numerical terrain model with high spatial resolution.
- the fields of atmospheric variables known at a initial time t_0 . One can use either analyses provided by Meteorologic Centers or radiosoundings provided by Meteorological Stations.

2.2 Dynamical turbulence parameterization

The basic dynamical equations of the model that allow to compute the time evolution of the physical system are the conservation of momentum (equations of motion), the first law of thermodynamics and the equations of dry-air-mass and moisture conservation. The turbulence is among the physical processes that occur at scales too small to be resolved by the model and so it must be correctly parameterized. Although the model offers a choice of 3D turbulent schemes, we used a 1D mode which takes into account the vertical turbulent fluxes only ¹. The method used to describe the turbulence production is described in [16] and [25]. It relies on the turbulence kinetic energy equation which takes the following form in Meso-Nh [26]:

$$\frac{De}{Dt} = -\overline{w'u'}\frac{\partial U}{\partial z} - \overline{w'v'}\frac{\partial V}{\partial z} - \frac{1}{\rho}\frac{\partial}{\partial z}(0.2\rho L\sqrt{e}\frac{\partial e}{\partial z}) - 0.7\frac{e^{\frac{3}{2}}}{L} + \beta\overline{w'\theta_v'} \quad (1)$$

where the first and second term on the right hand side represent the shear production, the third term the diffusion and the fourth term the dissipation contribution. The last term is the buoyancy term: w' is the vertical wind fluctuations, θ_v' the virtual potential temperature fluctuations and $\beta = \frac{g}{\theta_v}$ (g is the gravity acceleration). The vertical fluxes of wind and temperature are parameterized following the eddy diffusivity approach.

$$\overline{w'\theta_v'} = -K\frac{\partial\theta_v}{\partial z} \quad (2)$$

¹The turbulence scheme depends on the kind of mixing length definition selected. The C_N^2 can be parameterized in the atmosphere using the BL (Bougeault-Lacarrere) mixing length which is correlated to the choice of a 1D turbulence schema.

Some differences are noticed when compared to [16] work. We underline only the main one relevant to our application because it will introduce a modification in the optical turbulence parameterization as shown in the next paragraph. The eddy diffusivity is given by:

$$K(x, y, z, t) = 0.16L\sqrt{e}\phi_3(x, y, z, t) \quad (3)$$

where L is a mixing length and $\phi_3(x, y, z, t)$ is an inverse turbulent Prandtl number.

- L is the so called Bougeault-Lacarrere (BL89) [25] mixing length defined as follows: at any level z in the atmosphere a parcel of air of given internal energy $e(z)$, can move upwards (l_{up}) and downwards (l_{down}) before being stopped by buoyancy forces. These distances are defined by:

$$\int_z^{z+l_{up}} \frac{g}{\theta_v} \left(\theta_v(z) - \theta_v(z') \right) dz' = e(z) \quad (4)$$

and

$$\int_{z-l_{down}}^z \frac{g}{\theta_v} \left(\theta_v(z') - \theta_v(z) \right) dz' = e(z) \quad (5)$$

Bougeault and Lacarrere defined:

$$L = (l_{up}l_{down})^{1/2} \quad (6)$$

- ϕ_3 is a dimensionless function derived by [27]. It characterizes the thermal and dynamic stability of the atmosphere and takes into account the spatial variations of temperature and humidity. This is one of the element that permits a parameterization of the model at different scales motion. Its 3D analytical expression is given in [27]. It is a complex equation linked to the so called 'Redelsperger numbers' (dimensionless numbers characterizing the thermic and dynamic stability). In a dry 1D option we have a simpler analytical expression:

$$\phi_3(x, y, z, t) = \frac{1}{1 + C_1 \frac{L^2}{e} \frac{g}{\theta_v} \frac{\partial \theta_v}{\partial z}} \quad (7)$$

where $C_1 = 0.139$, and L is the mixing length.

$\frac{L^2}{e}$ behaves in a different way in a stable or unstable layer. In a very stable layer the mixing length is nearly equivalent to the Deardoff length

$$L = \sqrt{\frac{2e}{\frac{g}{\theta_v} \frac{\partial \theta_v}{\partial z}}} \quad (8)$$

and so $\phi_3 = 0.78$. In a very unstable layer ϕ_3 takes larger values and an upper bound is set as $\phi_3 = 2.2$

2.3 Optical turbulence parameterization

The Meso-Nh model has been adapted to simulate the optical atmospheric turbulence which is estimated by measuring the structure constant of the temperature fluctuations following [28], [29] and [15]:

$$C_T^2 = 1.6\varepsilon_\theta\varepsilon^{-1/3} \quad (9)$$

where ε_θ is the rate of temperature variance destruction by viscous processes and ε is the rate of energy dissipation related to the turbulence characteristic length and the energy by the Kolmogorov law

$$\varepsilon = 0.7 \frac{e^{3/2}}{L} \quad (10)$$

The ε_θ is governed by the theory of the turbulent mixing of a conservative passive additives. The potential temperature is a conservative parameter, that is it does not change when the sample volume is shifted about the space and it is passive because it does not affect the dynamic regime of the turbulence². This theory is based on the analogy between the velocity fluctuations in a turbulent flow and the concentration fluctuations of a conservative passive additive θ in a turbulent flow. It is based on a law that links the microscopic and the macroscopic physic parameters. The prognostic equation of the potential temperature variance $\overline{\theta'^2}$ in the turbulent energy budget is [29]:

$$\frac{\partial \overline{\theta'^2}}{\partial t} = -\frac{\partial \overline{w'\theta'^2}}{\partial z} - 2\overline{w'\theta'}\frac{\partial \overline{\theta}}{\partial z} - \varepsilon_\theta - \varepsilon_R \quad (11)$$

where ε_θ is the molecular dissipation, ε_R the radiative dissipation. Knowing that we can neglect the contributions from the triple correlations $\overline{w'\theta'^2}$ and the radiative dissipation we have

$$\frac{\partial \overline{\theta'^2}}{\partial t} = -2\overline{w'\theta'}\frac{\partial \overline{\theta}}{\partial z} - \varepsilon_\theta \quad (12)$$

The steady state balance equation for the rate of destruction of the variance leads to:

$$\varepsilon_\theta = -2\overline{w'\theta'}\frac{\partial \overline{\theta}}{\partial z} \quad (13)$$

If we substitute (13) and (10) into (9) using the equations presented in the last paragraph we obtain C_T^2 expressed as a function of macroscopic variables only

$$C_T^2 = 0.58\phi_3 L^{4/3} \left(\frac{\partial \overline{\theta}}{\partial z} \right)^2 \quad (14)$$

²The assumption that the temperature is passive is in general not true, since buoyancy forces are associated with the temperature inhomogeneities. In spite of this, for a given dynamical regime of turbulence, which already takes into account the action of the mean temperature profile, the fluctuating part of the temperature can be considered to be passive. [20]

Finally, the structure constant of the refraction index is obtained by the Gladston's law:

$$C_N^2 = \left(\frac{80 \cdot 10^{-6} P}{T^2} \right)^2 C_T^2 \quad (15)$$

2.4 Optical turbulence code for Astronomy

If in the last years the seeing was the universal accepted parameter used to characterize the site quality, today we know that, in order to reach the best performances of the adaptive optics techniques the knowledge of some other parameters such as the coherence wavefront time (τ_{AO}) and the isoplanetic angle (θ_{AO}) is fundamental. All these parameters are related to the refractive index fluctuations which appear inside the atmospheric turbulent layers. We summarize, in the following, the parameters which have been coded in the model. The Fried parameter r_0 is given by:

$$r_0 = \left[0.423 \left(\frac{2\pi}{\lambda} \right)^2 \int_0^\infty C_N^2(h) dh \right]^{-3/5} \quad (16)$$

The seeing ε is defined as the width at the half height of a star image at the focus of a large diameter telescope:

$$\varepsilon = 0.98 \frac{\lambda}{r_0} \quad (17)$$

where λ is the optical wavelength. As others authors we choose $\lambda = 0.5 \cdot 10^{-6} m$ for this study.

We also coded the isoplanetic angle θ_{AO} [30], [31] defined as the maximum angular separation of two stellar objects producing identical wavefronts at the telescope entrance pupil

$$\theta_{AO} = 0.31 \frac{r_0}{h_{AO}} \quad (18)$$

where

$$h_{AO} = \left[\frac{\int_0^\infty h^{5/3} C_N^2(h) dh}{\int_0^\infty C_N^2(h) dh} \right]^{3/5} \quad (19)$$

and the coherence wavefront time τ_{AO} [32]

$$\tau_{AO} = 0.31 \frac{r_0}{v_{AO}} \quad (20)$$

where

$$v_{AO} = \left[\frac{\int_0^{\infty} |v(h)|^{5/3} C_N^2(h) dh}{\int_0^{\infty} C_N^2(h) dh} \right]^{3/5} \quad (21)$$

2.5 Technical informations

The model was designed and developed jointly by the CNRM (Centre Nationale de la Recherches Meteorologique) and the Laboratoire d'Aerologie of Toulouse. It is currently used to simulate ideal or real phenomena. The time discretization is entirely explicit following the '*leap frog*' method. The source codes are written in standard **Fortran 90**, the source file management is performed by the standard **UNIX** file manager **SCCS**, and the procedures are written in standard **UNIX Korn-Shell**. To prepare and run a numerical simulation with the Meso-Nh model one must manipulate some Unix scripts and use a specific set of procedures. The main phases of a complete numerical experiment require a preparation of the simulation running, the simulation itself, and a post-processing phase. These are described in greater details in Annex 1. The model has been written in order to provide an usufull research tool. It can be installed on other informatic stations (not necessary a Cray station) and used by non commercial institutions for research purposes.

3 MESO-NH simulation

3.1 Pre-processing products

The first step, in the initialization phase, consists in selecting and formatting radiosoundings and analysis data into the form needed by the Meso-Nh. The values related to wind intensity and direction and temperature are introduced in a specific namelist. We provided data from the following sources:

- Codification of Antofagasta radiosoundings data (**PARSCA93**, 13-26/5/93) in the format requested by the numerical model namelist structure.
- Codification of ECMWF analysis data provided by the CRS4 center of Cagliari (Italy) for the same periods in the same format.
- Codification of physical simulation characteristics in the initialization name lists. (terrain roughness, sea temperature, vertical model logarithmic resolution, minimum kinetic energy).

3.1.1 Orographic model

The physiographic fields are implemented on the Meso-Nh physiographic grid using a specific procedure. With the help of a namelist the user enters the altitude values of the orographic model (digitized values on a rectangular matrix), the geographic

coordinates of the entire surface to be analyzed and the Meso-Nh horizontal resolution. A system procedure produces a binary file containing all of this information. The resulting physiographic fields, named **PGD** files, are stored on the Cray90.

Low resolution terrain model from GLOBE - 2000 m x 2000 m At the beginning of this contract, in order to learn how to use the Meso-Nh model, we used a PGD file extracted from GLOBE, covering a surface of 120 km x 120 km with an orographic resolution of 5 km and a Meso-Nh resolution of 2 km. The surface was centered on the Paranal mountain (70.40 W, 24.61 S). Too low turbulence levels were found using this model because the geographical position of Paranal was not well represented (Fig(1)) and the mountain height was lower than the real value due to sampling effect.

High resolution terrain model from contour map of Northern Chile - 500 m x 500 m As foreseen in the study contract, a higher resolution orographic model (500 m x 500 m) was provided by the DA (Departement d'Astrophysique) in Nice. ESO provided contour maps of the orography within a 50 km radius around the Paranal site, with a scale of 1:250 000, to be digitized under the responsibility of DA. A copy of the digitized file was delivered to ESO on magnetic tape in December 96. We produced, starting from this file, a set of different PGD files. In Table(21) we summarize the characteristics of the different files. In Fig(2), Fig(3) and Fig(4) we display the 2D map of the orographic model related to some of these files. As can be observed in Table(21), the last two files correspond to a reduced portion of the total available surface, while still preserving the general geographic structure of the region: a seaside surface to the west, a sharp mountain chain along the Chilean coast, a broad mountainous region which includes the peak of Paranal and a few higher mountains to the east of Paranal. To reduce the simulation computing time, we decided to use the latter two PGD files (PGDANDES9, PGDANDES10, see Table(21)) to make the final tests.

3.1.2 ECMWF analysis and Antofagasta radiosoundings

In order to summarize the global campaign characteristics we found helpful to prepare Table(22) and Table(23). Wind direction and amplitude, corresponding to four different pressure height levels, is described with arrows. The 200 mb pressure corresponds to the upper levels of the atmosphere (about 12km), i.e. the free atmosphere, whereas the 850 mb pressure corresponds to low levels influenced by heat energy transfer and orographic effects. We recall that the atmospheric pressure at the top of Paranal mountain is about 740 mb. We show measurements of Antofagasta radiosoundings at 12:00 U.T. and ECMWF analysis at 00:00 U.T., 06:00 U.T., 12:00 U.T. and 18:00 U.T.. In the second column we provide the mean seeing values of the corresponding nights measured by the SCIDAR. First, we note the lack of soundings on 20, 21, 22 and 24 of May. Radiosoundings were available only at 12:00 U.T. The Antofagasta station provides observations only once a day, instead of twice as usual in the standard procedure (12:00 U.T. and 00:00 U.T.). This can constitute a problem for the initialization phase of the Meso-Nh model. At 12:00 U.T. we are

at about two hours after the end of the night at Antofagasta station, i.e. the second part of the night as seen in Fig.(5). Throughout the whole campaign, the Scidar observations took place in the first part of the night that is between 00:00 U.T. and 05:30 U.T. corresponding to the unique double star available. This means that we do not have radiosoundings taken when the Scidar was operated. To make a simulation at 02:00 U.T., for example, we would need to make a temporal extrapolation of the initialization data. On the other hand, a large quantity of meteorological ECMWF data is available.

We now analyze more deeply the quality of radiosoundings and analysis data. This is an important aspect of the simulation procedure because initial conditions of low quality may produce erroneous simulation results. ECMWF analysis on (70.31 W, 23.62 S) grid point and radiosoundings from Antofagasta station (70.43 W, 23.43 S) were provided by ESO. In order to derive a better estimation of the differences between the radiosoundings and the ECMWF analysis data we produced the emagrams related to the two cases. An emagram is a thermodynamical diagram used for the graphical description of the atmosphere state. The MESO-NH model post-processing procedure can be used to output emagrams. As an example, in Fig.(9) we show, for the 26/5/93, the radiosoundings emagram at 12:00 U.T. and in Fig.(10) the analysis emagrams at the same hour. The pressure is reported on the y coordinates. The isothermic lines are inclined at 45 degrees and have a linear scale and the adiabatic lines are represented by dashed, bent, transverse lines.

These figures represent just two sample taken from our data, but after a complete analysis of the total campaign emagrams, we can make the following general remarks. The radiosounding temperature profile resolution is better than that provided by meteorological analysis. Moreover, the thermal inversion of low slabs is not detected in the analysis data whereas it appears in the radiosoundings. The temperature profiles given by radiosoundings in the higher layers do not reproduce the typical thermal inversion above the tropopause (at around 150 mb). A possible explanation of the low vertical resolution of the analysis data is that they are calculated at only 15 levels, this fact introduces an important averaging effect.

Another important aspect to consider in the context of the analysis quality is that, in the Paranal region, analysis data are strongly correlated to Antofagasta radiosounding quality. In fact, to obtain the analysis data, the meteorological exploitation centers (ECMWF or SCEM of Meteo France) use algorithms which interpolate available data such as radiosoundings, satellite and aircraft observations. In the interpolation process (see Annex 2), each observation data type is weighted with a varying factor related to the distance between the chosen grid point and the coordinate of the true observation and also to the quality of the observations. From our knowledge, the radiosounding measurements are the most reliable, and many problems are encountered by the Meteorological Centers when exploiting satellite observations. Clearly, the influence of observation measurement on the analysis is proportional to the distance between the grid point analyzed and the location of the observation. In the assimilation cycle of Arpege model by Meteo France, for example, the interpolation algorithm is based on a finite number of observations belonging to a circular surface with a radius of about 1000 km centered on the chosen grid point [33]. In this Chilean region the density of radiosounding stations is low, the nearest meteorological station

to Antofagasta being Quintero (71.53 W, 32.78 S) 920 km south to Antofagasta. We can suppose that the influence of Quintero measurements on the analysis of a grid point at only 20 km about from Antofagasta will not be significant even if all observations are considered in the assimilation cycle. Thus, the analysis rely strongly on the Antofagasta radiosoundings quality, and, as mentioned above, the temperature profile given by the analysis has a lower vertical resolution than that obtained by radiosoundings, due to a low spatial (vertical) and temporal resolution interpolation effect. On the other hand, as can be observed in Table(22) and Table(23), the intensity and wind directions, taken from radiosoundings and analysis at 12:00 U.T. are well correlated. We can find confirmation of these assessments in the conclusions quoted in the “Feasibility study of Meteorological prediction model for ESO observatories in Chile” - ESO contract number: VLT/TRE/CRS/174430002 final CRS4 report Fig.(24) and Fig.(11). Few discrepancies are found especially at low atmospheric levels.

3.1.3 Initialization criterion

What is the influence of erroneous measurements in radiosoundings and analysis on optical turbulence C_n^2 profiles? In Fig.(12) and in Fig.(13) are reported the C_N^2 profiles simulated over the Paranal mountain using the radiosounding (12:00 U.T.) and the analyses (00:00 U.T.) on 25/5 night. The radiosounding is associated to a stronger turbulence level than the analysis. One can observe that the C_n^2 deduced from the radiosounding gives low turbulence at high atmospheric levels due to the missing thermic inversion above the tropopause. How to choose the best initialization criterion ? The model must be fed by wind and temperature profiles which best represent the atmospheric behavior at this latitude, in term of thermodynamic equilibrium. For this reason, considering the poor quality of analysis data we had, we thought that the best solution was to mix both the radiosoundings and the analyses:

We used the radiosounding temperature profile between 1000 *mb* and 150 *mb* and the analysis above 150 *mb*.

In Fig.(14) we show the result of such a mixing between radiosounding and analysis. In this way, we hope to preserve the best vertical resolution of the information. Knowing that the orographic effects are particularly sensitive to the wind, we used in the low part of the atmosphere (1000 *mb* – 750 *mb*), the analysis wind direction and intensity at 00:00 U.T., that is the nearest temporal wind data in this region of the atmosphere. In Fig.(15) one can observe the simulated C_N^2 profile obtained with these corrections.

In Annex 4 we report a summary of the meteorological parameters (T, P, U) used for the all night simulations.

3.1.4 Spatio-temporal x,y,z,t initialization

Simulation time

Before starting the analysis of the whole PARSCA93 campaign we performed a test on the simulation time necessary to adapt the flow to the orography and to

converge to a steady state. At the end of the first phase of this feasibility study the model never attained stationary conditions after 1^h30 min simulation time. We thus decided to make longer simulations. In Fig.(16) and Fig.(17) the seeing evolution time over the Paranal is represented. In Fig.(16), after about 1 hour, the seeing is oscillating around its mean value (0.7 *arcsec*). On the contrary, in Fig.(17), the seeing seems stable and, suddenly, increases to up 2 *arcsec* after 9000 and 14000 sec, with a more chaotic trend. On this night, the strong degradation of the seeing is associated to the apparition of a turbulent layer at 4 km as one can see on Fig.(18). This is why the comparison between Scidar and the model was so poor after the first phase report. The seeing ratio between the best and the worst night for the Scidar measurements is

$$\left(\frac{\varepsilon_{16}}{\varepsilon_{25}}\right)_{SCI} = 3.6 \quad (22)$$

After 1^h 30 min (first phase report), the same ratio for the model was **1.35**, but after 4^h simulation it rises to **3.8** very close to the Scidar measurements (as one can deduce from Table(7) and Table(12)). This correct discrimination, made by the model, of the turbulent energetic rate between the best and the worst nights attests a good sensitivity of the model and, for this reason, we decided to make 4^h simulation for all the nights.

Sampling time

We used, for the all simulations, a sampling time $t_s = 2.5$ sec, found to be necessary to make correct simulations.

Horizontal resolution and range

We used the PGDANDES9 orographic binary file. As indicated in the Table(21) we analyzed 60 x 20 km around the Paranal mountain with an horizontal resolution of 500 m.

Vertical resolution and range

The vertical resolution used is the following:

50 m for the first vertical mesh

- between the heights of **50 m** and **3 km**, logarithmic intervals are used (**30%** stretching), the last corresponding to a resolution of **600 m**
- between **3 km** and **20 km** we used a constant value of **600 m**

The choice of logarithmic stretching for the lower grid points was made to save computing time, preserving maximum resolution where the effects of orography are the most important and the development of turbulent eddies is the most efficient. The atmosphere is thus sampled on 40 levels with vertical resolution ranging from 50 near the ground to 600 m at high altitude.

3.1.5 Radiosounding reliability

In Section 3.1.2 we described the initialization criterion applied to initialize the model for the analysis of the whole PARSCA93. After analyzing the whole campaign we concluded that, in two occasions, an unrealistic radiosounding temperature profile

caused the generation of numerical instabilities. In Fig(19) we show the seeing time evolution over the Paranal during the 26/5/93 night. The seeing fluctuation is characterized by a precise high frequency ($\frac{1}{77.5}$ Hz) oscillation which has nothing to do with experimental seeing measurements performed yet. The seeing never reduced to a single frequency but, on the contrary, it is represented by a broad band frequency range [35]. A precise analysis of the simulation outputs of this night reveals the presence of a great production of dynamic turbulence triggered in a region of dynamic stability close to equilibrium ($\frac{\partial\theta}{\partial z} \sim 0$) extending over many hundred of meters. In Fig.(20) we show the θ profile at the initial time $t=0$. In Fig(21), Fig(22) and Fig(23) are represented a vertical section of the potential temperature, the vertical wind fluctuations and the turbulent kinetic energy after 30 min. In Fig(24) is reported the vertical profile of the Richardson number at the same time. At 10 km a negative value of the Richardson number stresses the developpement of dynamic turbulence, as seen in Fig.(23), generated by the gravity waves well visualized by the periodicity of the vertical wind fluctuations shown in Fig.(22).

Consequently the seeing is oscillating periodically as it is clearly visible in both vertical and horizontal sections obtained after 30 min S.T. shown in Fig(25) and section of seeing presented in Fig.(25) and that obtained after a 1/4 of the numerical fluctuation period. Comparing the two vertical sections, it is evident that minima and maxima are shifted by a 1/4 of period, which attests the horizontal displacement of the turbulent structure at 10 km.

To our knowledge a dynamic instability extending over some hundreds meters in the atmosphere has never been observed. We replaced, so, the radiosounding profile by the analysis one between 7.2 and 12 km and we started another simulation. As it is visible in Fig.(28), no oscillation is present. This clearly demonstrates that Antofagasta radiosounding might be partially wrong. As we told previously for two nights (26/5 and 13/5) the model generated numeric instabilities and the simulation outputs were rejected. We intend to give, now, a detail analysis of the numeric instabilities sources that affected the 13/5 night. In Fig.(29) one can observe the seeing time evolution over the Paranal mountain related to the 13/5 night. After 200 sec the model generated a dynamic instability caused by the presence of a null gradient ($\frac{\partial\theta}{\partial z} \sim 0$) of the potential temperature at 10.5 km as seen in Fig.(30). The presence of a strong wind gradient Fig.(31), coupled with a low potential temperature gradient induces a Richardson number $R_i < 0.25$ at this altitude as seen on Fig.(32). This is the origin of the development of an important C_N^2 layer at 10.5 km (Fig.(33)). In Fig.(34) we report the initialization radiosounding. One can note an extended region where $\frac{\partial\theta}{\partial z} \sim 0$ (absolute temperature parallel to the adiabatic lines) at about 10 km. This attests the hypothesis that a poor quality radiosounding might originate numeric instability.

3.2 Output products

3.2.1 Implementation of new astronomical parameters

During this feasibility study we added other fundamental astronomical parameters such as:

- the **Richardson number**: RICH

$$R = \frac{g}{\theta} \frac{\frac{\partial \theta}{\partial z}}{\left(\frac{\partial U}{\partial z}\right)^2} \quad (23)$$

- the **Wind intensity**: MODVIT
- the **Wavefront coherence time**: CHT (Section 2.4)
- the **Isoplanatic angle**: ISO (Section 2.4)

3.2.2 Numeric outputs

For each night, we provide the following numerical outputs of meteorological and astronomical parameters at 30min time intervals over a complete 4^h simulation:

West-East cut of integrated values over 80 grid points centered over the Paranal mountain

- Seeing
- Isoplanetic angle
- Wavefront coherence time

West-East cut of wind intensity over 80 grid points centered over the Paranal mountain

- Wind intensity

Vertical profiles over the following grid points: Sea-(5,19), Coast-(36,19), Paranal-(61,19)

- CN2
- Potential temperature: THT
- Zonal wind: UT
- Meridian wind: VT
- Wind intensity: MOD-VIT
- Richardson number: RICH
- Mixing length: LM
- Turbulent kinetic energy: TKET

- Redelsperger number: PHI3

The numeric values are stored into files named `ddd0n00m.dat` and `ddd0n00mh.dat`. *dd* means the day, *n* and *m* are integers used to identify different simulations. In the first kind of files are reported the vertical profile of the all variables reported in the previously lines and the integrated values over 80 grid points centered over the Paranal mountain. In the second kind of files is reported the wind intensity over 80 grid points centered over the same point.

For each simulation we recorded the seeing time evolution above the coast (36,16), and above the Paranal mountain (61,19). These values are issued during the simulation. This code modification allows a good sampling of the seeing ($t_s = 2.5$ sec). The numeric values are recorded in files `sddp.dat` and `sddc.dat`.

Geographic location	Grid Point	File name
Paranal	(61,19)	<code>sddp.dat</code>
Coast	(36,16)	<code>sddc.dat</code>

Table 4: Data file names. *dd* refers to the day

3.2.3 Graphic outputs

For each night analyzed, we report Fig.(35-42) an horizontal seeing map centered above the Paranal region.

4 Simulated nights

4.1 Nights selection

On the whole PARSCA93 campaign only eight nights among 14 have been selected. During the nights of 20/5, 21/5, 22/5 and 24/5 the Antofagasta Station did not provide any radiosounding. Nights of 13/5 and the 26/5 have been discarded because they give rise to numeric instabilities. The nights finally selected were the 14, 15, 16, 17, 18, 19, 23 and 25 May 1993. One can find, at the end of this report, all the meteorological parameters used to initialize the model at each night.

4.2 Analysis of PARSCA93 campaign

To make a complete campaign analysis we used two different approach to discuss simulations results. First, we analyzed the seeing evolution over a 4^h period with a 2.5 sec time step, as seen in Fig.(43) to Fig.(50). Four simulation hours are reported sampled using one time step ($t_s = 2.5$ sec).

Then, in order to realize a better estimation of the model reponse we analyzed the C_N^2 profiles simulated at 30 min, 1^h , 2^h , 3^h , 4^h interval time. From Fig.(51) to Fig.(58)

we report, for each night, a comparison between the C_N^2 profiles provided after 4^h simulation time and the C_N^2 profile measured by the Scidar. Not all the simulated profiles reproduce correctly the optical turbulence distribution in the atmosphere. We intend, in the next paragraph, to give a detail analysis of the nights in which some anomalies are present.

14/5 NIGHT: A strong turbulence production, not revealed by the Scidar measurements, is observed in the first hundred meters. This turbulence in excess is more likely caused by the initialization radiosounding of Fig.(59). One can observe that, at ground level, the typical thermic inversion of the potential temperature at these latitudes is not present. In Fig.(60) and Fig.(61) are reported the Richardson number profiles at the time $t=0$ and $t=4^h$. One can remark the presence of an instability region ($R_i \leq 0.25$) in the first hundred meters produced by the model.

15/5 NIGHT: The initialization radiosounding presents two regions of near-adiabacity at 400 and 300 mb Fig.(62). The vertical section of potential temperature at $t=0$, selected along the west-east direction over the Paranal, presents, at the same altitude, two unstable regions. Two important C_N^2 layers are produced by the model at the first simulation time steps Fig.(63) and we can find them along the 4^h simulation time interval. Comparing the Scidar and the simulated C_N^2 profiles Fig.(52), we deduce that probably these two layers are not realistic.

16/5 NIGHT: After 4^h simulation interval time, a good correlation is found between the Scidar measurements and the model simulations. It is well evident, in this case, that the model is sensitive to orographic effects producing the right turbulence rate at the ground level Fig.(53).

17/5 NIGHT: A good turbulence distribution is reproduced by the model throughout the whole atmosphere.

18/5 NIGHT: A rather good spatial vertical distribution of the rate of turbulence is produced by the model Fig.(55). One can remark a general underestimation of the turbulence at the ground level.

19/5 NIGHT: A good turbulence distribution is reproduced by the model on the whole atmosphere.

23/5 NIGHT: A turbulent layer is created by the model between 6000 and 7000 m after 4 h simulation. An important vertical wind fluctuations Fig.(64) and a strong wind gradient Fig.(65) induce a dynamic turbulent regime in this region.

25/5 NIGHT: A good spatial vertical distribution is reproduced by the model.

In the Annex 3 we report tables summarizing the turbulence atmospheric state (integrated C_N^2 and seeing values) related to each night.

4.3 Statistical analysis Scidar/Meso-Nh

In order to test the capacity of the MESO-NH model to predict the seeing, we assumed that the Scidar is a reference and we compared both seeings (Scidar and Meso-Nh) during each selected night. We are confident in this assumption because Scidar has been tested in many ways, in various sites and compared with others techniques such as DIMM and balloons. On Fig.(66) we plot the comparison of the seeing given by the ESO-DIMM and retrieved from the Scidar during PARSCA93 campaign. The mean seeing error between these two series of measurement is 0.15

arcsec. The standard deviation between both techniques is 0.10 arcsec which gives us a basis of discussion for the Meso-Nh/Scidar comparison. We recall here that the Scidar was working during 00:00 and 05:00 U.T. and simulations are initialized with radiosoundings taken at 12:00 U.T. In order to compare both techniques we decided to average all the Scidar measurements available during each night. Since we had no idea of the needed simulation time to achieve the best prediction we considered all the predictions ranging between 30 min and 4 hours. We followed two different approaches to make the statistical simulations analysis. Being aware that our statistical sample is poor (8 nights only) we tried to extract the most complete information with the available data using different technic. For both methods we realized a linear regression fit and we computed the following statistical estimators:

- **Correlation coefficient**

$$r = \frac{\sum_i x_i y_i}{\sqrt{\sum_i x_i^2 \sum_i y_i^2}} \quad (24)$$

where x_i and y_i are the seeing estimated with Scidar and Meso-Nh

- **Correlation coefficient for centered variables**

$$r_c = \frac{\sum_i (x_i - \bar{x})(y_i - \bar{y})}{\sqrt{\sum_i (x_i - \bar{x})^2 \sum_i (y_i - \bar{y})^2}} \quad (25)$$

This gives a more significant estimation of correlation because it is independent from the mean values which are always positive, like seeing.

- **Correlation coefficient estimation**

To estimate the correlation coefficient we computed the probability P that two uncorrelated distributions of the analysed data give a correlation coefficient greater than that observed. Among the tests found in different statistical books, we chose an algorithm adapted for a small number N of data. We considered the Student's distribution ³, denoted $A(t|\nu)$ defined as the probability, for ν degrees of freedom, that a certain statistic t would be smaller than the observed value if the mean were the same. The variable t is defined as

$$t = r_c \sqrt{\frac{N-2}{1-r_c^2}} \quad (26)$$

The probability P is defined as

$$P = 1 - A(t|\nu) \quad (27)$$

where $\nu = N - 2$

³For a more complete definition of the Student's function, we send the reader to *Numerical Recipes, Fortran version, pag.169*

- **Linear regression** between Scidar measurements and Meso-Nh simulations. We preferred the simplest linear adjustment $y = ax$, instead of $y = b + ax$ because there is no reason to admit a systematic error in the simulation procedure.
- **Standard deviation** σ between Scidar measurements and the regression straight line is computed following

$$\sigma^2 = \frac{1}{N-1} \sum_i (y_i - ax_i)^2 \quad (28)$$

4.3.1 Method A

We compare the seeing Scidar measurements with the Meso-Nh simulations above Paranal each 2.5 sec. In order to have a better estimation of the correct adaptation time, we compute all the statistical parameters previously described averaging the values over different time intervals. In Table(25) we report the statistical results obtained over 6 different time intervals over a complete 4^h S.T.: $[1^h - 2^h]$, $[1^h - 3^h]$, $[2^h - 3^h]$, $[1^h - 4^h]$, $[2^h - 4^h]$ and finally $[3^h - 4^h]$. The first 30 min are discarded because after this time, as we shall explain in the following chapter, the model it has not yet adapted to the terrain. This method has the advantage to give a good temporal statistics but it does not give informations about the vertical structure.

4.3.2 Method B

As we are interested not only on seeing prediction but also in turbulent profile prediction, for each night we compare the C_N^2 averaged profiles from the Scidar with that obtained from the Meso-Nh output each 30 min. Doing so, we can obtain the following double advantage: we can study the time C_N^2 profile evolution and we have directly access to the optical turbulence evolution at all the model levels. We splitted the atmosphere in two regions; for each night, we compute the contribution provided by the boundary layer (BL) defined here between ground level and 5 km and the free atmosphere (FA) above 5 km. The same splitting has been used for both Scidar and Meso-Nh. As we are not completely confident in the ability of the Scidar to measure the optical turbulence in the surface layer (first hundred of meters) nor the Meso-Nh model, we used two sets of Meso-Nh output, with and without the surface layer in order to evaluate the sensitivity of the numeric model to the orographic effect. We thus defined a ε_{BL} , a ε_{FA} and a ε_{TOT} in the following way

$$\varepsilon_{BL} = 5.30 \cdot \lambda^{-1/5} \left(\int_x^{5000} C_N^2(h) dh \right)^{3/5} \quad (29)$$

$$\varepsilon_{FA} = 5.30 \cdot \lambda^{-1/5} \left(\int_{5000}^{\infty} C_N^2(h) dh \right)^{3/5} \quad (30)$$

$$\varepsilon_{Tot} = 5.30 \cdot \lambda^{-1/5} \left(\int_x^\infty C_N^2(h) dh \right)^{3/5} \quad (31)$$

for $\lambda = 0.5 \cdot 10^{-6} \text{m}$.

- **B(I):** $x = 2676 \text{m}$, we take the vertical levels N [$3 \leq N \leq 40$] (without first 100 m)
- **B(II):** $x = 2560 \text{m}$, we take all the vertical levels N [$1 \leq N \leq 40$]

We underline that the ground level is 2560 m and not 2600 m (true Paranal altitude) for a clear average effect issued by the horizontal model resolution used.

The two slabs (BL and FA) correspond also to different sensitivity of the Scidar. This instrument is known to be much more sensitive to high altitude turbulence. This second method B is less statistically defined than the first one A. We can average, in fact, only 4 C_N^2 profiles for each night related to the 1^h , 2^h , 3^h and 4^h outputs, but we can analyze the model sensitivity on the first 100 m. In Table(26) and Table(27) are reported the statistical results for two different configurations. In the first one B(I) we reject the first 100 m. In the second one B(II) we take into account all the vertical levels. We estimated it was important to make this test because we often found that, a large C_N^2 layer was produced by the model at this low altitude. At the moment we have no *a priori* reason to reject or accept this contribution because we know that the Scidar sensitivity at this altitude is poor (only a Classic version of Scidar was employed during the PARSCA93 campaign).

4.3.3 Signification of statistical estimators

Having a small number of data, one needs to be careful with the interpretation of the statistical analysis. The correlation coefficient, in particular, requires some comments.

- The correlation coefficient is a poor estimator for deciding whether one observed correlation is statistically significant or not. The reason of this is that r_c tells how good is the fit to a straight line but ignoring of the individual distribution x_i and y_i .
- If we know that a perfect correlation is 1 and no correlation is 0, there is no universal criterion to discriminate between a good correlation coefficient and a bad one. One of the possible criterion to discriminate these values is to compute the probability P that two uncorrelated distributions x_i and y_i (belonging to the same parental distribution) give a correlation coefficient greater than that found. A large P means that r_c is poor, while a small P means that r_c is good. A classic test, adapted for a small data number, ($N < 20$) gives the results reported in the Tables(25) to (27). We know that, also in this case, the threshold over which we can consider the correlation coefficient to be bad is arbitrary.

We think, so, that the standard deviation of data from the linear regression line might estimate in a complementary way, the data dispersion around the optimized regression line. We report the values in Table(25)-(27). Finally, an alternative statistical estimator was applied. We considered a sample of random couple of points, corresponding to random independent Scidar and Meso-Nh seeing. We assume values comprised in the interval [0.2-1.5] simulating the seeing distribution between a minimum and a maximum value. Assuming a uniform distribution of this sample, we computed the standard deviation from the regression line obtained by the sample. This standard deviation represents a typical value for a couple of uncorrelated serie of measurements. We obtained a mean value $\overline{\sigma_u} = 0.5$ and a standard deviation $\sigma_{\sigma_u} = \sigma^* = 0.02$. Looking at the Tables(25) and (27) one can observe that the standard deviations σ for the total seeing ϵ_{Tot} are 0.49 and 0.54 which correspond, respectively, to $1\sigma^*$ and $2\sigma^*$ of the random points distribuion.

4.3.4 Simulations calibration

In both methods A and B we make a calibration of the Meso-Nh outputs using the following procedure. We compute the mean value of Scidar seeing measured $\langle \epsilon_{SCI} \rangle$ and the Meso-Nh simulated seeing $\langle \epsilon_{MNH} \rangle$. All the simulated values are multiplied by the calibration coefficient $\alpha = \frac{\langle \epsilon_{SCI} \rangle}{\langle \epsilon_{MNH} \rangle}$, before doing any statistical analysis as described in method A and B.

5 Discussion

We intend to give now the results interpretation

- Using the **method A** (Table (25)), we can conclude that the temporal window $[2^h - 3^h]$ seems to give the best results following the criterion of the greatest correlation coefficient ($r_c = 0.29$). One can observe also that, for this time interval, the probability P that two uncorrelated distributions give a correlation coefficient greater than that found with the actual measurements, is the smallest ($P = 0.49$) so we conclude that this is the best interval on which we can analyze the simulations. In Fig.(67) we report a graphic global analysis of these data.
- Using **method B** (Table (26)-(27)), we can observe that when computed without the first hundred meters a better correlation ($r_c = 0.33$) is achieved than with the first 100 m ($r_c = 0.20$). The criterium of the minimum standard deviation, leads to the opposite conclusion, i.e. the scattering computed with the first 100 m ($\sigma = 0.50$) is better than that obtained without the surface layer ($\sigma = 0.54$). So, we have no, at the moment, sufficient elements to be confident or not in the surface layer prediction of Meso-Nh. In Fig.(68)-(73) we report a graphic global analysis of these data.

We want to underline that only the method B, having access to the C_N^2 profiles, gives a correct estimation of the calibration coefficient. As an example we report for the night 19/5/93 in Fig.(77), Fig.(78) and Fig.(79) the C_N^2 profiles

provided by Scidar and by Meso-Nh using three different calibration coefficient β as obtained using the method A and the method B with and without the first 100 m. If we observe the higher part of the C_N^2 profiles, that is the part less modified by the orographic effect but sensitive to the climatological noise, we can deduce that the $\beta = 4.48$ gives the best fit with the Scidar.

- We discussed, until now, the results from a global point of view. Can we have a finer analysis about the estimation of the energy in the low and in the high part of the atmosphere? Looking at the Fig.(69), (70), (72) and (73) it is obvious that the correlation level, especially in the high part of the atmosphere is weak. This fact is clearly attributed to a bad reliability level of the Antofagasta radiosounding that penalizes the **statistical** analysis.

In spite of this, we underline the following interesting result. In the analyzed cases (with and without the first 100 m of atmosphere) the slope of the regression line (after calibration) related to ε_{BL} and ε_{FA} are of the same order of magnitude. This means that the model sensitivity is good not only in the lower part of the atmosphere, as we might expect, but in the higher part too. A good C_N^2 profile reconstruction at these high altitude could be very interesting for the scintillation rate, the isoplanetic angle and the wavefront coherence time previsions; all of these parameters are very sensitive to this kind of turbulence. In particular, the previsions performances of the wavefront coherence time could be extremely positive. We know, that its sensitivity grows up with a $5/3$ power of wind intensity. At these latitudes the jet stream wind can reach 60 m/sec and it becomes a real discriminant parameter. Knowing that the wind previsions at the synoptic scales are generally well reliable, this numeric technic could give good forecasts.

To give an example of good model sensitivity at the high altitudes, we report in Fig.(74) a comparison between the C_N^2 profile obtained by the model and the balloons launched over the Paranal during the PARSCA92 campaign. Any systematic study has been realised on this campaign and we report this result to give an idea of the model sensitivity at the high altitude.

- Another important conclusion that we can provide by this study is a confirmation of the good geographic location of the Paranal site. In all the horizontal seeing maps [Fig.(35-42)] it is clear that the Paranal is characterized by the best seeing conditions and that it is sufficiently far from the Chilean coast which is characterized, on the contrary, by a high turbulence production rate. To give an example of the different turbulence production budget over the coast and the Paranal mount, we report in Fig.(75), the time seeing evolution (over 4^h S.T.).

5.1 Statistical reliability

In order to estimate the statistic reliability of our technic, we compared the statistical estimators presented in the previously paragraph with those obtained by a simple forecast by persistence method. In Fig.(76) is reported the graphic comparison between the forecast by persistence method and the numeric one. Following the

criterion of the maximum correlation coefficient, the numerical method gives better results: $(r_c)_{MNH} > (r_c)_{persistence}$. On the contrary, following the criterion of the minimum standard deviation, the forecast by persistence method gives better results: $\sigma_{persistence} < \sigma_{MNH}$. This apparent contradiction is attributed to the small number of statistical points. In spite of this, it is important to remember that the conditions are particularly favorable for the forecast by persistence. We limited our analysis to only 15 nights during which we can identify two period Table(22) and Table(23) characterized by a bad ($\bar{\varepsilon} = 0.97$) and a better ($\bar{\varepsilon} = 0.57$) seeing. The statistical fluctuations around these mean values are not great. Under these conditions the forecast by persistence method is particularly efficient. The seeing computed over long period would be presumably characterized by greater fluctuations. We can expect that, under a more realistic condition, the forecast by persistence method might give worse results.

5.2 Adaptation time

At the end of the first part of this feasibility study we concluded that the model stability seemed dependent from the grid point (p.18). After 1^h30 min S.T. we never observed an obvious convergence toward a stationary regime of the model. At the end of the complete analysis we can make the following remarks:

- looking at the Fig.(43)-Fig.(50) we can affirm that the adaptation time to the orography is never smaller than 30 min. This means that we shall not be able to have a reliable prevision within a time simulation shorter than 30 min.
- in most of the cases the model fluctuates around a stationary mean value. The model never diverges.
- the time window [2^h-3^h] seems to give the best results following two different criteria: the correlation between the Scidar measurements and the Meso-Nh simulations is maximum and the standard deviation to the regression straight line is minimum.

5.3 Radiative transfer contribution

As announced at the end of the first phase of this study we started a simulation taking into account the radiative transfer. In this way the model computes the thermic vertical fluxes emitted by the ground during the night. For what concern the total energy budget, this element is extremely important for a correct evaluation of the nighttime atmospheric turbulence near the ground. In Fig.(80) is reported, as an example, the seeing evolution over 4^h S.T. during the 16/5 night. It is clear that the radiative contribution is important in the global energy budget. We thus recommend, in the future, to take into account systematic study using this configuration.

5.4 Optimization of the ECMWF product utilization

One of the most important problems that we found using the ECMWF analysis is that they do not show the thermic inversion of the lower layer. One of the possible

reason of this lack of information is due to the fact that the analysis grid point is located a little bit inland (grid point ESO1=(70.32 W, 23.62 S)) Fig.(81) and not above the ocean. We know that the ECMWF analyses are computed using the optimal interpolation algorithm (Annex 2), from the observed meteorological parameters. If the analyzed grid point is located above a mountain, the meteorological parameters, related to the altitudes comprised between the sea and the local level are extrapolated by the hydrostatic law:

$$dp = -\rho g dz \quad (32)$$

Temperature is retrieved by the pressure by the:

$$\frac{T_1}{T_0} = \left(\frac{P_1}{P_0}\right)^{\frac{R_a}{C_{pa}}} \quad (33)$$

where

$R_a = 287 J K g^{-1} K^{-1}$, $C_{pa} = 1005 J K g^{-1} K^{-1}$ and $\frac{R_a}{C_{pa}} = 2/7$.

It is clear that the presence of the ground, and in particular of an high mountain, prevents from a good temperature profile reconstruction in the first kilometer over the sea. In order to verify if a better choice of the analysis grid point could give better results for the thermic inversion at ground, we took the same kind of ECMWF analysis on 15 level over two other grid points far away above the sea. In Fig.(82) and Fig.(83) we reported the potential and absolute temperature profile versus the altitude related to the three grid points ESO1, ESO2 and ESO3. They are compared to the radiosounding temperature profile measured at Antofagasta.

It is evident that, an analysis on a grid point above the sea far from the coast, gives a better reconstruction of the thermal inversion than the radiosoundings.

Moreover, we know that the ECMWF data base can deliver analyses computed on 31 levels (ECMWF - MARS catalogue - Meteorological Bulletin M32 - 22 December 95) which are however not systematically supplied to all clients. We think that, in the perspective of an optimization of the simulation procedure, a better choice of the initialization products provided by the ECMWF should be done in the future.

5.5 Simulation price

As we told in the introduction, one of the most important application of this feasibility study is the flexible scheduling. The scientific challenge is to forecast a correct optical turbulence distribution in the atmosphere using an ‘optimal’ configuration. Among the parameters that help to define the word ‘optimal’, one can not forget the price of a simulation. As the ESO Director General told in his introductory talk at the ESO Workshop ‘*Forecasting Astronomical Observing Conditions*’, the cost of a one night of operation of the observatory (about 100000 DM) gives the scale for deciding the extent to which the astronomic community should push research in modeling and prediction. In Table(84) we reported a summary of the price related to different configurations tested during this study. The price reported in the last column is related to the listing price of the **Cray9000** (Meteo France) on September 1997. At this date, the price of a one CPU hour decreased from **771 DM** to **200**

DM. On spring 1998 the Cray9000 will be replaced by a **Fujitsu VPP700**. The price of one CPU hour will be **114 DM** and the model will be two times faster. We can easily estimate, thus, a reduction of the initial price by a **13.5** factor. Besides this, is it possible that, in the future, royalties for a commercial use of the model will be imposed.

6 Conclusions and Perspectives

We intend to summarize, here, the principal conclusion provided by this feasibility study for a seeing forecast and to give a sketch of the possible developments in this research.

- We demonstrated that a simplified simulation principle gives realistic results. A non-hydrostatic model, well adapted to put in evidence the orographic effects on the development of the gravity waves, reproduces, as we might expect, a seeing characterized by an extended region of a great turbulence production over the Chilean coast and by a general low turbulence levels over the Paranal mountain site. This numerical technique could be thus efficiently used for the site testing studies.
- We demonstrated that the model has a good sensitivity. It can discriminate, in a correct quantitative way, the worst and the best seeing of the campaign ranging within less than 1 arcsec.
- The turbulence rate simulated by the model is well estimated both in the low and high part of the atmosphere. We remember briefly the turbulent layer developed in the 16/5/93 night after 4 hours simulation time Fig.(53) and the layer resolved by the model at 10 km in the 25/3/92 night Fig.(74).
- The sensitivity to the orographic effect is proved. Turbulence at the ground level is *produced* by the model. We remember the 16/5/93 night case. In the actual configuration the model needs 4 h about to adapt itself to the terrain.
- The proved poor quality of the Antofagasta radiosoundings is the principal cause of erroneous simulations obtained during few nights. In these cases, unrealistic dynamic instabilities are produced by the model in the middle high of the atmosphere. The Antofagasta radiosoundings have sufficient vertical resolution but are not completely reliable, at least in the limited temporal period analyzed (only 8 nights). From a statistical point of view, we can not affirm that this technique gives better results than the forecast by persistence one but it is important to make the following remarks:
 - The sample analyzed is statistically poor
 - A comparison with the forecast by persistence method might be significant only on a longer period

- The Antofagasta radiosoundings are not the only products supplied by the Meteorologic Centers and others kinds of data could be analyzed. In the previous chapter we suggested to use data provided by others catalogue and extracted by grid points far away above the sea.
- We showed that, in order to calibrate the model it is necessary to retrieve C_N^2 profiles and then the seeing. Using only integrated value, without the knowledge of the vertical turbulence distribution one could attend to a wrong estimation of the adaptation time for example. Moreover, one could overestimate the turbulence in the high part of the atmosphere.

Finally we add that our feasibility study is well complementary to the '*Feasibility study of a meteorological prediction model for ESO observatories in Chile*' - [45060/VLT/95/6952/GW] one.

We read in the conclusions of this rapport that it is proved that the ECMWF products give a good ground temperature prevision. We proved that, to use a numerical technic, it is not sufficient to well forecast the ground temperature. It is mandatory that the observed meteorological data over the whole atmosphere to be of good quality.

For what concern the perspectives of such a study we underline the following:

- We intend to test, in the next future, the Meso-Nh model above the Spanish site of the Canaries Islands at La Palma comparing simulations with the Scidar measurements obtained during the campaign CAN95 that took place in November 95 at the Roque de Los Muchachos Observatory. In this occasion, the classic Scidar version, was modified in order to have access to the boundary layer turbulence. We will have a more reliable measurements to compare to the simulations. Moreover, we shall be able to initialize the model with Tenerife Meteo Station radiosoundings whose reliability is better than Antofagasta ones. We shall dispose, finally, of a complete site measurements: balloons U,P,T and C_N^2 profiles measured at the site, meteorologic ground measurements provided by the local masts and seeing measurements provided by the IAC (Instituto de Astrofisica de Canarias) made with a DIMM.
- We suggest, as explain in the previous chapter, a systematic study using the radiative emission scheme.
- In order to obtain a more rapid model orographic adaptation, it could be interesting to study the possibility to initialize the model with a not constant mixing length.
- In order to better test the forecasting performance efficiency of the technic we should use the forecast products of a meteorologic center such as the ECMWF. Only introducing new initial values in the model during a night every 6 hours we could obtain a **real seeing forecast**.
- From the point of view of the model optimization it could be interesting to study:

- the actual role of the ϕ_3 function in the dynamic turbulence model parameterization for these kind of simulations.
 - the model sensitivity to different vertical sampling of the variable
- We should apply the Meso-Nh model to a wider set of observations to improve the statistical meaning and to test the reliability of the technique.

7 ACKNOWLEDGMENTS

The authors wish to thank the GMME team of the Centre National de Recherche Meteorologique for their scientific collaboration and logistical help. In particular, they are grateful to J. Stein, P. Jabouille, J.L. Redelsperger and J.P. Lafore for the assistance with the various technical mysteries of their computer system. We extend our thanks to M. Nuret for the time he devoted to our project and to E. Pesin for her technical support with network connections. The authors are grateful to M.Sarazin for his constant and dedicated presence. We thank G. Lund for his helpful comments and revision of the authors original English draft.

ANNEX1: Simulation procedures

Pre-processing phase

Before making a simulation, the user must complete a particular namelist with the radiosoundings or the analysis data required to initialize the model and must provide the geophysical and geometric parameters: surface dimensions, longitude and latitude of the center of the defined surface, temperature distribution at ground level, temporal evolution of ground temperature, horizontal and vertical resolutions for the model, terrain roughness, sea temperature, boundary conditions as reported in Fig.(6). A standard procedure is then used to prepare a binary file containing all this information which are then stored into the Cray computer to be used in the real simulation process.

Simulation phase

To perform a simulation the model uses the file prepared in the pre-processing phase together with further data which the user provides by means of a second namelist. This list defines, among other items, the following principal terms:

- the temporal duration of the complete simulation in the time domain of the propagation model
- the time sampling interval within the time domain of the propagation model (time step length). The value of this parameter is very important because Meso-Nh is an explicit model, (that is the variables are computed starting from the last sampled time); a wrong time sampling can generate numerical spurious waves. The time step length is related to the model mesh size and to the maximum speed of the flow. It is defined by a stability analysis that leads to a criterion of the limit time step which can be expressed as follows:

$$\Delta t_{\min} = \left(\frac{U_0}{\Delta x} + \frac{N_0 |\cos(\pi \Delta z / 2H)|}{\left[1 + \left(\frac{\Delta x}{\Delta z} \sin(\pi \Delta z / 2H) \right)^2 \right]^{1/2}} \right)^{-1} \quad (34)$$

where Δt_{\min} is the limit time step leading to a stable integration, H is the height of model top, Δx and Δz are respectively the horizontal and vertical mesh intervals, U_0 is the maximum flow speed and N_0 is the Brunt-Vaisala frequency. Some comments may be made about this stability analysis:

- a) For weak mesh aspect ratio $\Delta x / \Delta z$, Δt_{\min} is quasi-independent of the domain height H (meso- γ scale, that is small length scales)
- b) For large mesh aspect ratio $\Delta x / \Delta z$, Δt_{\min} depends on H (meso- α and meso- β scales, that is large length scales).

In practice, for all the configurations, a simpler law can be used. It has been tested in many examples giving good results:

$$\Delta t_{\min} = \frac{\Delta x}{U_0} \quad (35)$$

Finally, we remember that Δt_{\min} defines the number of computing unit needed for a given simulation (**Ex:** a 30 min simulation with a time step of $\Delta t_{\min} = 10$ sec needs 180 computing units).

- the activation of different physical parameterization coded in the model such as: the type of **physical turbulence model** used to parameterize the transfer of energy from unresolved to resolved scales, and the **surface model** used to parameterize the transfer of thermal energy from the ground to the atmosphere.

In Fig(7) is reported an example of this namelist. The simulation procedure produces a binary file containing the model outputs for the two different fields:

- prognostic fields (kinetic energy, temperature, wind intensity,...)
- diagnostic fields (mixing length, pressure,...).

Post-processing phase

A post-processing facility enables simple visual access to the 3-D and 2-D fields computed by the Meso-Nh model. This program uses a file that contains three namelist. They control respectively

- the reading of model variables in the binary file produced during the simulation phase
- the portion of the model domain which is displayed, the geometry of the plot (horizontal map, vertical cross-section, vertical profile,...)
- various visual characteristics of the plot.

In Fig.(8) is reported an example of this last namelist. A procedure is used to read these commands and to create a meta-file that can be viewed using a standard graphic NCAR package. Any selected graphical output can be obtained in postscript format (**filename.ps**).

In order to make statistical analyses of the model sensitivity, **the code has been modified to produce not only graphics, but also numerical data outputs.** We intend to make a comparison between the model and observed data, which is not only qualitative but also quantitative. This can now be achieved by taking data simulated by the Meso-Nh and comparing it with measurements obtained from the SCIDAR and the DIMM.

ANNEX2: Data assimilation and data quality

The aim of the analysis [34] is to provide the general circulation numeric model with the most realistic state of the atmosphere. For so doing the ECMWF uses a finite number of observations and a **first guess** provided by the same prevision model (generally the last six hours prevision) or by the climatology. The analysis must modify this first guess integrating in the best way the informations coming from the observations which, in general, do not describe perfectly the atmosphere state. Different quality controls are realized on the observations data in order to select a realistic set of data. The assimilation of the first guess and the observations are made using an algorithm named **optimal interpolation**. If A is the analyzed parameter, for each grid point is defined:

$$a_k^a = a_k^g + \sum_i \lambda_i (y_i^o - y_i^g) \quad (36)$$

where

- a_k^a is the value of A that we want to know in the k grid point
- a_k^g is the value of the parameter provided by the first guess in the k grid point
- λ_i is the averaged weight associated to the quality of the observation (kind of measurement and kind of observed parameter), the distance between the analysis grid point and the observations grid point and the quality of the first guess
- y_i^o is the observed value of the parameter Y (Y can be A or, more generally, a parameter linearly correlated to A)
- y_i^g is the value of Y provided by the first guess.

The optimal interpolation method defines λ_i in the following way:

$$\lambda_i = \frac{\sigma_g^2}{\sigma_{o,i}^2 + \sigma_g^2} \quad (37)$$

which transforms the equation 36 into

$$a_k^a = a_k^g + \sum_i \frac{\sigma_g^2}{\sigma_{o,i}^2 + \sigma_g^2} (y_i^o - y_i^g) \quad (38)$$

where $\sigma_{o,i}^2$ is the variance of observations errors, σ_g^2 is the variance of the first guess error resulting from the total uncertainty in the analysis. When an observation is unreliable, $\sigma_{o,i}^2$ is large and a_k^a takes the value of a_k^g . In this case there is a little impact on the first guess. When the observation is assumed to be accurate, $\sigma_{o,i}^2$ is small and a_k^a , almost takes the value y_i^o .

These analysis, named **uninitialized analysis**, can generate, sometimes, fictive gravity waves during the simulations. To avoid this, they must be initialized in order

to be adapted to the dynamic of the model. This more elaborated analysis is named **initialized analysis**.

In an operational schedule, the ECMWF produces global analysis and previsions using data collected during the time. The previsions are permanently corrected by the observations that are injected in the algorithm of the optimal interpolation. This feed-back system of assimilation data is named **Analysis Assimilation**.

ANNEX 3: Summary of night by night optical turbulence for the PARSCA93 campaign

14/5/93	SCIDAR						MESO-NH						Niv=[3-40]
Time window	$C_N^2 BL$	$C_N^2 FA$	ϵ_{BL}	ϵ_{FA}	$\frac{\epsilon_{FA}}{\epsilon_{BL}}$	ϵ_{TOT}	$C_N^2 BL$	$C_N^2 FA$	ϵ_{BL}	ϵ_{FA}	$\frac{\epsilon_{FA}}{\epsilon_{BL}}$	ϵ_{TOT}	Sim.Time
[00:00-01:00]	-	-	-	-	-	-	$2.01 \cdot 10^{-14}$	$2.53 \cdot 10^{-14}$	0.12	0.13	1.14	0.20	30min
[01:00-02:00]	$5.13 \cdot 10^{-13}$	$4.50 \cdot 10^{-13}$	0.84	0.78	0.92	1.23	$1.50 \cdot 10^{-13}$	$2.59 \cdot 10^{-14}$	0.40	0.14	0.35	0.44	1 ^h
[02:00-03:00]	$4.89 \cdot 10^{-13}$	$3.90 \cdot 10^{-13}$	0.82	0.71	0.87	1.16	$5.91 \cdot 10^{-13}$	$2.58 \cdot 10^{-14}$	0.92	0.14	0.15	0.94	2 ^h
[03:00-04:00]	$1.94 \cdot 10^{-13}$	$2.57 \cdot 10^{-13}$	0.55	1.18	0.78	0.47	$4.24 \cdot 10^{-13}$	$2.57 \cdot 10^{-14}$	0.75	0.14	0.18	0.78	3 ^h
[04:00-05:00]	$2.45 \cdot 10^{-13}$	$2.57 \cdot 10^{-12}$	0.54	0.55	1.02	0.83	$5.91 \cdot 10^{-13}$	$2.58 \cdot 10^{-14}$	0.92	0.14	0.15	0.94	4 ^h
[05:00-06:00]	$3.54 \cdot 10^{-12}$	$1.83 \cdot 10^{-13}$	0.67	0.45	0.67	0.86							
							$4.39 \cdot 10^{-13}$	$2.58 \cdot 10^{-14}$	0.75	0.14		0.77	Mean
[00:00-06:00]	$3.76 \cdot 10^{-13}$	$3.19 \cdot 10^{-14}$	0.70	0.63	0.90	1.01							

Table 5: Analysis of the 14/5 night. In the left part of the table we report the Scidar measurements analysis and in the right part the Meso-Nh simulations ones. In the first column are reported the time windows in which the variables are averaged. In the first six lines is report a detailed analysis for each hour, and the last line report the average estimation taken over the whole night. In the second column we compute the $C_N^2 \Delta h$ inside the Boundary Layer ($\Delta h = |2600 - 5000| m$) and in the third column inside the Free Atmosphere ($\Delta h = |5000 - 20000| m$). We labeled with BL=Boundary Layer the first 5 km of the atmosphere because we estimate that the orographic effects, during 4^h simulation time intervals, have an important influence in this part of the atmosphere. In this way we select, with the BL, the atmosphere region where the Meso-Nh model performances are expected. In the fourth column is reported the seeing related to the BL (ϵ_{BL}), in the fifth column the seeing related to the FA (ϵ_{FA}), in the sixth column the ratio of them ($\epsilon_{FA}/\epsilon_{BL}$) and in the seventh column the total seeing (ϵ_{TOT}) integrated over the whole atmosphere ($\Delta h = |2600 - 20000| m$). In the right part of the table, the same variable are reported for different simulation time intervals of the Meso-Nh simulations. In the last column are reported the different simulation time intervals sampled with one hour increment. In the last line, the same variables are averaged over 4^h simulation time interval. In the first line of the last column we report the model levels used in the computations.

15/5/93	SCIDAR						MESO-NH						Niv=[3-40]
Time window	$C_N^2 BL$	$C_N^2 FA$	ϵ_{BL}	ϵ_{FA}	$\frac{\epsilon_{FA}}{\epsilon_{BL}}$	ϵ_{TOT}	$C_N^2 BL$	$C_N^2 FA$	ϵ_{BL}	ϵ_{FA}	$\frac{\epsilon_{FA}}{\epsilon_{BL}}$	ϵ_{TOT}	Sim.Time
[00:00-01:00]	-	-	-	-	-	-	$1.02 \cdot 10^{-14}$	$1.50 \cdot 10^{-13}$	0.08	0.40	4.99	0.42	30min
[01:00-02:00]	$4.22 \cdot 10^{-13}$	$1.15 \cdot 10^{-13}$	0.75	0.34	0.45	0.86	$2.09 \cdot 10^{-14}$	$2.12 \cdot 10^{-13}$	0.12	0.50	4.01	0.53	1 ^h
[02:00-03:00]	$3.48 \cdot 10^{-13}$	$1.02 \cdot 10^{-13}$	0.66	0.32	0.47	0.78	$2.96 \cdot 10^{-14}$	$2.45 \cdot 10^{-13}$	0.15	0.54	3.55	0.58	2 ^h
[03:00-04:00]	$3.97 \cdot 10^{-13}$	$1.68 \cdot 10^{-13}$	0.72	0.43	0.59	0.89	$2.88 \cdot 10^{-14}$	$1.67 \cdot 10^{-13}$	0.15	0.43	2.87	0.47	3 ^h
[04:00-05:00]	$2.74 \cdot 10^{-13}$	$1.68 \cdot 10^{-13}$	0.58	0.43	0.74	0.77	$8.59 \cdot 10^{-14}$	$2.72 \cdot 10^{-13}$	0.28	0.57	1.99	0.68	4 ^h
[05:00-06:00]	$3.05 \cdot 10^{-14}$	$1.20 \cdot 10^{-14}$	0.61	0.35	0.57	0.75							
							$4.13 \cdot 10^{-13}$	$2.24 \cdot 10^{-13}$	0.17	0.51		0.56	Mean
[00:00-06:00]	$3.54 \cdot 10^{-13}$	$1.37 \cdot 10^{-14}$	0.67	0.38	0.56	0.82							

Table 6: Analysis of the 15/5 night. Same as Table (5)

16/5/93	SCIDAR							MESO-NH							Niv=[3-40]
Time window	C_N^{BL}	C_N^{FA}	ε_{BL}	ε_{FA}	$\frac{\varepsilon_{EA}}{\varepsilon_{BL}}$	ε_{TOT}		C_N^{BL}	C_N^{FA}	ε_{BL}	ε_{FA}	$\frac{\varepsilon_{EA}}{\varepsilon_{BL}}$	ε_{TOT}		Sim.Time
[00:00-01:00]	-	-	-	-	-	-		$2.19 \cdot 10^{-14}$	$4.02 \cdot 10^{-15}$	0.13	0.04	0.36	0.14		30min
[01:00-02:00]	$1.12 \cdot 10^{-12}$	$6.91 \cdot 10^{-14}$	1.34	0.25	0.18	1.39		$4.59 \cdot 10^{-14}$	$4.08 \cdot 10^{-15}$	0.20	0.05	0.23	0.21		1 ^h
[02:00-03:00]	$1.26 \cdot 10^{-12}$	$4.97 \cdot 10^{-14}$	1.44	0.20	0.14	1.48		$6.27 \cdot 10^{-14}$	$4.28 \cdot 10^{-15}$	0.24	0.05	0.20	0.25		2 ^h
[03:00-04:00]	$1.18 \cdot 10^{-12}$	$4.16 \cdot 10^{-14}$	1.39	0.18	0.13	1.42		$7.29 \cdot 10^{-14}$	$1.25 \cdot 10^{-13}$	0.26	0.36	1.38	0.47		3 ^h
[04:00-05:00]	$1.05 \cdot 10^{-12}$	$2.53 \cdot 10^{-14}$	1.29	0.13	0.10	1.31		$4.01 \cdot 10^{-13}$	$4.27 \cdot 10^{-15}$	0.73	0.04	0.06	0.73		4 ^h
[05:00-06:00]	$8.36 \cdot 10^{-13}$	$2.13 \cdot 10^{-14}$	1.13	0.12	0.11	1.14									
								$14.53 \cdot 10^{-14}$	$3.47 \cdot 10^{-15}$	0.36	0.12		0.41		Mean
[00:00-06:00]	$1.12 \cdot 10^{-12}$	$4.43 \cdot 10^{-14}$	1.35	0.19	0.14	1.38									

Table 7: Analysis of the 16/5 night. Same as Table (5)

17/5/93	SCIDAR							MESO-NH							Niv=[3-40]
Time window	C_N^{BL}	C_N^{FA}	ε_{BL}	ε_{FA}	$\frac{\varepsilon_{EA}}{\varepsilon_{BL}}$	ε_{TOT}		C_N^{BL}	C_N^{FA}	ε_{BL}	ε_{FA}	$\frac{\varepsilon_{EA}}{\varepsilon_{BL}}$	ε_{TOT}		Sim.Time
[00:00-01:00]	-	-	-	-	-	-		$0.81 \cdot 10^{-14}$	$2.22 \cdot 10^{-14}$	0.07	0.12	1.82	0.15		30min
[01:00-02:00]	$4.49 \cdot 10^{-13}$	$9.55 \cdot 10^{-14}$	0.77	0.30	0.39	0.87		$0.82 \cdot 10^{-14}$	$3.45 \cdot 10^{-14}$	0.07	0.16	2.36	0.19		1 ^h
[02:00-03:00]	$4.31 \cdot 10^{-13}$	$8.28 \cdot 10^{-14}$	0.76	0.28	0.37	0.84		$0.82 \cdot 10^{-14}$	$0.39 \cdot 10^{-13}$	0.07	0.17	2.55	0.20		2 ^h
[03:00-04:00]	$4.81 \cdot 10^{-13}$	$4.16 \cdot 10^{-14}$	0.81	0.24	0.30	0.87		$0.80 \cdot 10^{-14}$	$0.39 \cdot 10^{-13}$	0.07	0.18	2.60	0.20		3 ^h
[04:00-05:00]	$5.20 \cdot 10^{-13}$	$8.08 \cdot 10^{-14}$	0.85	0.27	0.32	0.92		$0.82 \cdot 10^{-14}$	$0.39 \cdot 10^{-13}$	0.07	0.18	2.54	0.20		4 ^h
[05:00-06:00]	$3.89 \cdot 10^{-13}$	$7.51 \cdot 10^{-14}$	0.71	0.26	0.37	0.79									
								$0.81 \cdot 10^{-14}$	$3.78 \cdot 10^{-14}$	0.07	0.18		0.20		Mean
[00:00-06:00]	$4.63 \cdot 10^{-13}$	$8.02 \cdot 10^{-14}$	0.79	0.27	0.34	0.87									

Table 8: Analysis of the 17/5 night. Same as Table (5)

18/5/93	SCIDAR							MESO-NH							Niv=[3-40]
Time window	C_N^{BL}	C_N^{FA}	ε_{BL}	ε_{FA}	$\frac{\varepsilon_{EA}}{\varepsilon_{BL}}$	ε_{TOT}		C_N^{BL}	C_N^{FA}	ε_{BL}	ε_{FA}	$\frac{\varepsilon_{EA}}{\varepsilon_{BL}}$	ε_{TOT}		Sim.Time
[00:00-01:00]	$7.09 \cdot 10^{-13}$	$2.01 \cdot 10^{-13}$	1.02	0.48	0.46	1.19		$1.21 \cdot 10^{-14}$	$2.11 \cdot 10^{-14}$	0.09	0.12	1.39	0.16		30min
[01:00-02:00]	$3.65 \cdot 10^{-13}$	$2.49 \cdot 10^{-13}$	0.68	0.54	0.79	0.94		$1.21 \cdot 10^{-14}$	$2.09 \cdot 10^{-14}$	0.09	0.12	1.38	0.16		1 ^h
[02:00-03:00]	$4.30 \cdot 10^{-13}$	$2.25 \cdot 10^{-13}$	0.75	0.51	0.67	0.97		$1.16 \cdot 10^{-14}$	$2.13 \cdot 10^{-14}$	0.09	0.12	1.43	0.16		2 ^h
[03:00-04:00]	$3.72 \cdot 10^{-13}$	$1.98 \cdot 10^{-13}$	0.69	0.47	0.68	0.90		$1.16 \cdot 10^{-14}$	$2.54 \cdot 10^{-14}$	0.75	0.09	0.14	0.17		3 ^h
[04:00-05:00]	$3.83 \cdot 10^{-13}$	$1.29 \cdot 10^{-12}$	0.70	0.37	0.52	0.84		$1.11 \cdot 10^{-14}$	$2.11 \cdot 10^{-14}$	0.09	0.12	1.47	0.16		4 ^h
[05:00-06:00]	$6.57 \cdot 10^{-13}$	$1.27 \cdot 10^{-13}$	0.97	0.36	0.37	1.08									
								$1.16 \cdot 10^{-14}$	$2.21 \cdot 10^{-14}$	0.09	0.12		0.16		Mean
[00:00-06:00]	$4.19 \cdot 10^{-13}$	$1.92 \cdot 10^{-13}$	0.74	0.46	0.62	0.93									

Table 9: Analysis of the 18/5 night. Same as Table (5)

19/5/93	SCIDAR							MESO-NH							Niv=[3-40]
Time window	C_N^{BL}	C_N^{FA}	ε_{BL}	ε_{FA}	$\frac{\varepsilon_{EA}}{\varepsilon_{BL}}$	ε_{TOT}		C_N^{BL}	C_N^{FA}	ε_{BL}	ε_{FA}	$\frac{\varepsilon_{EA}}{\varepsilon_{BL}}$	ε_{TOT}		Sim.Time
[00:00-01:00]	$2.16 \cdot 10^{-13}$	$5.27 \cdot 10^{-13}$	0.50	0.85	1.70	1.05		$1.49 \cdot 10^{-14}$	$1.18 \cdot 10^{-14}$	0.10	0.09	0.86	0.14		30min
[01:00-02:00]	$4.76 \cdot 10^{-13}$	$1.99 \cdot 10^{-13}$	0.80	0.47	0.59	0.99		$1.45 \cdot 10^{-14}$	$1.20 \cdot 10^{-14}$	0.10	0.09	0.89	0.14		1 ^h
[02:00-03:00]	$2.98 \cdot 10^{-13}$	$1.98 \cdot 10^{-13}$	0.61	0.47	0.78	0.82		$1.40 \cdot 10^{-14}$	$1.20 \cdot 10^{-14}$	0.10	0.09	0.91	0.14		2 ^h
[03:00-04:00]	$3.09 \cdot 10^{-13}$	$1.35 \cdot 10^{-13}$	0.62	0.38	0.61	0.77		$1.41 \cdot 10^{-14}$	$1.22 \cdot 10^{-14}$	0.10	0.09	0.91	0.14		3 ^h
[04:00-05:00]	$2.80 \cdot 10^{-13}$	$1.46 \cdot 10^{-13}$	0.58	0.39	0.67	0.75		$1.40 \cdot 10^{-14}$	$1.21 \cdot 10^{-14}$	0.10	0.09	0.91	0.14		4 ^h
[05:00-06:00]	$3.22 \cdot 10^{-13}$	$1.60 \cdot 10^{-13}$	0.63	0.42	0.65	0.81									
								$1.41 \cdot 10^{-14}$	$1.21 \cdot 10^{-14}$	0.10	0.09		0.14		Mean
[00:00-06:00]	$3.35 \cdot 10^{-13}$	$1.87 \cdot 10^{-13}$	0.65	0.46	0.70	0.85									

Table 10: Analysis of the 19/5 night. Same as Table (5)

23/5/93	SCIDAR						MESO-NH						Niv=[3-40]
Time window	C_N^{BL}	C_N^{FA}	ε_{BL}	ε_{FA}	$\frac{\varepsilon_{EA}}{\varepsilon_{BL}}$	ε_{TOT}	C_N^{BL}	C_N^{FA}	ε_{BL}	ε_{FA}	$\frac{\varepsilon_{EA}}{\varepsilon_{BL}}$	ε_{TOT}	Sim.Time
[00:00-01:00]	$3.13 \cdot 10^{-13}$	$1.32 \cdot 10^{-13}$	0.62	0.37	0.59	0.77	$9.50 \cdot 10^{-15}$	$1.81 \cdot 10^{-13}$	0.08	0.45	5.87	0.46	30min
[01:00-02:00]	$2.22 \cdot 10^{-13}$	$1.31 \cdot 10^{-13}$	0.51	0.37	0.72	0.67	$9.91 \cdot 10^{-15}$	$1.35 \cdot 10^{-13}$	0.08	0.38	4.79	0.39	1 ^h
[02:00-03:00]	$1.72 \cdot 10^{-13}$	$1.13 \cdot 10^{-13}$	0.43	0.34	0.77	0.59	$1.18 \cdot 10^{-14}$	$8.70 \cdot 10^{-14}$	0.09	0.29	3.31	0.31	2 ^h
[03:00-04:00]	$1.42 \cdot 10^{-13}$	$1.44 \cdot 10^{-13}$	0.39	0.39	1.00	0.59	$9.86 \cdot 10^{-15}$	$1.69 \cdot 10^{-13}$	0.08	0.43	5.49	0.44	3 ^h
[04:00-05:00]	$2.90 \cdot 10^{-13}$	$1.14 \cdot 10^{-13}$	0.60	0.34	0.57	0.73	$9.69 \cdot 10^{-15}$	$1.52 \cdot 10^{-13}$	0.08	0.40	5.22	0.42	4 ^h
[05:00-06:00]	$3.76 \cdot 10^{-13}$	$7.93 \cdot 10^{-14}$	0.70	0.27	0.39	0.78							
							$1.0 \cdot 10^{-14}$	$1.35 \cdot 10^{-13}$	0.08	0.37		0.39	Mean
[00:00-06:00]	$2.29 \cdot 10^{-13}$	$1.25 \cdot 10^{-13}$	0.52	0.36	0.69	0.67							

Table 11: Analysis of the 23/5 night. Same as Table (5)

25/5/93	SCIDAR						MESO-NH						Niv=[3-40]
Time window	C_N^{BL}	C_N^{FA}	ε_{BL}	ε_{FA}	$\frac{\varepsilon_{EA}}{\varepsilon_{BL}}$	ε_{TOT}	C_N^{BL}	C_N^{FA}	ε_{BL}	ε_{FA}	$\frac{\varepsilon_{EA}}{\varepsilon_{BL}}$	ε_{TOT}	Sim.Time
[00:00-01:00]	$6.35 \cdot 10^{-14}$	$9.19 \cdot 10^{-14}$	0.24	0.30	1.24	0.41	$7.98 \cdot 10^{-15}$	$2.16 \cdot 10^{-14}$	0.07	0.12	1.81	0.15	30min
[01:00-02:00]	$5.34 \cdot 10^{-14}$	$8.27 \cdot 10^{-14}$	0.21	0.28	1.29	0.38	$8.60 \cdot 10^{-15}$	$2.17 \cdot 10^{-14}$	0.07	0.12	1.74	0.15	1 ^h
[02:00-03:00]	$6.46 \cdot 10^{-14}$	$9.78 \cdot 10^{-14}$	0.24	0.31	1.28	0.42	$1.08 \cdot 10^{-14}$	$2.17 \cdot 10^{-14}$	0.08	0.12	1.52	0.16	2 ^h
[03:00-04:00]	$5.72 \cdot 10^{-14}$	$6.54 \cdot 10^{-14}$	0.22	0.24	1.08	0.35	$3.72 \cdot 10^{-14}$	$2.17 \cdot 10^{-14}$	0.17	0.12	0.72	0.23	3 ^h
[04:00-05:00]	$5.10 \cdot 10^{-14}$	$4.62 \cdot 10^{-14}$	0.21	0.19	0.94	0.31	$2.00 \cdot 10^{-14}$	$2.18 \cdot 10^{-14}$	0.12	0.13	1.05	0.19	4 ^h
[05:00-06:00]	-	-	-	-	-	-							
							$1.91 \cdot 10^{-14}$	$2.17 \cdot 10^{-14}$	0.11	0.12		0.18	Mean
[00:00-06:00]	$5.93 \cdot 10^{-14}$	$8.28 \cdot 10^{-14}$	0.23	0.28	1.22	0.39							

Table 12: Analysis of the 25/5 night. Same as Table (5)

14/5/93	SCIDAR						MESO-NH						Niv=[1-40]
Time window	C_N^{BL}	C_N^{FA}	ε_{BL}	ε_{FA}	$\frac{\varepsilon_{EA}}{\varepsilon_{BL}}$	ε_{TOT}	C_N^{BL}	C_N^{FA}	ε_{BL}	ε_{FA}	$\frac{\varepsilon_{EA}}{\varepsilon_{BL}}$	ε_{TOT}	Sim.Time
[00:00-01:00]	-	-	-	-	-	-	$2.63 \cdot 10^{-13}$	$2.53 \cdot 10^{-14}$	0.56	0.14	0.24	0.60	30min
[01:00-02:00]	$5.13 \cdot 10^{-13}$	$4.50 \cdot 10^{-13}$	0.84	0.78	0.92	1.23	$3.83 \cdot 10^{-13}$	$2.59 \cdot 10^{-14}$	0.71	0.14	0.20	0.74	1 ^h
[02:00-03:00]	$4.89 \cdot 10^{-13}$	$3.90 \cdot 10^{-13}$	0.82	0.71	0.87	1.16	$7.82 \cdot 10^{-13}$	$2.58 \cdot 10^{-14}$	1.08	0.14	0.13	1.10	2 ^h
[03:00-04:00]	$1.94 \cdot 10^{-13}$	$2.57 \cdot 10^{-13}$	0.55	1.18	0.78	0.47	$5.15 \cdot 10^{-13}$	$2.57 \cdot 10^{-14}$	0.85	0.14	0.16	0.87	3 ^h
[04:00-05:00]	$2.45 \cdot 10^{-13}$	$2.57 \cdot 10^{-12}$	0.54	0.55	1.02	0.83	$7.48 \cdot 10^{-13}$	$2.58 \cdot 10^{-14}$	1.06	0.14	0.13	1.08	4 ^h
[05:00-06:00]	$3.54 \cdot 10^{-12}$	$1.83 \cdot 10^{-13}$	0.67	0.45	0.67	0.86							
							$6.07 \cdot 10^{-13}$	$2.58 \cdot 10^{-14}$	0.92	0.14		0.95	Mean
[00:00-06:00]	$3.76 \cdot 10^{-13}$	$3.19 \cdot 10^{-14}$	0.70	0.63	0.90	1.01							

Table 13: Analysis of the 14/5 night. Same as Table (5)

15/5/93	SCIDAR							MESO-NH							Niv=[1-40]
Time window	C_N^{BL}	C_N^{FA}	ϵ_{BL}	ϵ_{FA}	$\frac{\epsilon_{EA}}{\epsilon_{BL}}$	ϵ_{TOT}		C_N^{BL}	C_N^{FA}	ϵ_{BL}	ϵ_{FA}	$\frac{\epsilon_{EA}}{\epsilon_{BL}}$	ϵ_{TOT}		Sim.Time
[00:00-01:00]	-	-	-	-	-	-		$8.83 \cdot 10^{-14}$	$1.50 \cdot 10^{-13}$	0.29	0.40	1.37	0.53		30min
[01:00-02:00]	$4.22 \cdot 10^{-13}$	$1.15 \cdot 10^{-13}$	0.75	0.34	0.45	0.86		$9.65 \cdot 10^{-14}$	$2.12 \cdot 10^{-13}$	0.31	0.50	1.60	0.62		1 ^h
[02:00-03:00]	$3.48 \cdot 10^{-13}$	$1.02 \cdot 10^{-13}$	0.66	0.32	0.47	0.78		$1.07 \cdot 10^{-13}$	$2.45 \cdot 10^{-13}$	0.33	0.54	1.64	0.67		2 ^h
[03:00-04:00]	$3.97 \cdot 10^{-13}$	$1.68 \cdot 10^{-13}$	0.72	0.43	0.59	0.89		$1.45 \cdot 10^{-13}$	$1.67 \cdot 10^{-13}$	0.39	0.43	1.09	0.63		3 ^h
[04:00-05:00]	$2.74 \cdot 10^{-13}$	$1.68 \cdot 10^{-13}$	0.58	0.43	0.74	0.77		$1.56 \cdot 10^{-13}$	$2.72 \cdot 10^{-13}$	0.41	0.58	1.39	0.76		4 ^h
[05:00-06:00]	$3.05 \cdot 10^{-14}$	$1.20 \cdot 10^{-14}$	0.61	0.35	0.57	0.75									
								$1.26 \cdot 10^{-13}$	$2.24 \cdot 10^{-13}$	0.36	0.51		0.67		Mean
[00:00-06:00]	$3.54 \cdot 10^{-13}$	$1.37 \cdot 10^{-14}$	0.67	0.38	0.56	0.82									

Table 14: Analysis of the 15/5 night. Same as Table (5)

16/5/93	SCIDAR							MESO-NH							Niv=[1-40]
Time window	C_N^{BL}	C_N^{FA}	ϵ_{BL}	ϵ_{FA}	$\frac{\epsilon_{EA}}{\epsilon_{BL}}$	ϵ_{TOT}		C_N^{BL}	C_N^{FA}	ϵ_{BL}	ϵ_{FA}	$\frac{\epsilon_{EA}}{\epsilon_{BL}}$	ϵ_{TOT}		Sim.Time
[00:00-01:00]	-	-	-	-	-	-		$9.29 \cdot 10^{-14}$	$4.02 \cdot 10^{-15}$	0.30	0.04	0.15	0.31		30min
[01:00-02:00]	$1.12 \cdot 10^{-12}$	$6.91 \cdot 10^{-14}$	1.34	0.25	0.18	1.39		$6.55 \cdot 10^{-14}$	$4.07 \cdot 10^{-15}$	0.24	0.04	0.18	0.25		1 ^h
[02:00-03:00]	$1.26 \cdot 10^{-12}$	$4.97 \cdot 10^{-14}$	1.44	0.20	0.14	1.48		$1.11 \cdot 10^{-13}$	$4.29 \cdot 10^{-15}$	0.34	0.04	0.14	0.34		2 ^h
[03:00-04:00]	$1.18 \cdot 10^{-12}$	$4.16 \cdot 10^{-14}$	1.39	0.18	0.13	1.42		$1.25 \cdot 10^{-13}$	$1.25 \cdot 10^{-15}$	0.36	0.36	1.00	0.54		3 ^h
[04:00-05:00]	$1.05 \cdot 10^{-12}$	$2.53 \cdot 10^{-14}$	1.29	0.13	0.10	1.31		$4.68 \cdot 10^{-13}$	$4.27 \cdot 10^{-15}$	0.80	0.04	0.06	0.80		4 ^h
[05:00-06:00]	$8.36 \cdot 10^{-13}$	$2.13 \cdot 10^{-14}$	1.13	0.12	0.11	1.14									
								$1.92 \cdot 10^{-13}$	$34.00 \cdot 10^{-15}$	0.43	0.12		0.48		Mean
[00:00-06:00]	$1.12 \cdot 10^{-12}$	$4.43 \cdot 10^{-14}$	1.35	0.19	0.14	1.38									

Table 15: Analysis of the 16/5 night. Same as Table (5)

17/5/93	SCIDAR							MESO-NH							Niv=[1-40]
Time window	C_N^{BL}	C_N^{FA}	ϵ_{BL}	ϵ_{FA}	$\frac{\epsilon_{EA}}{\epsilon_{BL}}$	ϵ_{TOT}		C_N^{BL}	C_N^{FA}	ϵ_{BL}	ϵ_{FA}	$\frac{\epsilon_{EA}}{\epsilon_{BL}}$	ϵ_{TOT}		Sim.Time
[00:00-01:00]	-	-	-	-	-	-		$4.43 \cdot 10^{-14}$	$2.22 \cdot 10^{-14}$	0.19	0.13	0.66	0.25		30min
[01:00-02:00]	$4.49 \cdot 10^{-13}$	$9.55 \cdot 10^{-14}$	0.77	0.30	0.39	0.87		$4.35 \cdot 10^{-14}$	$3.45 \cdot 10^{-14}$	0.19	0.17	0.87	0.27		1 ^h
[02:00-03:00]	$4.31 \cdot 10^{-13}$	$8.28 \cdot 10^{-14}$	0.76	0.28	0.37	0.84		$2.60 \cdot 10^{-14}$	$3.94 \cdot 10^{-14}$	0.14	0.18	1.28	0.24		2 ^h
[03:00-04:00]	$4.81 \cdot 10^{-13}$	$4.16 \cdot 10^{-14}$	0.81	0.24	0.30	0.87		$4.23 \cdot 10^{-14}$	$3.98 \cdot 10^{-14}$	0.19	0.18	0.96	0.28		3 ^h
[04:00-05:00]	$5.20 \cdot 10^{-13}$	$8.08 \cdot 10^{-14}$	0.85	0.27	0.32	0.92		$4.88 \cdot 10^{-14}$	$3.94 \cdot 10^{-14}$	0.20	0.18	0.88	0.29		4 ^h
[05:00-06:00]	$3.89 \cdot 10^{-13}$	$7.51 \cdot 10^{-14}$	0.71	0.26	0.37	0.79									
								$4.01 \cdot 10^{-14}$	$3.82 \cdot 10^{-14}$	0.18	0.18		0.27		Mean
[00:00-06:00]	$4.63 \cdot 10^{-13}$	$8.02 \cdot 10^{-14}$	0.79	0.27	0.34	0.87									

Table 16: Analysis of the 17/5 night. Same as Table (5)

18/5/93	SCIDAR							MESO-NH							Niv=[1-40]
Time window	C_N^{BL}	C_N^{FA}	ϵ_{BL}	ϵ_{FA}	$\frac{\epsilon_{EA}}{\epsilon_{BL}}$	ϵ_{TOT}		C_N^{BL}	C_N^{FA}	ϵ_{BL}	ϵ_{FA}	$\frac{\epsilon_{EA}}{\epsilon_{BL}}$	ϵ_{TOT}		Sim.Time
[00:00-01:00]	$7.09 \cdot 10^{-13}$	$2.01 \cdot 10^{-13}$	1.02	0.48	0.46	1.19		$4.69 \cdot 10^{-14}$	$2.11 \cdot 10^{-14}$	0.20	0.12	0.61	0.25		30min
[01:00-02:00]	$3.65 \cdot 10^{-13}$	$2.49 \cdot 10^{-13}$	0.68	0.54	0.79	0.94		$7.95 \cdot 10^{-14}$	$2.09 \cdot 10^{-14}$	0.27	0.12	0.45	0.32		1 ^h
[02:00-03:00]	$4.30 \cdot 10^{-13}$	$2.25 \cdot 10^{-13}$	0.75	0.51	0.67	0.97		$9.62 \cdot 10^{-14}$	$2.14 \cdot 10^{-14}$	0.31	0.12	1.40	0.35		2 ^h
[03:00-04:00]	$3.72 \cdot 10^{-13}$	$1.98 \cdot 10^{-13}$	0.69	0.47	0.68	0.90		$3.82 \cdot 10^{-14}$	$2.54 \cdot 10^{-14}$	0.18	0.14	0.78	0.24		3 ^h
[04:00-05:00]	$3.83 \cdot 10^{-13}$	$1.29 \cdot 10^{-12}$	0.70	0.37	0.52	0.84		$3.77 \cdot 10^{-14}$	$2.11 \cdot 10^{-14}$	0.18	0.12	0.71	0.23		4 ^h
[05:00-06:00]	$6.57 \cdot 10^{-13}$	$1.27 \cdot 10^{-13}$	0.97	0.36	0.37	1.08									
								$6.29 \cdot 10^{-14}$	$2.22 \cdot 10^{-14}$	0.23	0.12		0.28		Mean
[00:00-06:00]	$4.19 \cdot 10^{-13}$	$1.92 \cdot 10^{-13}$	0.74	0.46	0.62	0.93									

Table 17: Analysis of the 18/5 night. Same as Table (5)

19/5/93	SCIDAR						MESO-NH						Niv=[1-40]
Time window	C_N^{BL}	C_N^{FA}	ε_{BL}	ε_{FA}	$\frac{\varepsilon_{EA}}{\varepsilon_{BL}}$	ε_{TOT}	C_N^{BL}	C_N^{FA}	ε_{BL}	ε_{FA}	$\frac{\varepsilon_{EA}}{\varepsilon_{BL}}$	ε_{TOT}	Sim.Time
[00:00-01:00]	$2.16 \cdot 10^{-13}$	$5.27 \cdot 10^{-13}$	0.50	0.85	1.70	1.05	$1.76 \cdot 10^{-14}$	$1.18 \cdot 10^{-14}$	0.11	0.09	0.78	0.15	30min
[01:00-02:00]	$4.76 \cdot 10^{-13}$	$1.99 \cdot 10^{-13}$	0.80	0.47	0.59	0.99	$2.81 \cdot 10^{-14}$	$1.20 \cdot 10^{-14}$	0.15	0.09	0.60	0.18	1 ^h
[02:00-03:00]	$2.98 \cdot 10^{-13}$	$1.98 \cdot 10^{-13}$	0.61	0.47	0.78	0.82	$1.69 \cdot 10^{-14}$	$1.20 \cdot 10^{-14}$	0.11	0.09	0.81	0.15	2 ^h
[03:00-04:00]	$3.09 \cdot 10^{-13}$	$1.35 \cdot 10^{-13}$	0.62	0.38	0.61	0.77	$2.50 \cdot 10^{-14}$	$1.23 \cdot 10^{-14}$	0.14	0.09	0.65	0.17	3 ^h
[04:00-05:00]	$2.80 \cdot 10^{-13}$	$1.46 \cdot 10^{-13}$	0.58	0.39	0.67	0.75	$4.41 \cdot 10^{-12}$	$1.21 \cdot 10^{-14}$	0.19	0.09	0.46	0.22	4 ^h
[05:00-06:00]	$3.22 \cdot 10^{-13}$	$1.60 \cdot 10^{-13}$	0.63	0.42	0.65	0.81							
							$2.85 \cdot 10^{-14}$	$1.21 \cdot 10^{-14}$	0.15	0.09		0.18	Mean
[00:00-06:00]	$3.35 \cdot 10^{-13}$	$1.87 \cdot 10^{-13}$	0.65	0.46	0.70	0.85							

Table 18: Analysis of the 19/5 night. Same as Table (5)

23/5/93	SCIDAR						MESO-NH						Niv=[1-40]
Time window	C_N^{BL}	C_N^{FA}	ε_{BL}	ε_{FA}	$\frac{\varepsilon_{EA}}{\varepsilon_{BL}}$	ε_{TOT}	C_N^{BL}	C_N^{FA}	ε_{BL}	ε_{FA}	$\frac{\varepsilon_{EA}}{\varepsilon_{BL}}$	ε_{TOT}	Sim.Time
[00:00-01:00]	$3.13 \cdot 10^{-13}$	$1.32 \cdot 10^{-13}$	0.62	0.37	0.59	0.77	$2.39 \cdot 10^{-15}$	$1.81 \cdot 10^{-13}$	0.13	0.45	3.37	0.48	30min
[01:00-02:00]	$2.22 \cdot 10^{-13}$	$1.31 \cdot 10^{-13}$	0.51	0.37	0.72	0.67	$5.83 \cdot 10^{-14}$	$1.35 \cdot 10^{-13}$	0.23	0.38	1.65	0.47	1 ^h
[02:00-03:00]	$1.72 \cdot 10^{-13}$	$1.13 \cdot 10^{-13}$	0.43	0.34	0.77	0.59	$3.14 \cdot 10^{-14}$	$8.70 \cdot 10^{-14}$	0.16	0.29	1.84	0.35	2 ^h
[03:00-04:00]	$1.42 \cdot 10^{-13}$	$1.44 \cdot 10^{-13}$	0.39	0.39	1.00	0.59	$1.69 \cdot 10^{-14}$	$1.69 \cdot 10^{-13}$	0.11	0.43	3.97	0.46	3 ^h
[04:00-05:00]	$2.90 \cdot 10^{-13}$	$1.14 \cdot 10^{-13}$	0.60	0.34	0.57	0.73	$7.79 \cdot 10^{-14}$	$1.52 \cdot 10^{-13}$	0.27	0.40	1.49	0.52	4 ^h
[05:00-06:00]	$3.76 \cdot 10^{-13}$	$7.93 \cdot 10^{-14}$	0.70	0.27	0.39	0.78							
							$4.61 \cdot 10^{-14}$	$13.57 \cdot 10^{-14}$	0.19	0.37		0.45	Mean
[00:00-06:00]	$2.29 \cdot 10^{-13}$	$1.25 \cdot 10^{-13}$	0.52	0.36	0.69	0.67							

Table 19: Analysis of the 23/5 night. Same as Table (5)

25/5/93	SCIDAR						MESO-NH						Niv=[1-40]
Time window	C_N^{BL}	C_N^{FA}	ε_{BL}	ε_{FA}	$\frac{\varepsilon_{EA}}{\varepsilon_{BL}}$	ε_{TOT}	C_N^{BL}	C_N^{FA}	ε_{BL}	ε_{FA}	$\frac{\varepsilon_{EA}}{\varepsilon_{BL}}$	ε_{TOT}	Sim.Time
[00:00-01:00]	$6.35 \cdot 10^{-14}$	$9.19 \cdot 10^{-14}$	0.24	0.30	1.24	0.41	$1.60 \cdot 10^{-14}$	$2.16 \cdot 10^{-14}$	0.10	0.12	1.19	0.17	30min
[01:00-02:00]	$5.34 \cdot 10^{-14}$	$8.27 \cdot 10^{-14}$	0.21	0.28	1.29	0.38	$6.79 \cdot 10^{-14}$	$2.17 \cdot 10^{-14}$	0.25	0.12	0.50	0.30	1 ^h
[02:00-03:00]	$6.46 \cdot 10^{-14}$	$9.78 \cdot 10^{-14}$	0.24	0.31	1.28	0.42	$1.88 \cdot 10^{-13}$	$2.17 \cdot 10^{-14}$	0.46	0.12	0.27	0.49	2 ^h
[03:00-04:00]	$5.72 \cdot 10^{-14}$	$6.54 \cdot 10^{-14}$	0.22	0.24	1.08	0.35	$8.34 \cdot 10^{-14}$	$2.17 \cdot 10^{-14}$	0.28	0.12	0.44	0.32	3 ^h
[04:00-05:00]	$5.10 \cdot 10^{-14}$	$4.62 \cdot 10^{-14}$	0.21	0.19	0.94	0.31	$1.58 \cdot 10^{-13}$	$2.19 \cdot 10^{-14}$	0.42	0.13	0.30	0.45	4 ^h
[05:00-06:00]	-	-	-	-	-	-							
							$12.43 \cdot 10^{-14}$	$2.17 \cdot 10^{-14}$	0.35	0.12		0.39	Mean
[00:00-06:00]	$5.93 \cdot 10^{-14}$	$8.28 \cdot 10^{-14}$	0.23	0.28	1.22	0.39							

Table 20: Analysis of the 25/5 night. Same as Table (5)

References

- [1] M. Sarazin, F. Roddier “The ESO differential image monitor”, *A&A* **227**, pp.294-300, 1990

- [2] J. Vernin, M. Azouit "Traitement d'Image adapte au Speckle atmospherique. I. Formation du speckle en atmosphere turbulente. Proprietes statistiques", *J. Optics (Paris)*, **14**, 5-9, (1983)
- [3] J. Vernin, M. Azouit "Traitement d'Image adapte au Speckle atmospherique. II. Analyse multidimensionnelle appliquee au diagnostic a distance de la turbulence", *J. Optics (Paris)*, **14**, 131-142, (1983)
- [4] F. Roddier "The effects of atmospheric turbulence in optical astronomy", *Progress in Optics*, **Vol. XIX**, no. 18, pp. 283-376, 1981
- [5] F. Murtagh, M. Sarazin "Nowcasting Astronomical Seeing: a study of ESO La Silla and Paranal" P.A.S.P., bf 105 932-939 (1993)
- [6] A. Aussem, F. Murtagh, M. Sarazin "Dynamical recurrent neural networks and pattern recognition methods for time series prediction: application to seeing and temperature forecasting in the context of ESO's VLT astronomical weather station" *Vistas in Astronomy* **38**, 357-374 (1994)
- [7] The Messenger (October 97)
- [8] J. Vernin "Astronomical site selection: a new meteorological approach" - Proceedings "Advanced Technology Optical Telescopes III" - 3-6 March 1986 Tucson, Arizona
- [9] L. Valenziano "Astronomical seeing estimation in Antartica", *Exp. Astr.*, in press.
- [10] JZ. Benkhaldoun, A. Jabiri, J. Vernin "Attempt to access an astronomical seeing using a model forecast", *Exp. Astr.*, submitted
- [11] C. Coulman, J. Vernin, Y. Coqueugniot, J. L. Caccia "Outer scale of turbulence appropriate to modeling refractive-index structure profiles" *Appl. Opt.* **27**, 155-160 (1988)
- [12] T. E. VanZandt, J. L. Green, K. S. Gage and W. L. Clark "Vertical profiles of refractivity turbulence structure constant: comparison of observations by the Sunset Radar with a new theoretical model" *Radio Science* **13**, 819-829 (1978)
- [13] T. E. VanZandt, K. S. Gage and J. M. Warnock "An improved model for the calculation of profiles of C_N^2 and ϵ in the free atmosphere from background profiles of wind, temperature and humidity" 20th Conference on Radar Meteorology, 30 Nov./3 Dec. 1981, published by the American Meteorological Society, Boston
- [14] P. Y. Bely "Forecasting seeing: a first step", ESO Workshop on Site Testing for future large telescopes, La Silla, 4-6 October 20th Conference on Radar Meteorology, 30 Nov./3 Dec. 1981, published by the American Meteorological Society, Boston

- [15] C. Couleman, P. R. Gillingham "The observation, Calculation and Possible forecasting of astronomical seeing" P.A.S.P. **98**, 376-387 (1986)
- [16] P. Bougeault, C. De Hui, B. Fleury, J. Laurent "Investigation of the seeing by means of an atmospheric meso-scale numerical simulation" Appl. Opt. **34**, 3481-3488 (1995)
- [17] C. Couleman, J. Vernin, A. Fuchs "Optical seeing - mechanism of formation of thin turbulent laminae in the atmosphere" Applied Optics **34**, 5461-5474 (1995)
- [18] H. Tennekes and J. L. Lumley "A first course in Turbulence" The Mit Press(1986)
- [19] Meteorological Monographs "Atmospheric processes over complex terrain" Ed. Blumen **23** (1990)
- [20] V.I.Tatarski "Wave propagation in a turbulent medium" (1968)
- [21] S. di Serego Alighieri "Observing Modes for the Italian Galileo Telescope" - New Observing Modes for the Next Century" - ASP Conference Series, Vol.87, 1996
- [22] S. Di Serego Alighieri "Instrumentation and observing techniques from Galilei to the TNG" 3G Conference (1997)
- [23] E. Masciadri, J. Vernin, P. Bougeault "Progress Report - ESO Contract: 47724/VLT/96/6384/MST - *Feasibility study of seeing prevision using the Meso-Nh meteorological model*" March 1997
- [24] J. P. Lafore, J. Stein, N. Asencio, P. Bougeault, V. Ducrocq, J. Duron, C. Fischer, P. Hereil, P. Mascart, J. P. Pinty, J. L. Redelsperger, E. Richard, J. Vila-Guerau de Arellano, "The Meso-Nh atmospheric simulation System. Part I:Adiabatic Formulation and control simulation" in *Annales Geophysicae*
- [25] P. Bougeault, P. Lacarrere "Parameterization of Orography-Induced Turbulence in a Meso-Scale Model" Mon. Wea. Rev. **117**, 1872-1890 (1995)
- [26] J. Cuxart, P. Bougeault and J-L. Redelsperger "Turbulence closure for a non-hydrostatic model" 11th Symp. Boundary Layers & Turb., bf 13 409-412, (1995)
- [27] J.L Redelsperger, G. Sommeria "Methode de representation de la turbulence d'echelle inferieure a la maille pour un model tri-dimensionnel de convection nuageuse" in *Boundary Layer Met.*, bf 21 509-530 (1981)
- [28] J.C. Wyngaard, Y. Izumi, S.A. Collins "Behaviour of the refractive-Index-Structure Parameter near the ground" in *JOSA*, bf 61 1646-1650 (1971)
- [29] J. C. Andre, G. de Moor, P. Lacarrere, R. du Vachat "Modeling the 24-hour evolution of the mean and turbulent structures of the planetary layer", *J. Atmos. Sci.*, bf 35 1861-1883 (1978)

- [30] F. Roddier, J. M. Gilli, J. Vernin “On the isoplanetic patch size in stellar speckle interferometry” *J. Optics of Paris*, **13**, 63-70, (1982)
- [31] D.L.Fried, *Optica Acta*, **26**, 597 (1979)
- [32] F. Roddier, J. M. Gilli, G. Lund “On the origin of speckle boiling and its effects in stellar speckle interferometry” *J. Optics of Paris*, **13**, 263-271, (1982)
- [33] F. Morand, C. Piriou “Guide à l’usage des utilisateurs du model Arpege” Service Central D’Exploitation de la Meteorologie (SCEM)- METEO FRANCE
- [34] “User Guide to ECMWF products”-
- [35] C. Munoz-Tunon, J. Vernin, A. M. Varela “Night-time image quality at Roque de Los Muchachos Observatory” *A&A Supplement Series*, **125**, 183-193, (1997)
- [36] R. Benzi, R. Deidda,, M. Marrocu, A. Speranza “Feasibility Study of a Meteorological Prediction Model for ESO Observatories in Chile” Report VLT-TRE-CRS-17443-0001/2, July 1996/April 1997

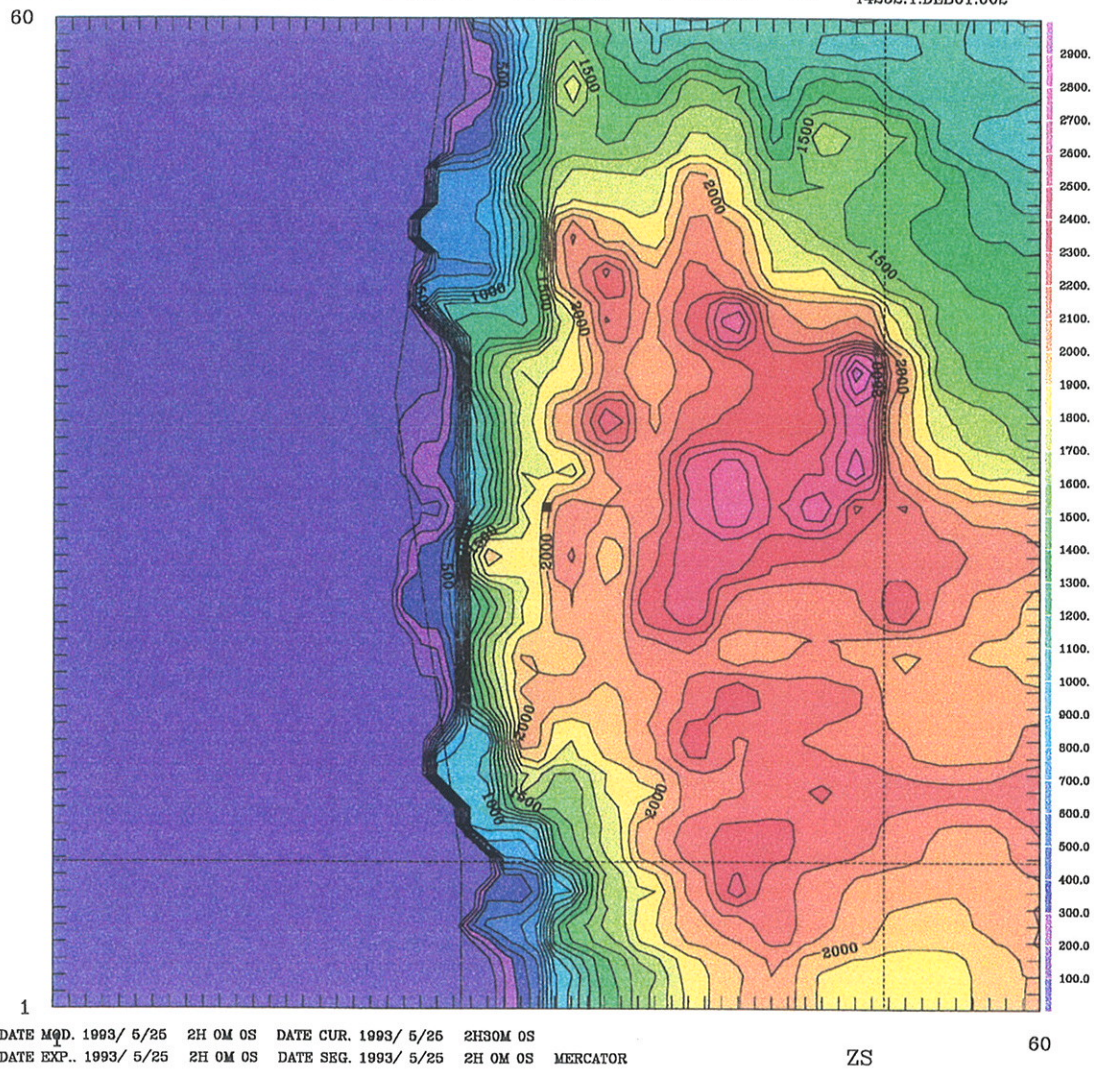


Figure 1: PGDANDES: Orographic model extracted from GLOBE - 60 x 60 grid points - 120 x 120 km - 2000 x 2000 m resolution. Paranal location is indicated by a black square.

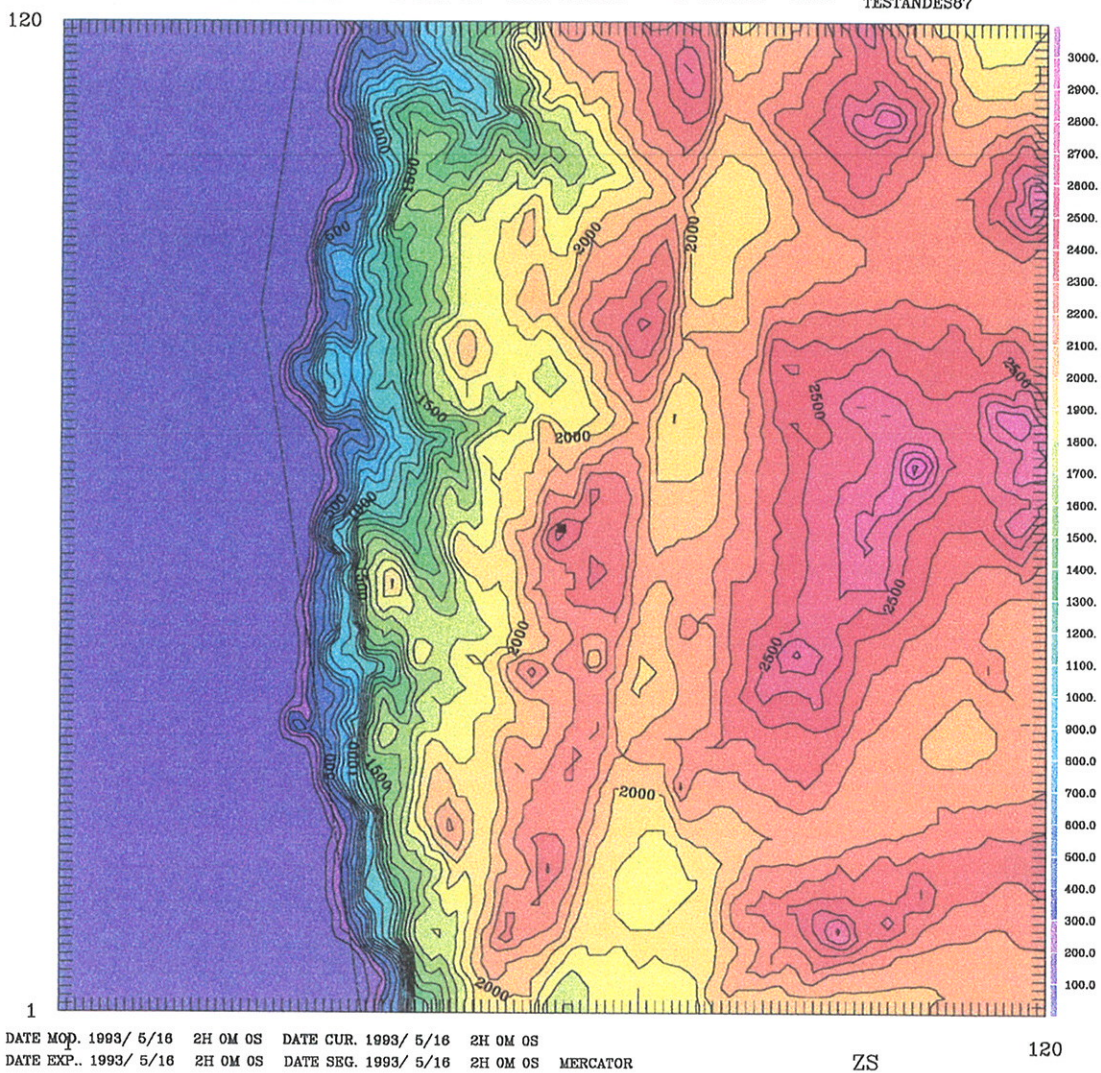


Figure 2: PGDANDES8: Orographic model extracted from a digitized map - 120 x 120 grid points - 60 km x 60 km - 500 m x 500 m resolution. Paranal location is indicated by a black square.

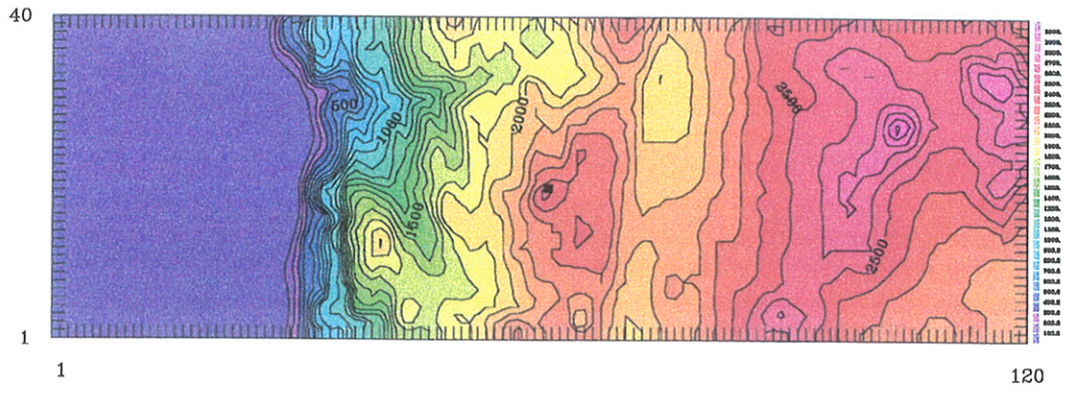


Figure 3: PGDANDES9: As Fig.(2) - 120 x 40 grid points - 60 km x 20 km - 500 m x 500 m resolution. Paranal location is indicated by a black square



Figure 4: PGDANDES10: As Fig.(2) - 60 x 20 grid points - 60 km x 20 km - 1000 m x 1000 m resolution. Paranal location is indicated by a black square

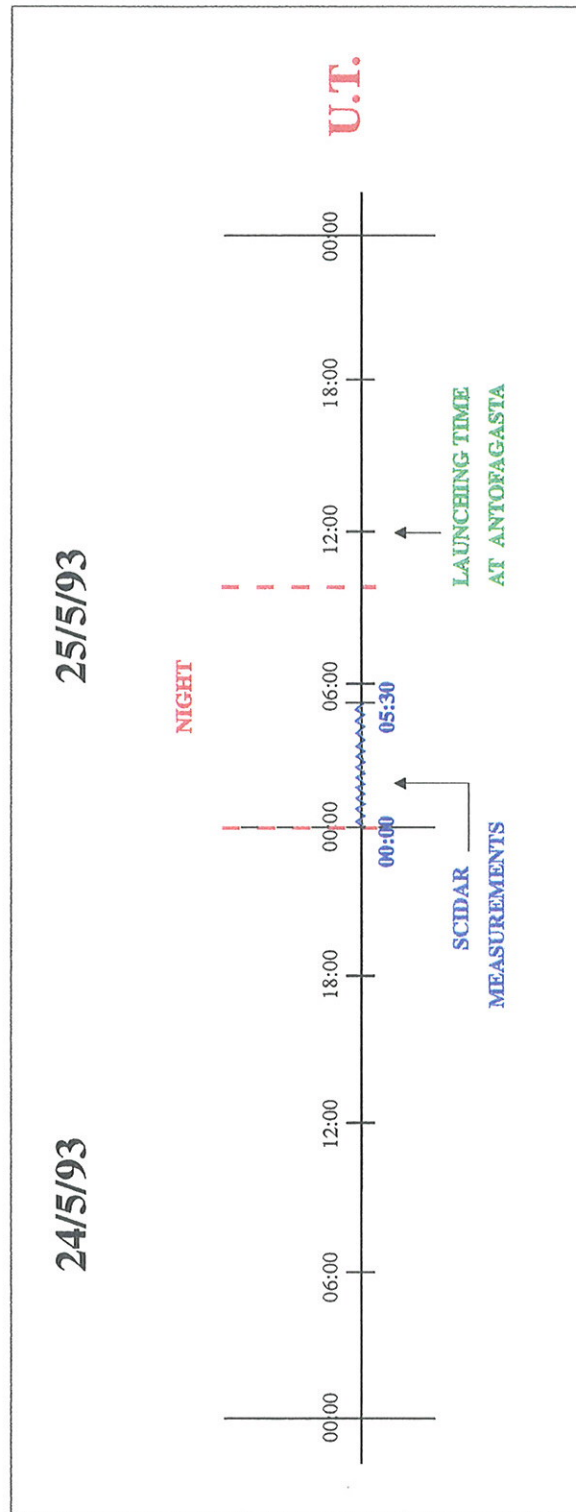


Figure 5: Observation time. Blue temporal window [00:00-05:30] indicates the time at which Scidar measurements took place during each night over the whole campaign. The red lines indicate the astronomical night.


```

&NAM_REAL_PGD CPGD_FILE='PGDANDES9',
LREAD_ZS = .TRUE., LREAD_ZOREL = .FALSE.,
LREAD_ZOVEG = .TRUE., LREAD_RAD_PARAM = .TRUE.,
LREAD_VEG_PARAM = .TRUE., LREAD_GROUND_PARAM = .TRUE. /
&NAM_DIMn_PRE NIMAX=120, NJMAX=40, NKMAX=40 /
&NAM_CONF_PRE LCARTESIAN=.FALSE., LBOUSS=.FALSE.,
L2D=.FALSE., L1D=.FALSE.,
CIDEAL='RSOU',
LPERTURB=.FALSE., NVERB=5 /
&NAM_CONFn LUSERV=.TRUE., NSV = 0 /
&NAM_GRID_PRE XLAT0 = -24.61, XLON0 = -70.4,
XRFK = 0., XBETA = 0. /
&NAM_GRIDn_PRE CZGRID_TYPE = 'FUNCTN', XDZGRD=50., XDZTOP=600.,
XZMAX_STRGRD=3000., XSTRGRD=30., XSTRTOP=0.,
XLATCEN = -24.61, XLONCEN = -70.4 /
&NAM_LUNITH CINIFILE='X165V2' /
&NAM_POST_PRE /
&NAM_DYNn_PRE /
&NAM_LBCn_PRE CLBCX(1)='OPEN', CLBCX(2)='OPEN',
CLBCY(1)='OPEN', CLBCY(2)='OPEN' /
&NAM_VPROF_PRE CTYPELOC='IJGRID', NILOC=20, NJLOC=20,
CFUNU='ZZZ', CFUNV='ZZZ',
LGEOSBAL=.TRUE. /
&NAM_Grn_PRE CSURF='TSZ0', ZOREL=0.1, SST=288.4, XETS=1., XHUG=0.2 /
1993 05 16 0.
'STANDARD'
120.3571
100000.0
302.2200
281.7534
15
100000.0 180.5334 2.970152
92500.00 178.5868 2.750891
85000.00 194.5630 1.229715
70000.00 358.7872 5.011208
50000.00 198.1834 7.580033
40000.00 180.0798 13.71003
30000.00 200.0004 14.82738
25000.00 223.3562 15.50598
20000.00 223.1112 26.94090
15000.00 235.7448 33.36119
10000.00 246.8536 18.83461
7000.000 253.6958 8.980802
5000.000 254.1208 1.060424
3000.000 338.5658 8.961808
1000.000 357.0905 8.150828
15
92500.00 298.1600 275.7214
85000.00 293.8200 269.4320
70000.00 282.7100 260.2862
50000.00 266.5100 243.7736
40000.00 253.3100 230.5608
30000.00 237.3500 217.2408
25000.00 227.1400 208.4734
20000.00 216.1000 207.4415
15000.00 207.4500 199.5349
10000.00 199.7600 191.0163
7000.000 204.1700 189.6216
5000.000 209.8200 187.4992
3000.000 219.2000 184.2774
1000.000 235.8800 177.1429

```

Figure 6: Pre-processing namelist

```

&NAM_LUNItN CINIFILE = "S16SV2" /
&NAM_CONFh LUSERV = T, LUSERR = F, LUSERI = F, LUSERS = F,
  LUSERG = F, LUSERH = F, NSV = 0 /
&NAM_DYNh XTSTEP = 2.5, CPRESOPT = "RICHA", NITR = 4, XRELAX = 1.,
  LHO_RELAX = T, LVE_RELAX = T, NRIX = 5, NRIMY = 3, XIRIMMAX = .00166,
  XT4DIFF = 1500. /
&NAM_ADVh /
&NAM_PARAMh CTURB = "TKEL", CRAD = "NONE", CDRAG = "NONE", CGROUND = "TSZ0",
  CLOUD = "NONE" /
&NAM_PARAM_RADN /
&NAM_LBCn CLBCX = 2*"OPEN", CLBCY = 2*"OPEN", NLBLX = 2*1, NLBLY = 2*1,
  XCPHASE = 20. /
&NAM_OUTh XOUT1 = 1800., XOUT2 = 3600. /
&NAM_TURBh XIMPL = 1., CTURBLEN = "BL89", CTUREDIM = "1DIM", LTURB_DIAG = T,
  LTURB_FLX = F /
&NAM_CONF CCONF = "START", LTHINSHELL = T, L2D = F, L1D = F, LFLAT = F, IMODEL = 1,
  NVERB = 1, CEXP = "S16V2", CSEG = "DEB01" /
&NAM_DYN XSEGLN = 3600., XASSELIN = 0.2, LCORIO = T, XALKTOP = 0.005,
  XALZBOT = 12570., LNUMDIFF = .T. /
&NAM_BUDGET CBUTYPE = "NONE" /
&NAM_BU_RU LBU_RU = .FALSE. /
&NAM_BU_RV LBU_RV = .FALSE. /
&NAM_BU_RW LBU_RW = .FALSE. /
&NAM_BU_RTH LBU_RTH = .FALSE. /
&NAM_BU_RTKE LBU_RTKE = .FALSE. /
&NAM_BU_RSV1 LBU_RSV1 = .FALSE. /
&NAM_BU_RRV LBU_RRV = .FALSE. /
&NAM_BU_RRC LBU_RRC = .FALSE. /
&NAM_BU_RRR LBU_RRR = .FALSE. /
&NAM_BU_RRI LBU_RRI = .FALSE. /
&NAM_BU_RRS LBU_RRS = .FALSE. /
&NAM_BU_RRG LBU_RRG = .FALSE. /
&NAM_BU_RRH LBU_RRH = .FALSE. /
&NAM_LES /

```

Figure 7: Simulation namelist

```

&NAM_GETh LGETALLT = T, CGETUT = "READ", CGETVT = "READ", CGETWT = "READ",
  CGETTHT = "READ", CGETTKET = "READ", CGETRVT = "READ",
  CGETUM = "READ", CGETVM = "READ", CGETWM = "READ",
  CGETTHM = "READ", CGETRVM = "READ",
  CGETRCT = "READ", CGETRRT = "READ", CGETRIT = "READ", CGETRST = "READ",
  CGETRGT = "READ", CGETRHT = "READ", CGETSVT = 20*"READ", CGETPHIT = "READ" /
&NAM_DOMAIN_POS LHORIZ = .F., LVERTI = .T., NIDEBCOU = 20, NJDEBCOU = 20, NLANGLE = 0,
  NLMAX = 80, XHMIN = 0., XHMAX = 20000. /
&NAM_DIRTRA_POS
NIMNMX = 0, LCOLAREA = .F., LCOLINE = .F., XTHINT = 1., XUINT = 2.,
XWINT = .5, XTKEINT = .1,
NISKIP = 2, XVHC = -20., XVRL = 0.2, XAMX = 0.2 /

```

Figure 8: Post-processing namelist

FILENAME	Orographic Model Res.(m)	Meso-Nh Horiz. Res. (m)	Geog. Surface (km)	Grid Point Number
PGDANDES	5000 x 5000	2000 x 2000	120 x 120	60 x 60
PGDANDES6	500 x 500	1000 x 1000	80 x 80	80 x 80
PGDANDES8	500 x 500	500 x 500	60 x 60	120 x 120
PGDANDES9	500 x 500	500 x 500	60 x 20	120 x 40
PGDANDES10	500 x 500	1000 x 1000	60 x 20	60 x 20

Table 21: Orographic model resolution. List of binary files created for simulations at different horizontal resolutions.

DATE /593	e SEEING AVERAGE	RADIOSOUNDINGS - 12:00 U.T.					ANALYSIS - 00:00 U.T.					ANALYSIS - 06:00 U.T.				
		V 850 mb	V 700 mb	V 500 mb	V 200 mb		V 850 mb	V 700 mb	V 500 mb	V 200 mb		V 850 mb	V 700 mb	V 500 mb	V 200 mb	
13	0.87	✓	✓	✓	✓		✓	✓	✓	✓		✓	✓	✓	✓	
14	0.99	✓	✓	✓	✓		✓	✓	✓	✓		✓	✓	✓	✓	
15	0.81	✓	✓	✓	✓		✓	✓	✓	✓		✓	✓	✓	✓	
16	1.38	✓	✓	✓	✓		✓	✓	✓	✓		✓	✓	✓	✓	
17	0.83	✓	✓	✓	✓		✓	✓	✓	✓		✓	✓	✓	✓	
18	0.93	✓	✓	✓	✓		✓	✓	✓	✓		✓	✓	✓	✓	
19	0.80	✓	✓	✓	✓		✓	✓	✓	✓		✓	✓	✓	✓	
20	0.43															
21	0.67															
22	0.67															
23	0.66	✓	✓	✓	✓		✓	✓	✓	✓		✓	✓	✓	✓	
24	0.63															
25	0.38	✓	✓	✓	✓		✓	✓	✓	✓		✓	✓	✓	✓	
26	0.57	✓	✓	✓	✓		✓	✓	✓	✓		✓	✓	✓	✓	

Table 22: Summary of results from the PARSCA93 campaign. Same as Table(23)

DATE	ANALYSIS - 12:00 U.T.				ANALYSIS - 18:00 U.T.			
	V 850 mb	V 700 mb	V 500 mb	V 200 mb	V 850 mb	V 700 mb	V 500 mb	V 200 mb
13	↖	↖	↖	↖	↖	↖	↖	↖
14	↖	↖	↖	↖	↖	↖	↖	↖
15	↖	↖	↖	↖	↖	↖	↖	↖
16	↖	↖	↖	↖	↖	↖	↖	↖
17	↖	↖	↖	↖	↖	↖	↖	↖
18	↖	↖	↖	↖	↖	↖	↖	↖
19	↖	↖	↖	↖	↖	↖	↖	↖
20	↖	↖	↖	↖	↖	↖	↖	↖
21	↖	↖	↖	↖	↖	↖	↖	↖
22	↖	↖	↖	↖	↖	↖	↖	↖
23	↖	↖	↖	↖	↖	↖	↖	↖
24	↖	↖	↖	↖	↖	↖	↖	↖
25	↖	↖	↖	↖	↖	↖	↖	↖
26	↖	↖	↖	↖	↖	↖	↖	↖

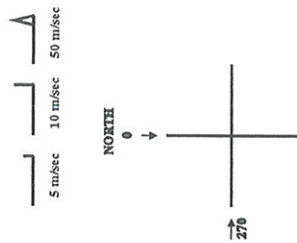


Table 23: Summary of meteorological conditions during the PARSCA93 campaign. Wind direction and amplitude, corresponding to four different pressure levels, is described with arrows. The 200 mb pressure corresponds to the upper levels of the atmosphere (about 12km), i.e. the free atmosphere, whereas the 850 mb pressure corresponds to low levels influenced by heat energy transfer and orographic effects. Antofagasta radiosoundings at 12:00 U.T. and ECMWF analysis at 00:00 U.T., 06:00 U.T., 12:00 U.T. and 18:00 U.T. in the (289.6875,-23.625) grid point are reported. In the first column are reported the night dates of the whole campaign. In the second column we provide the averaged seeing measured by the SCIDAR during the different nights.

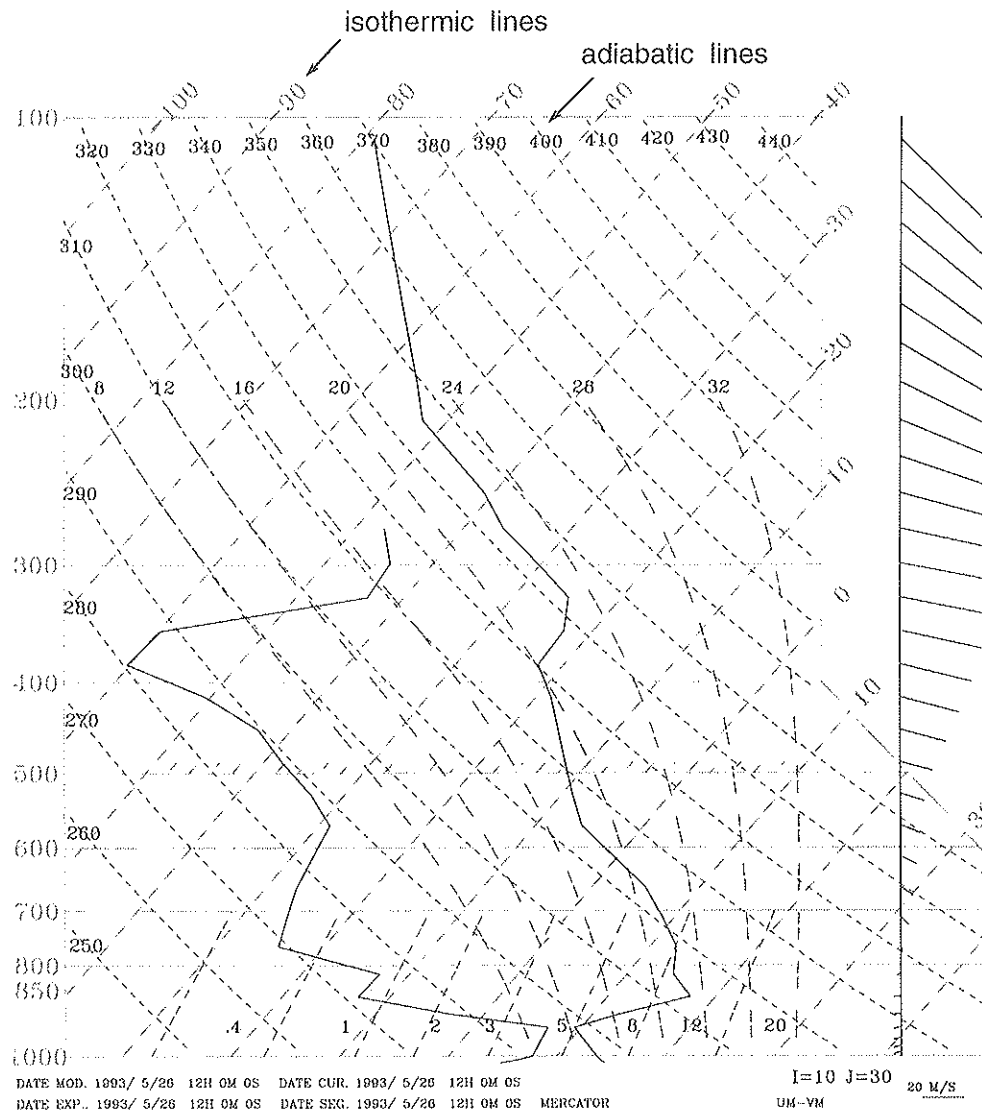


Figure 9: Radiosounding emagram - 26/5/93 at 12:00 T.U. An emagram is a characteristic thermodynamic diagram used by meteorological stations for the graphic description of the atmosphere state. The pressure is reported on the y coordinate. The isothermic lines are inclined to 45 degrees and have a linear scale. The adiabatic lines are represented by dashed, bent, transverses lines. The left line represent the dew point temperature and the right line the absolute temperature. The regions in which the absolute temperature is parallel to the adiabatic lines corresponds to dynamic instability regions. On the right side of figure is reported the wind direction and intensity along on the West-East direction.

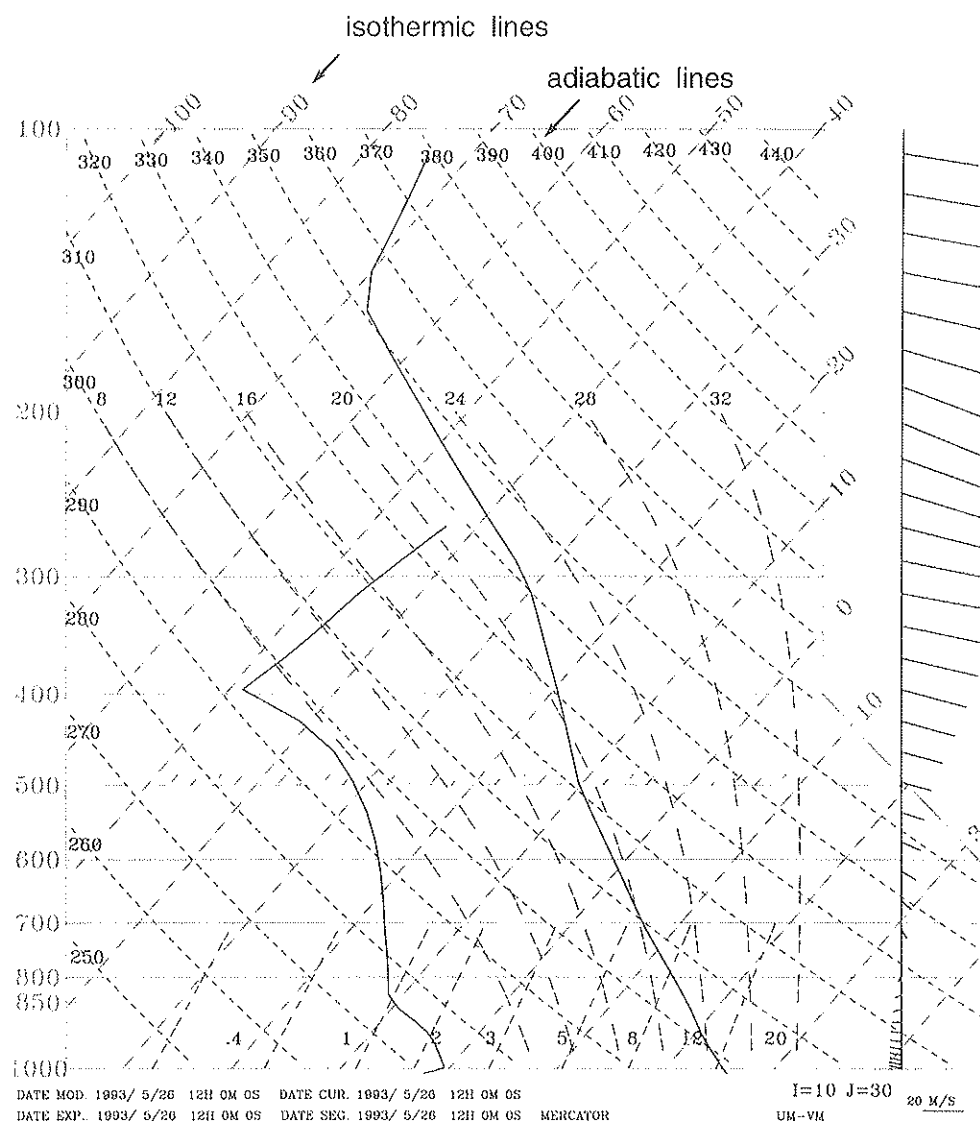


Figure 10: Analysis emagram - 26/5/93 at 12:00 T.U. - Same as Fig(9)

Wind (m/sec) Comparison ECMWF analyses Antofagasta radiosoundings	corr	err (m/s)	err (m/s)
	0.981	-0.36	2.11

Table 24: Wind intensity (m/sec) comparison between Antofagasta radiosoundings and ECMWF analyses during 1993 year. Averages of daily correlations, mean errors and mean absolute errors [36].

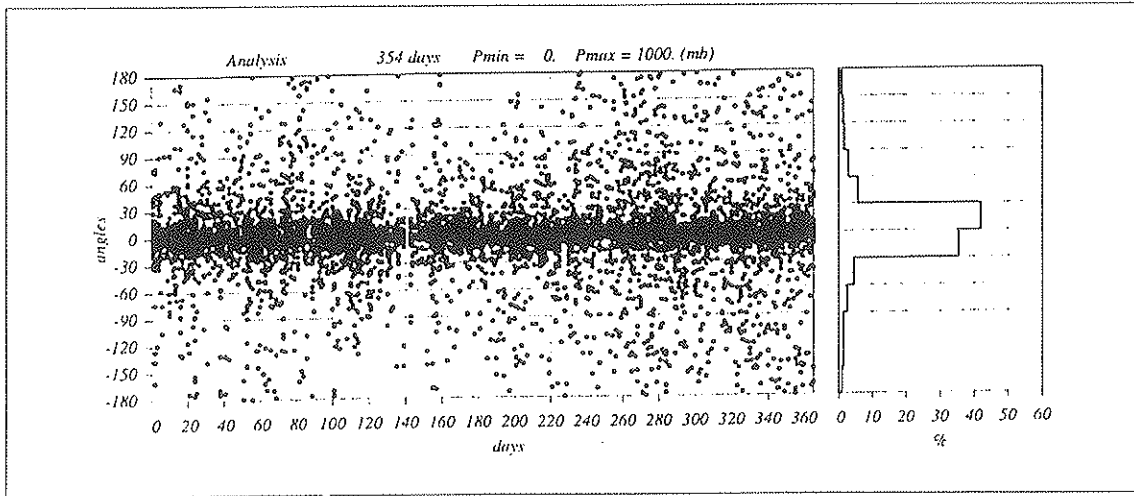


Figure 11: Wind direction comparison between Antofagasta radiosoundings and ECMWF analyses during 1993 year (12:00 U.T.).

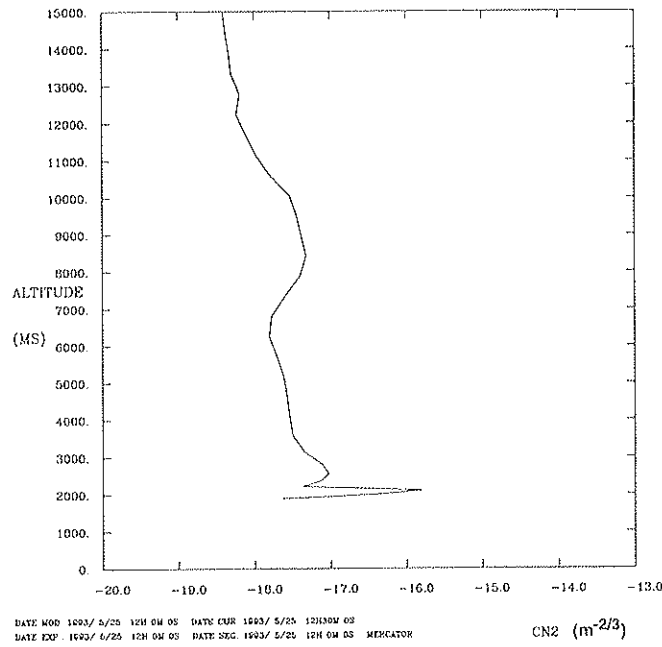


Figure 12: 25/5/93 night - C_N^2 vertical profile above Paranal mountain. Initialization with Antofagasta radiosounding at 12:00 U.T. Simulation time: 30 min

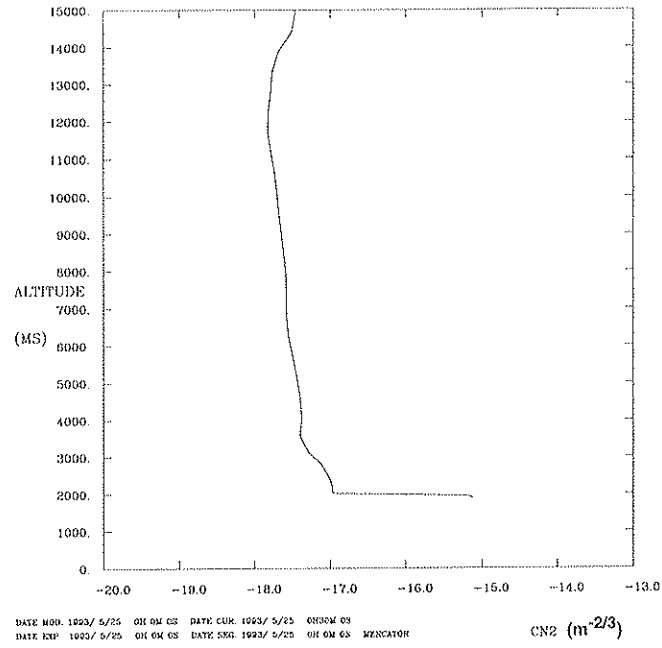


Figure 13: **25/5/93 night** - C_N^2 vertical profile above Paranal mountain. Initialization with ECMWF Analysis at 00:00 U.T. (grid point(-23.625,289.6875)) Simulation time: **30 min**

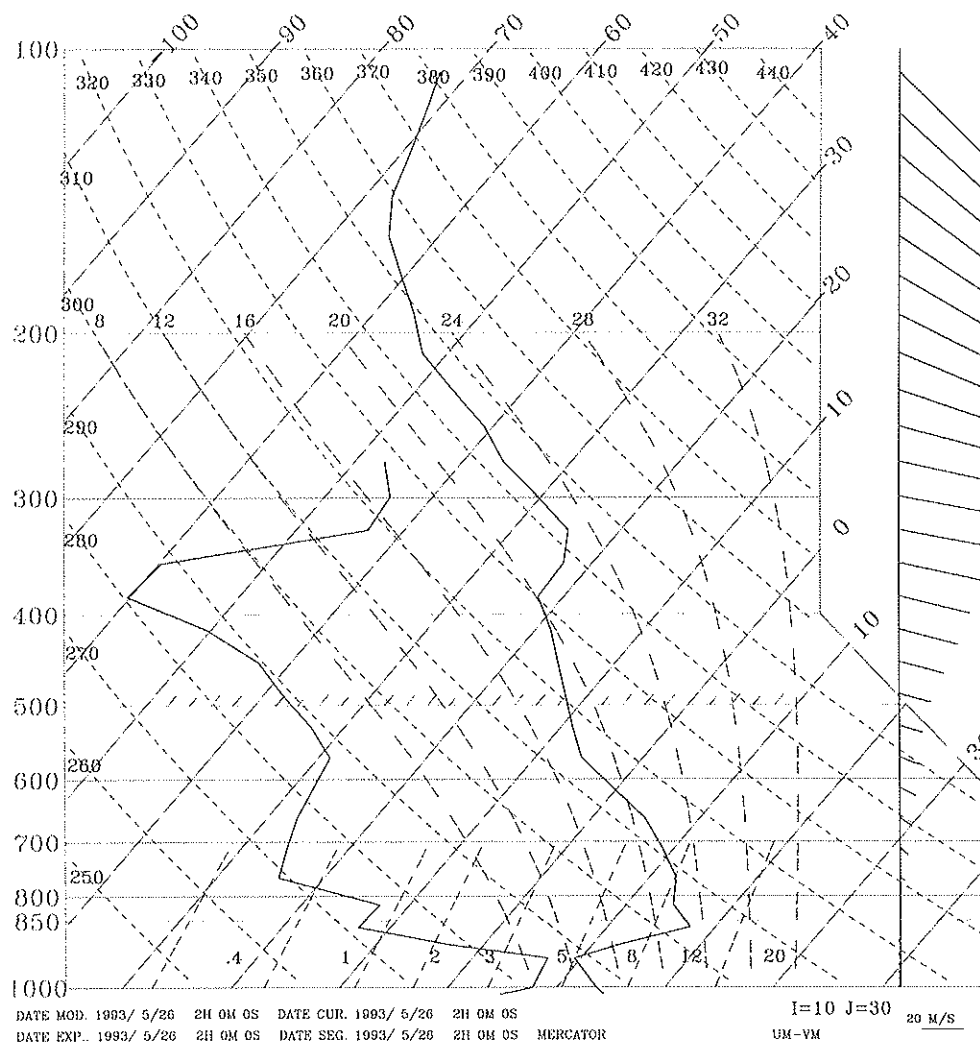


Figure 14: Initialization Emagram (as Fig.(9)) - 26/5/93. The radiosounding temperature profile (1000 *mb* – 150 *mb*) is corrected at high levels (over 150*mb*) by the analysis data. In the low atmosphere levels (1000 *mb* – 750 *mb*) the analysis wind direction and amplitude are used.

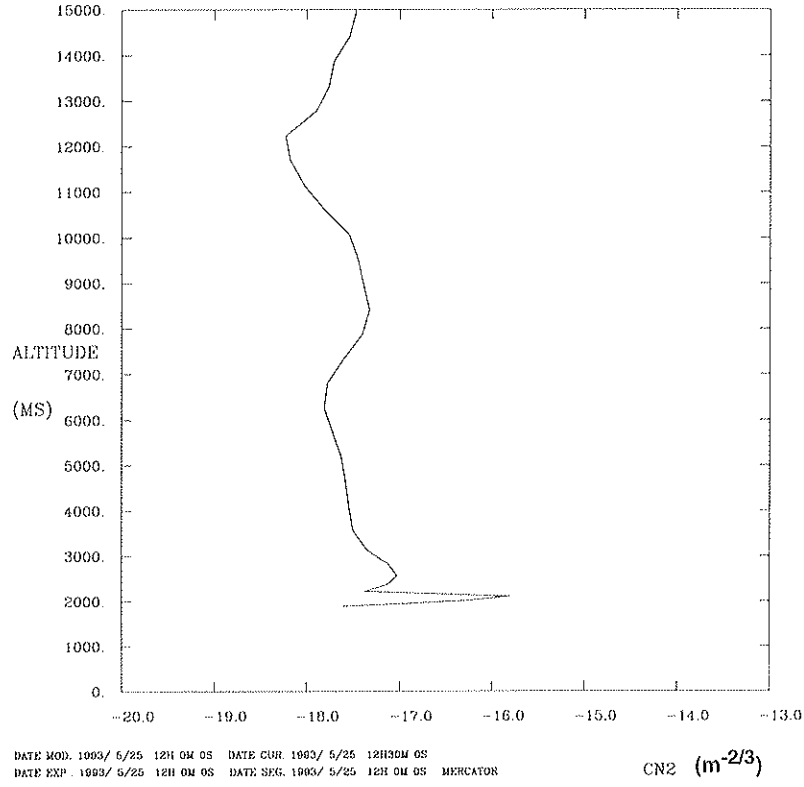


Figure 15: **25/5/93** - C_N^2 vertical profile above Paranal mountain. Initialization with the emagram of Fig.(14) Simulation time: **30 min**

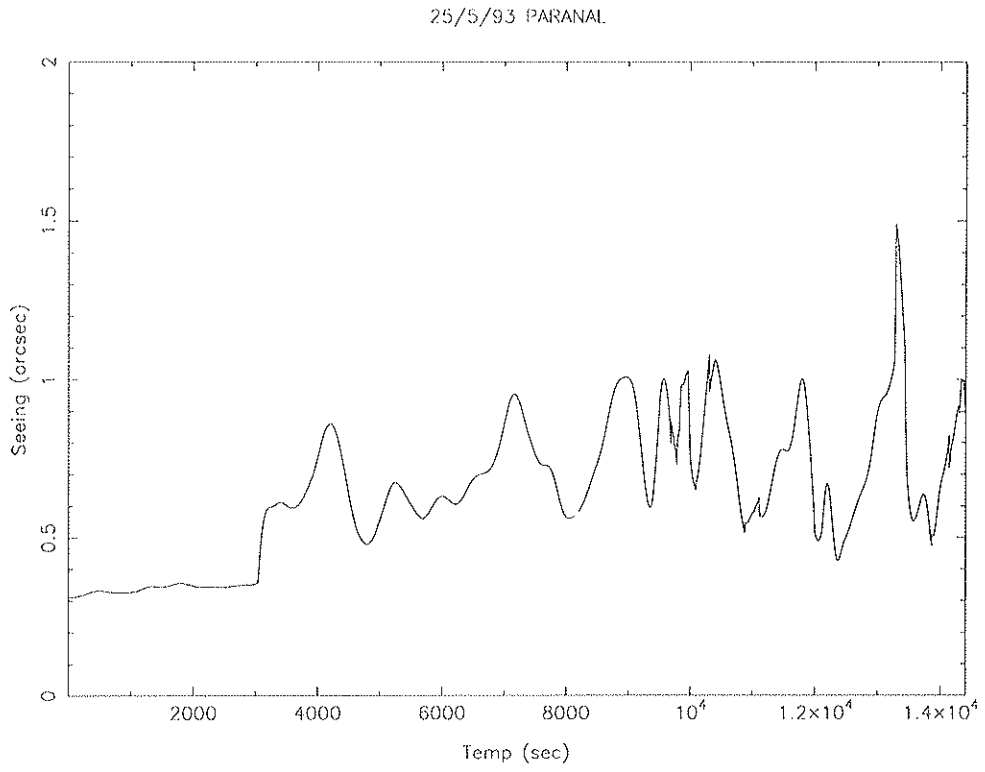


Figure 16: 4 h time seeing evolution over Paranal on **25/5/93**

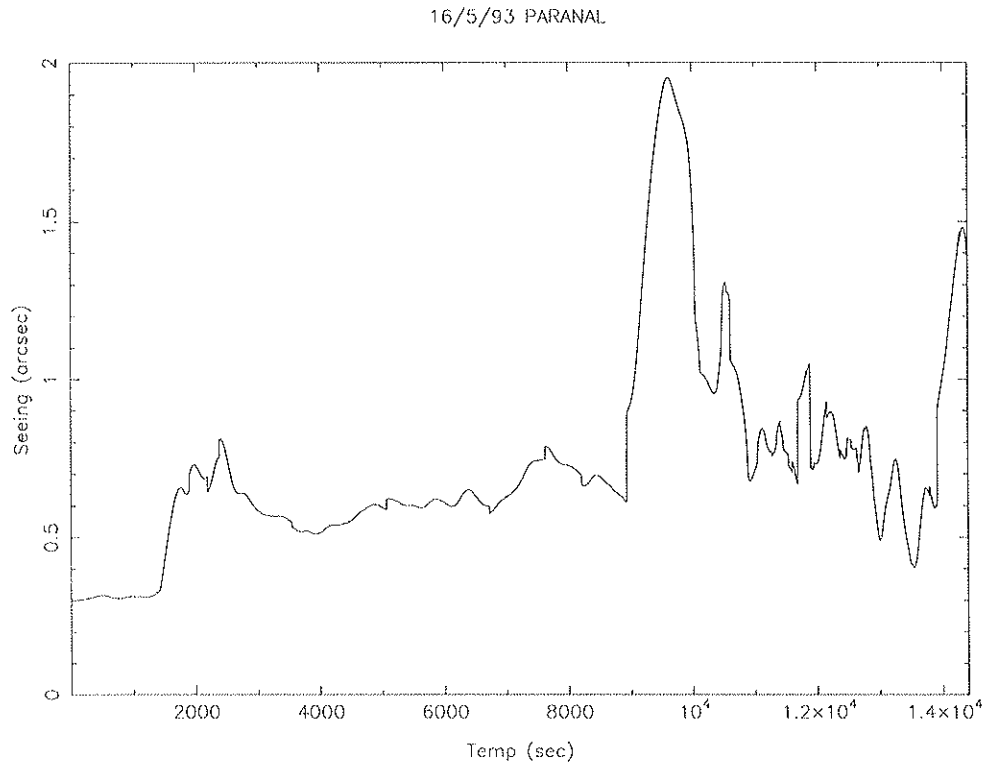


Figure 17: 4 h time seeing evolution over Paranal on **16/5/93**

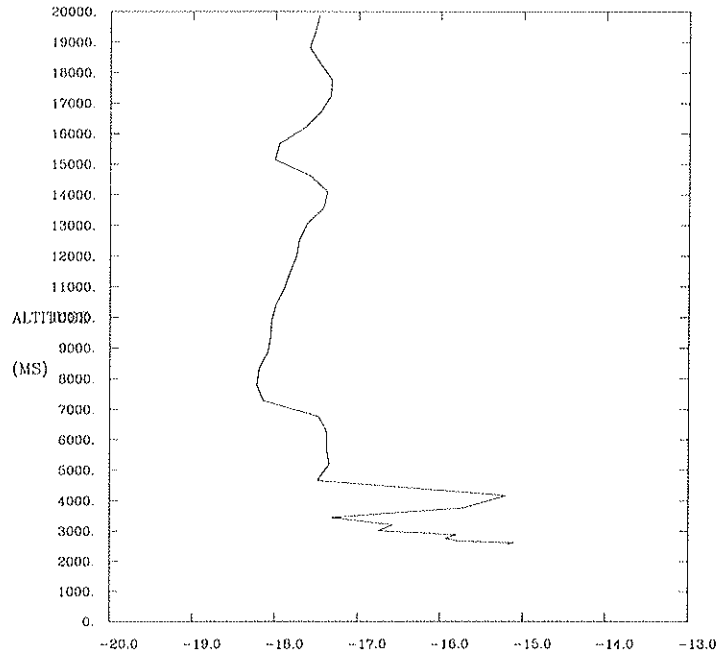


Figure 18: **16/5/93** C_N^2 vertical profile above Paranal mountain after 4 h simulation time

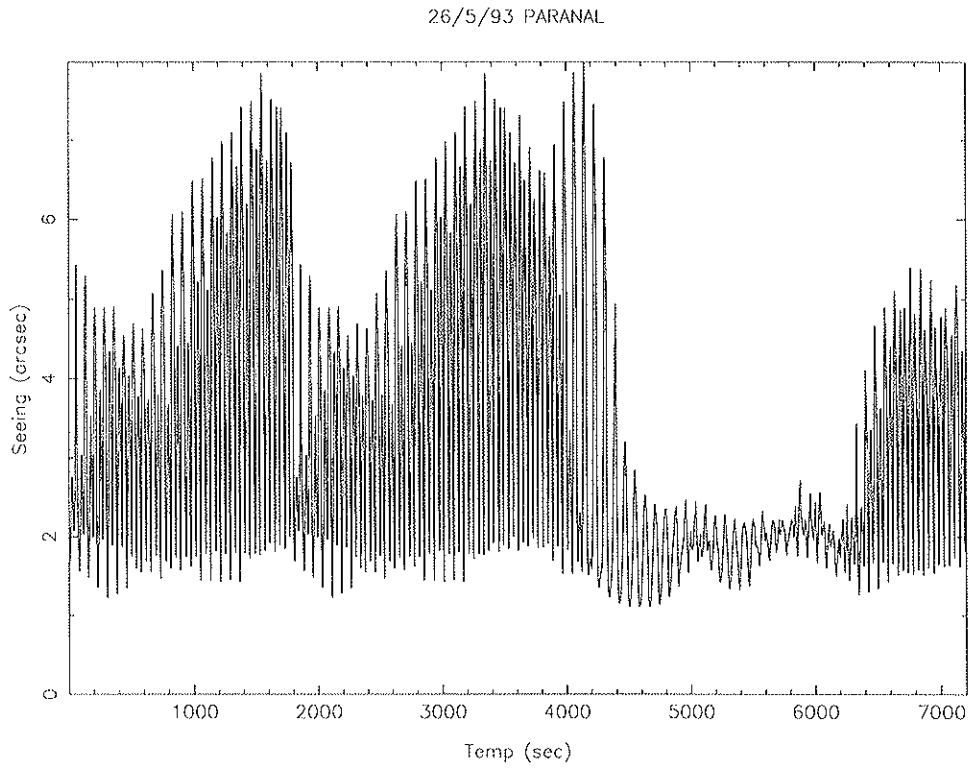


Figure 19: **26/5/93** 4 h time seeing evolution above Paranal.

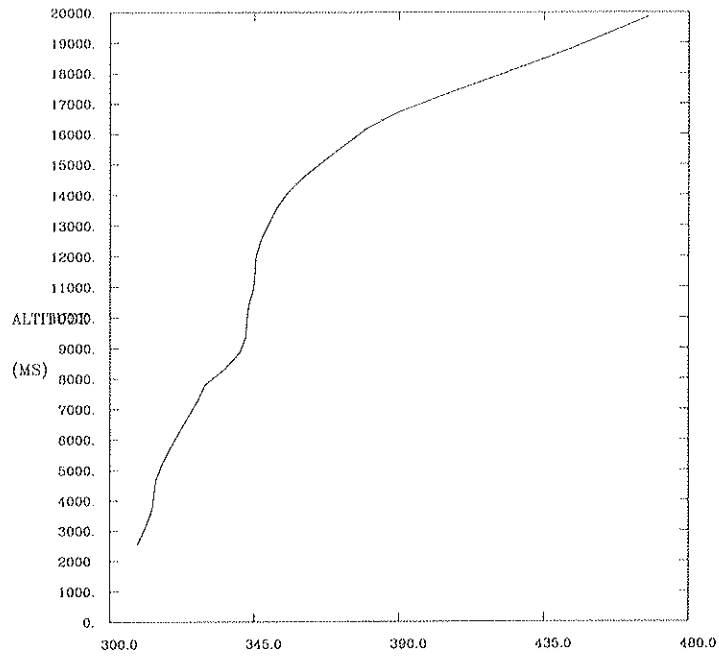


Figure 20: **26/5/93** Potential temperature vertical profile over Paranal mountain at time $t=0$ sec, that is before the model adaptation to the orography

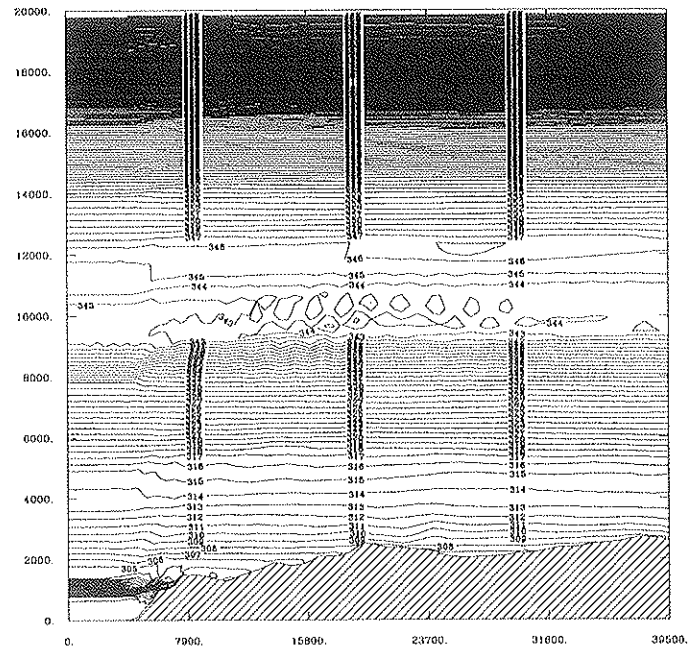


Figure 21: **26/5/93** Potential temperature east-west vertical section across Paranal mountain after 30 min simulation time

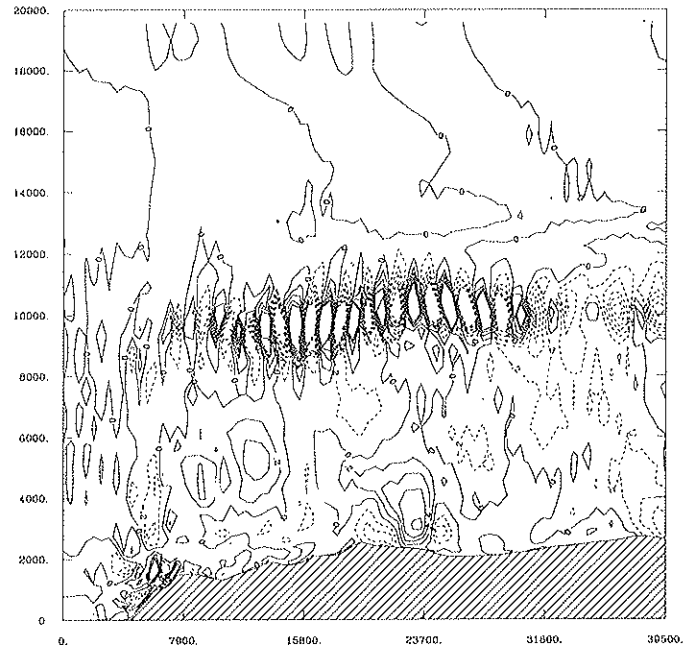


Figure 22: **26/5/93** Vertical wind fluctuations east-west vertical section across Paranal mountain after 30 min simulation time

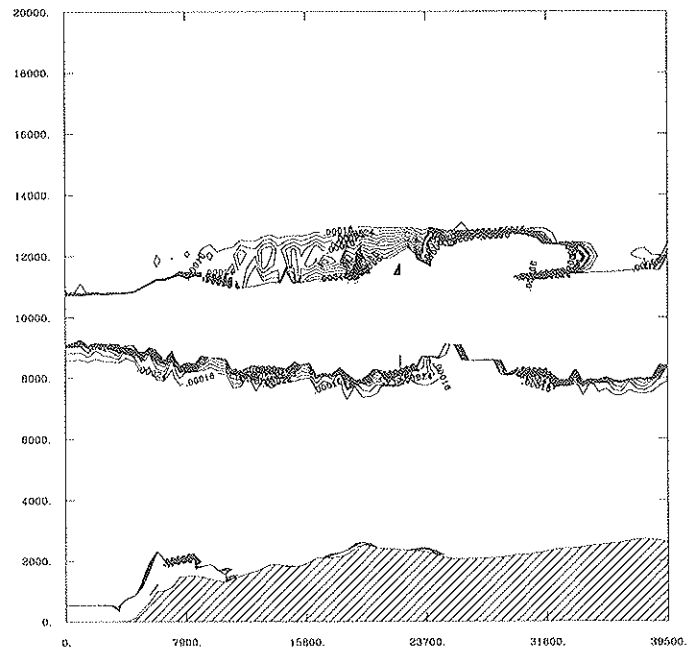


Figure 23: **26/5/93** Turbulent kinetic energy east-west vertical section across Paranal mountain after 30 min simulation time

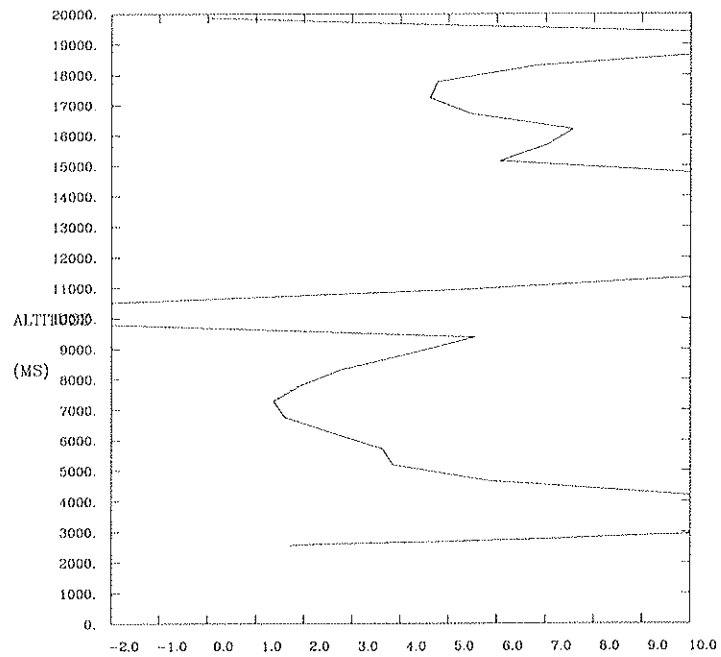


Figure 24: **26/5/93** Richardson number vertical profile over Paranal mountain after 30 min simulation time

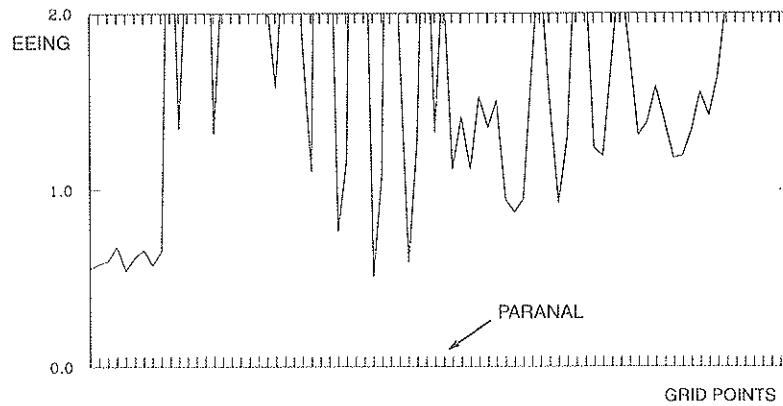


Figure 25: **26/5/93** Seeing east-west vertical section across Paranal mountain after 30 min simulation time

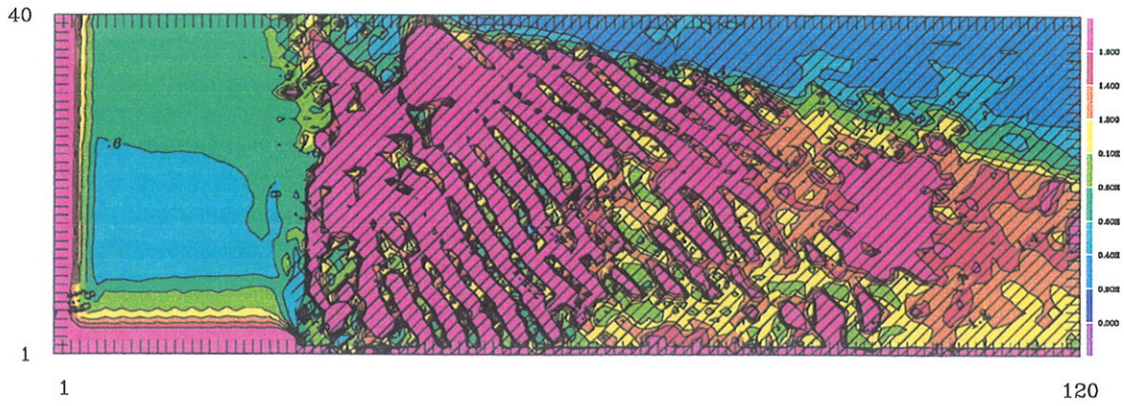


Figure 26: **26/5/93** Seeing horizontal section over Paranal mountain after 30 min simulation time

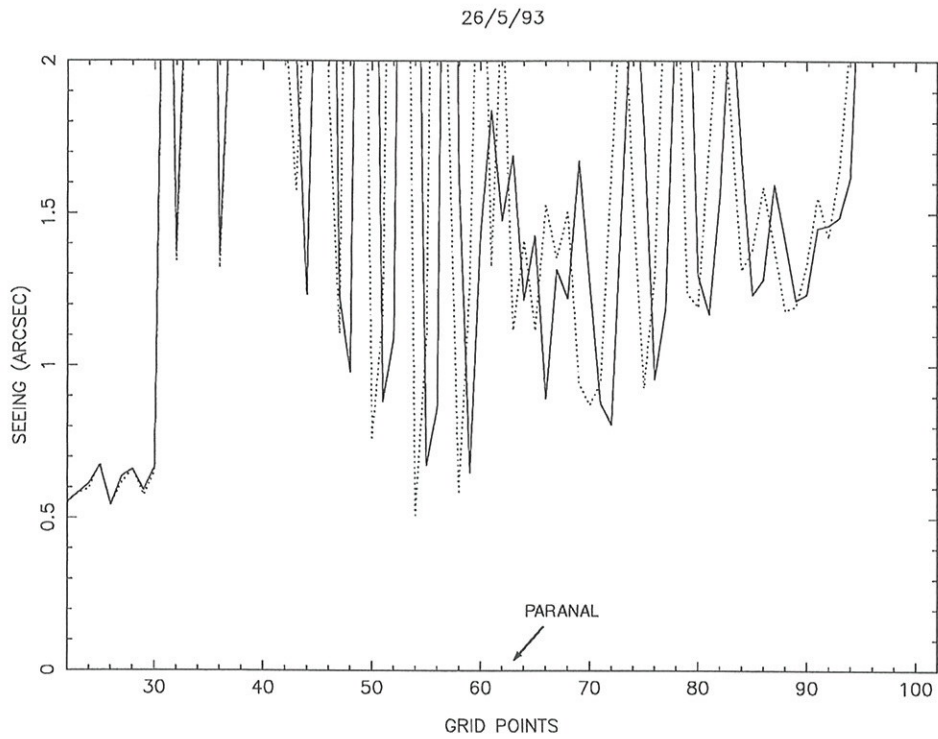


Figure 27: **26/5/93** Seeing east-west vertical section over Paranal mountain on 80 grid points centered above the Paranal and equivalent to 60 km distance. Full line: after 30 min. Dashed line: after $(30 \text{ min} + \frac{T}{4})$; $\frac{T}{4} = 77.5 \text{ sec}$; T = numeric fluctuations period

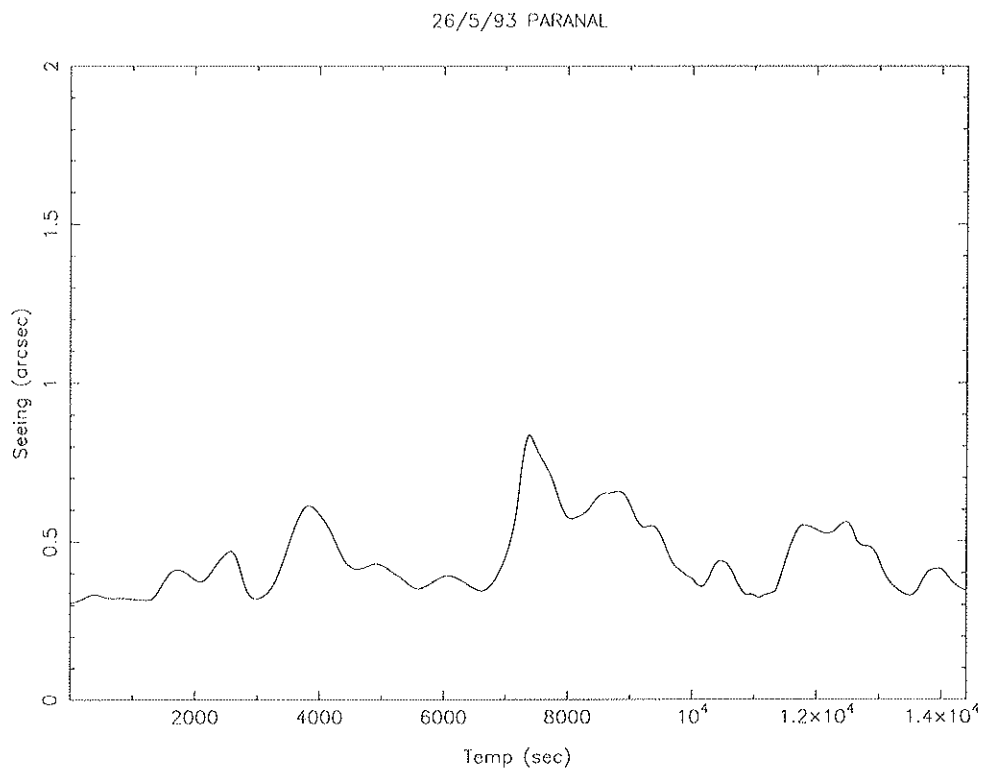


Figure 28: **26/5/93** Same as Fig.(19) but with a modified temperature profile

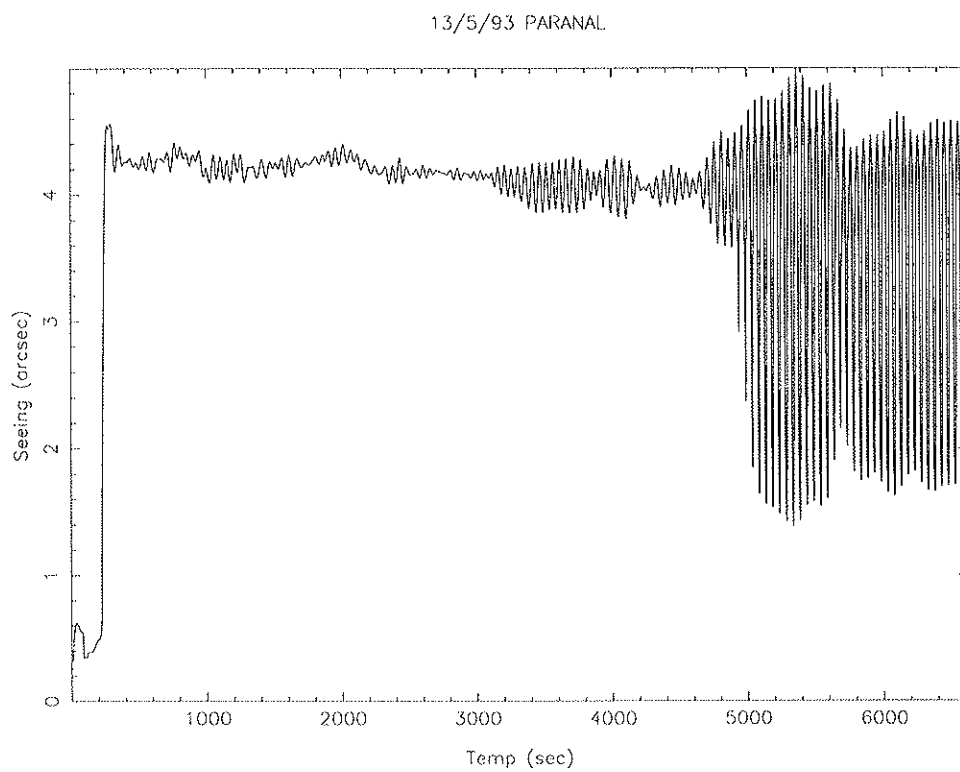


Figure 29: **13/5/93** 4 h time seeing evolution above Paranal.

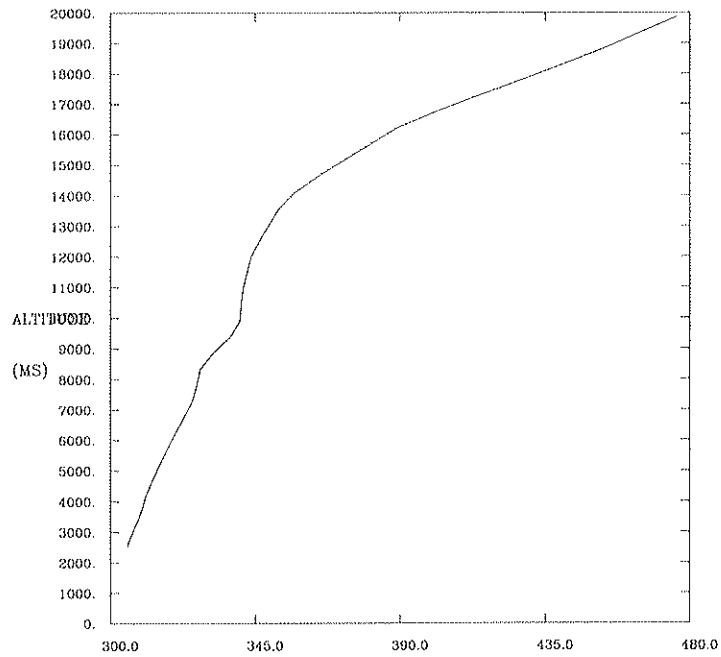


Figure 30: **13/5/93** Potential temperature vertical profile over Paranal mountain at time $t=0$ sec, that is before the model adaptation to orography

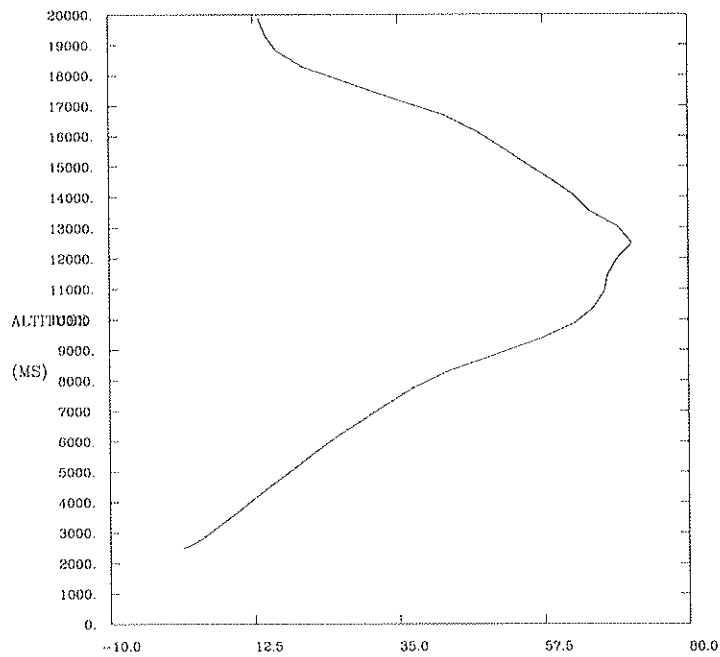


Figure 31: **13/5/93** Wind on the x axis vertical profile over Paranal mountain after 200 sec simulation time

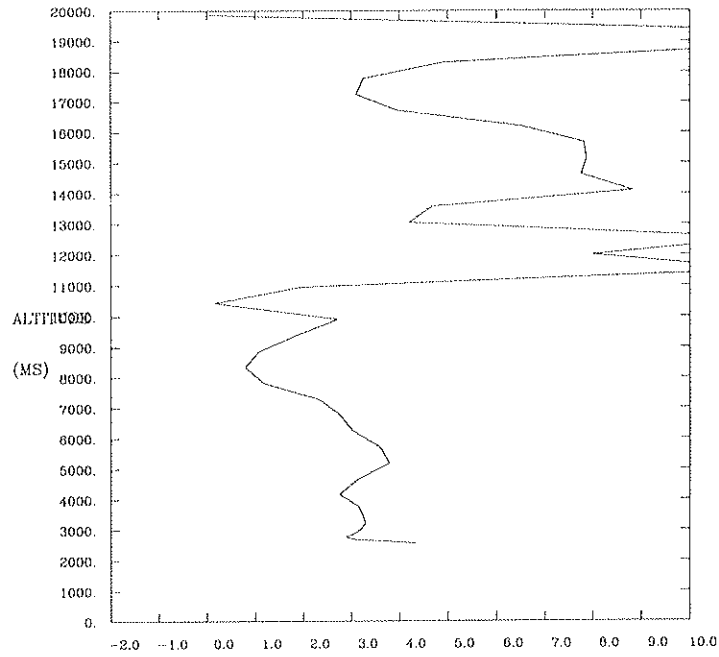


Figure 32: **13/5/93** Richardson number vertical profile above Paranal mountain after 200 sec simulation time

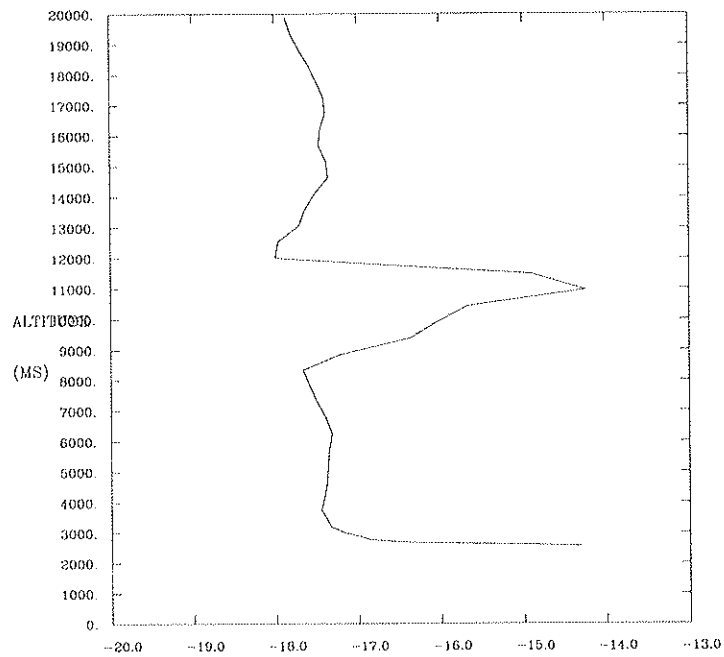


Figure 33: **13/5/93** C_N^2 vertical profile above Paranal mountain after 30 min simulation time

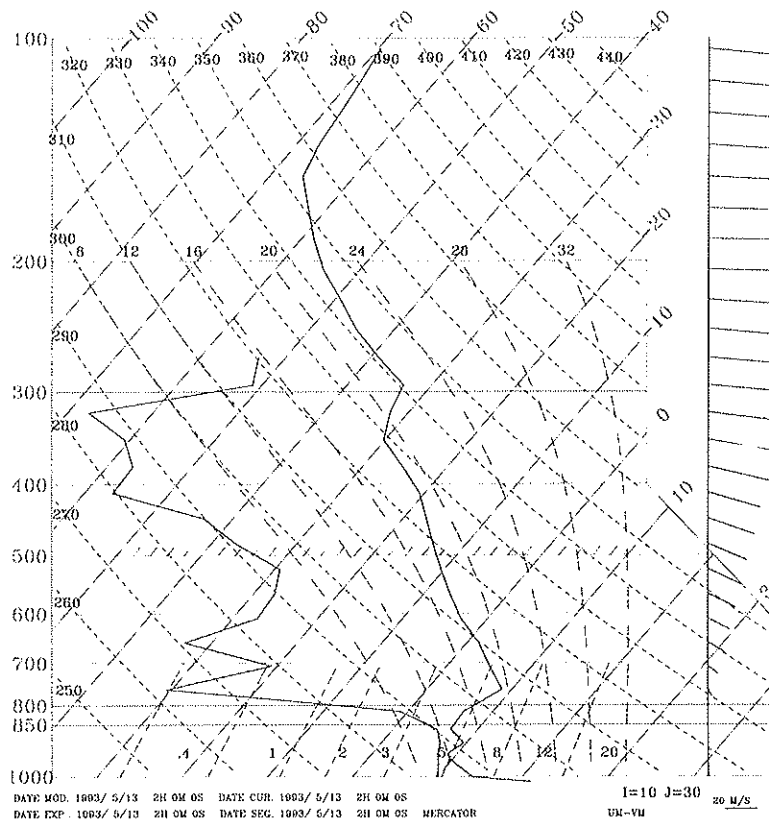


Figure 34: 13/5/93 Initialization emagram. Same as Fig.(9)

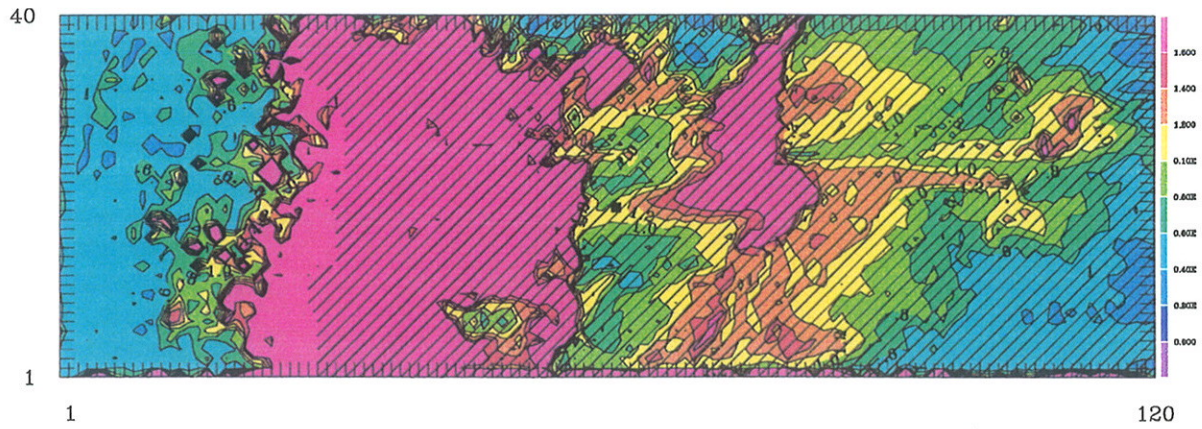


Figure 35: **14/5/93** night - Horizontal seeing map - simulation time: 4 h. Color code: seeing values between $[0 - 1.6]$ arcsec are represented with a step of 0.2 arcsec. Red regions are related to a bad seeing, blue regions to a good seeing. Bad seeing at the low edge of map is not consistent, it is related to boundary effects.

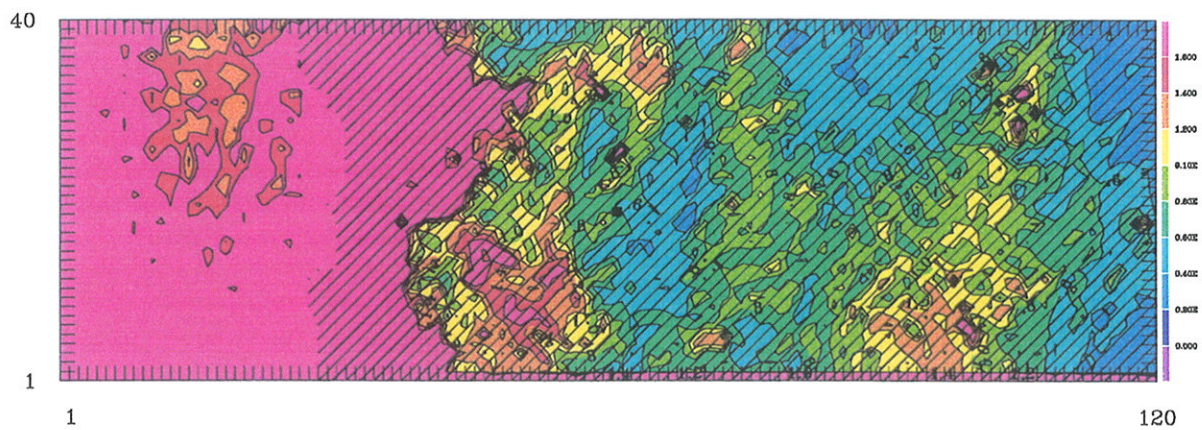


Figure 36: **15/5/93** night - Horizontal seeing map - simulation time: 4 h. Same as Fig.(35)

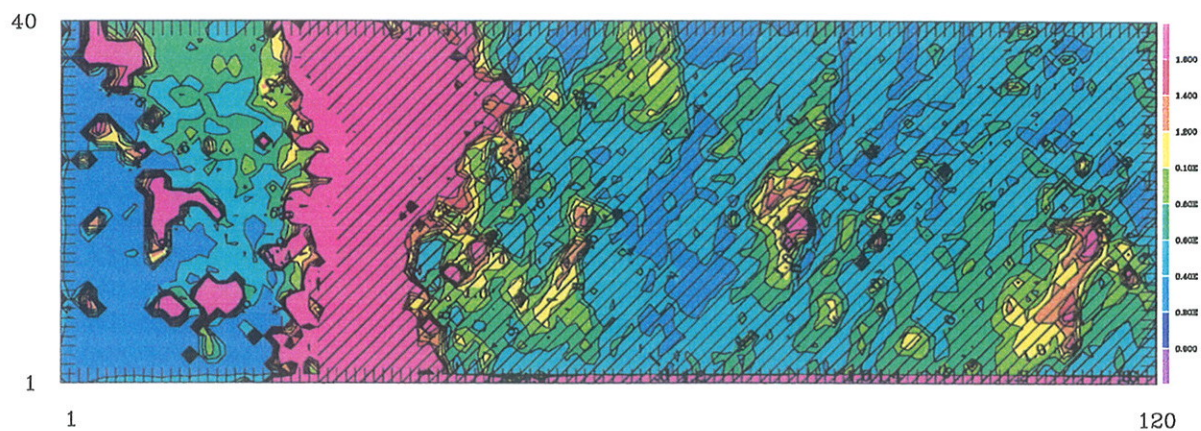


Figure 37: 16/5/93 night - Horizontal seeing map - simulation time: 4 h. Same as Fig.(35)

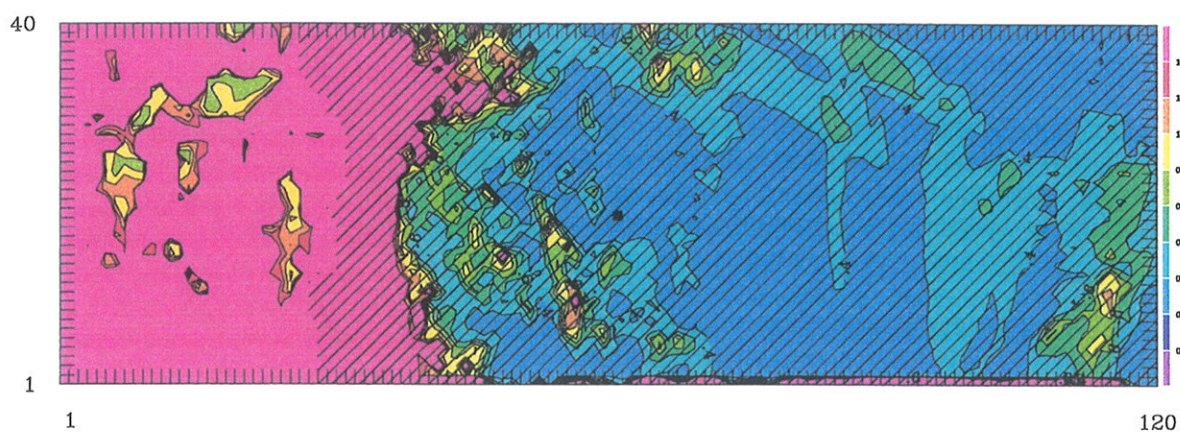


Figure 38: 17/5/93 night - Horizontal seeing map - simulation time: 4 h. Same as Fig.(35)

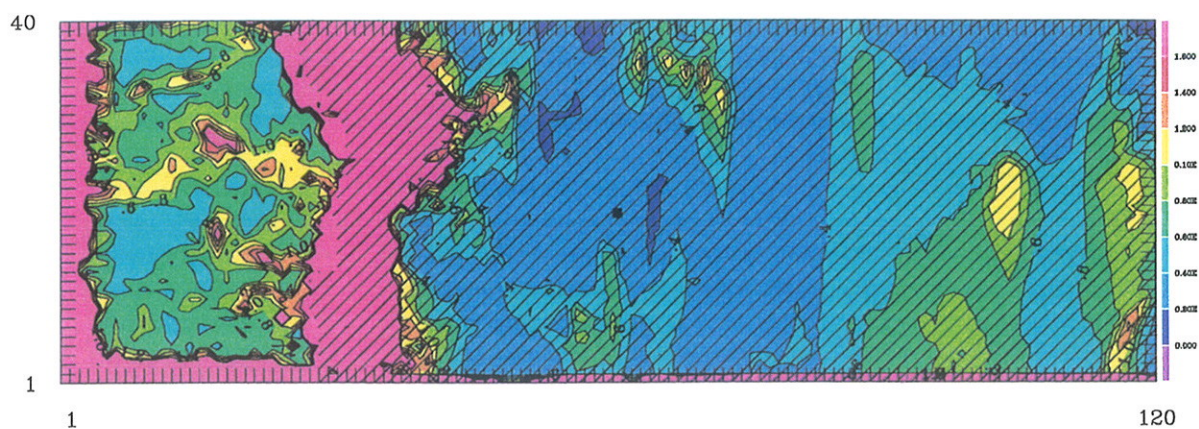


Figure 39: **18/5/93** night - Horizontal seeing map - simulation time: 4 h. Same as Fig.(35)

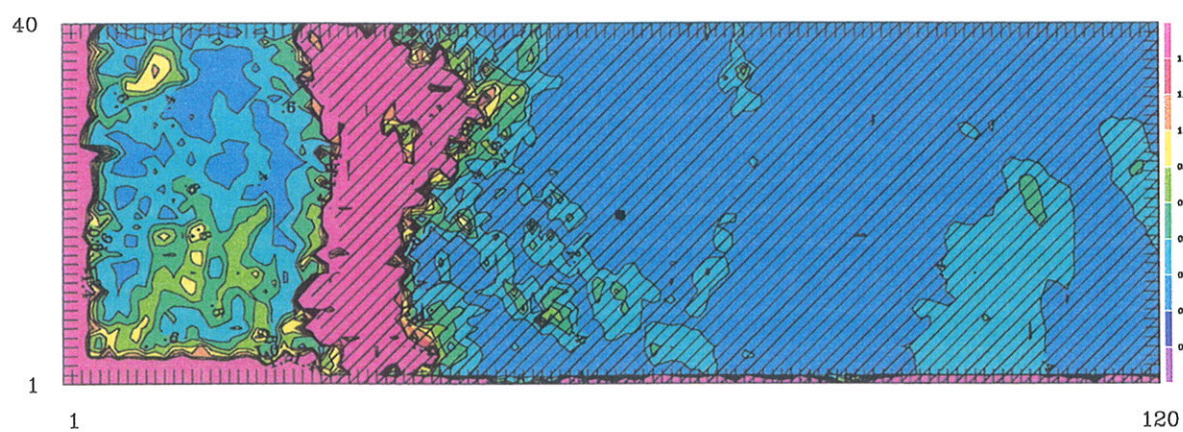


Figure 40: **19/5/93** night - Horizontal seeing map - simulation time: 4 h. Same as Fig.(35)

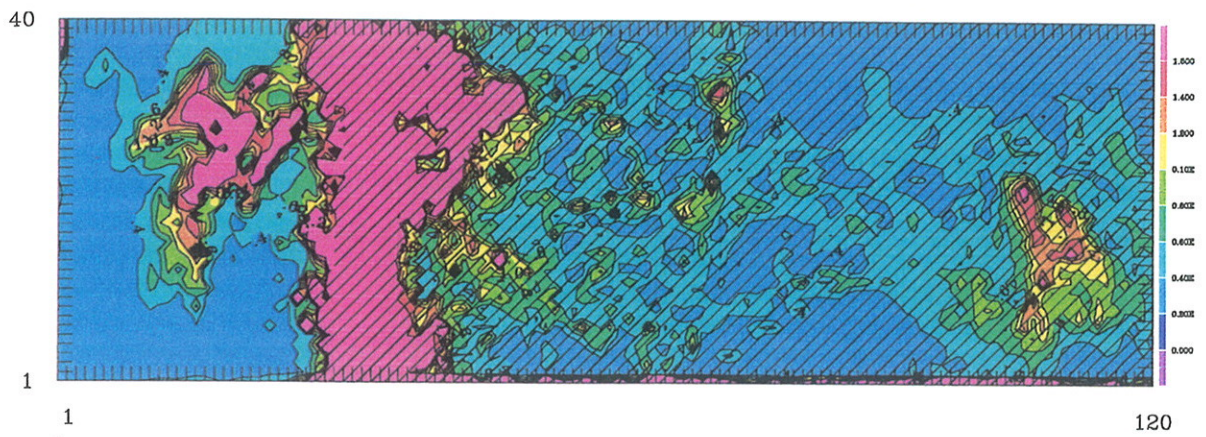


Figure 41: **23/5/93** night - Horizontal seeing map - simulation time: 4 h. Same as Fig.(35)

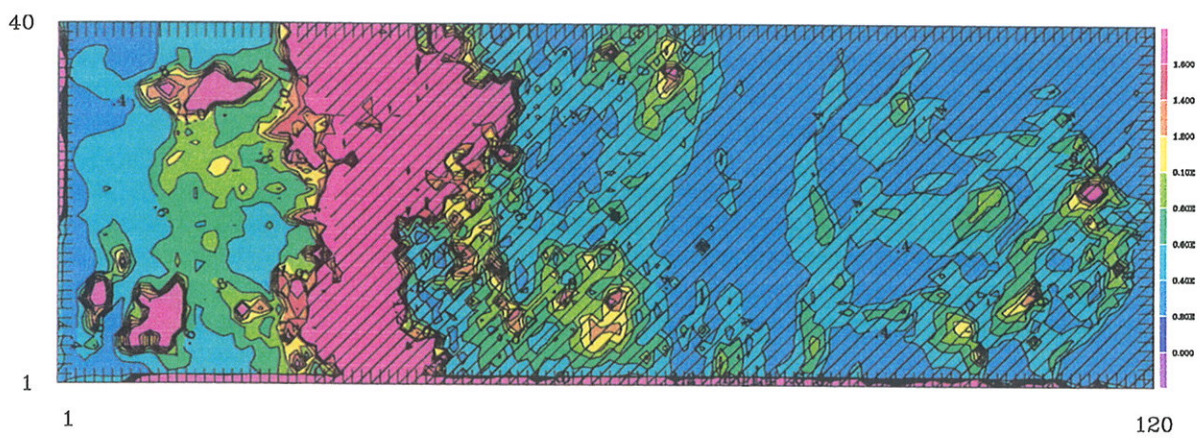


Figure 42: **25/5/93** night - Horizontal seeing map - simulation time: 4 h. Same as Fig.(35)

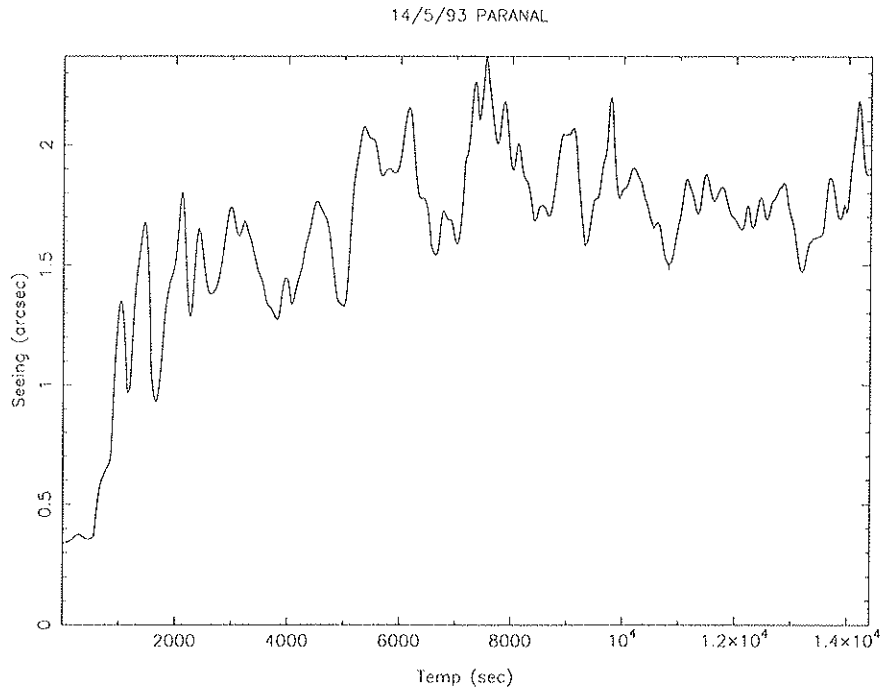


Figure 43: Time seeing evolution during the **14/5/93** night

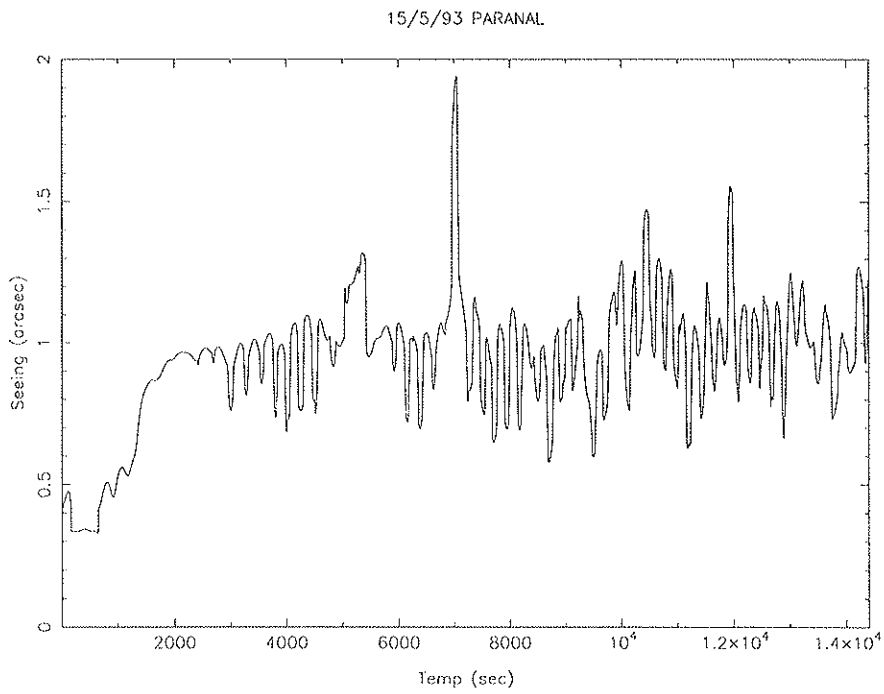


Figure 44: Time seeing evolution during the **15/5/93** night. Same as Fig.(43)

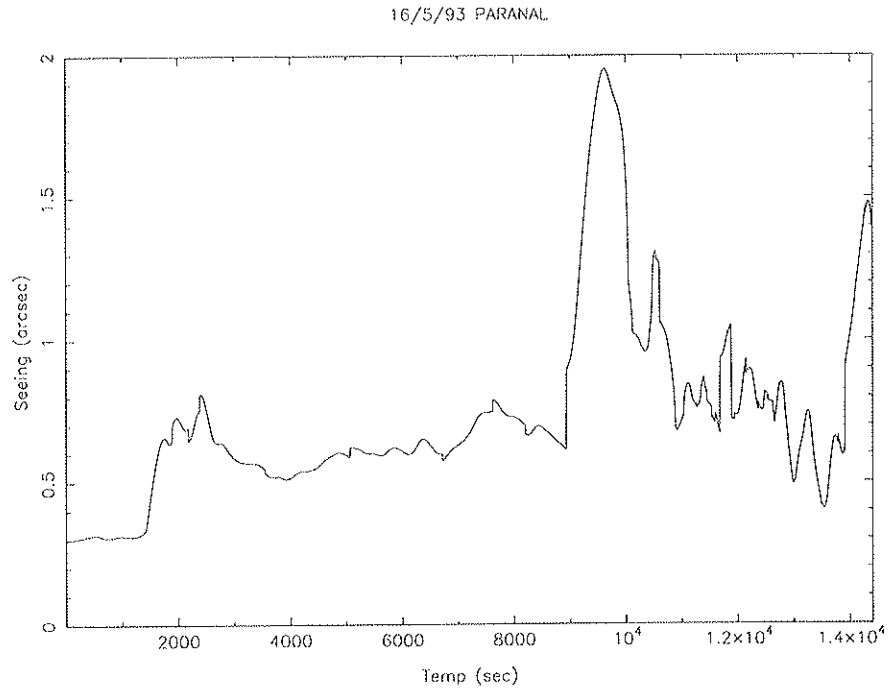


Figure 45: Time seeing evolution during the **16/5/93** night. Same as Fig.(43)

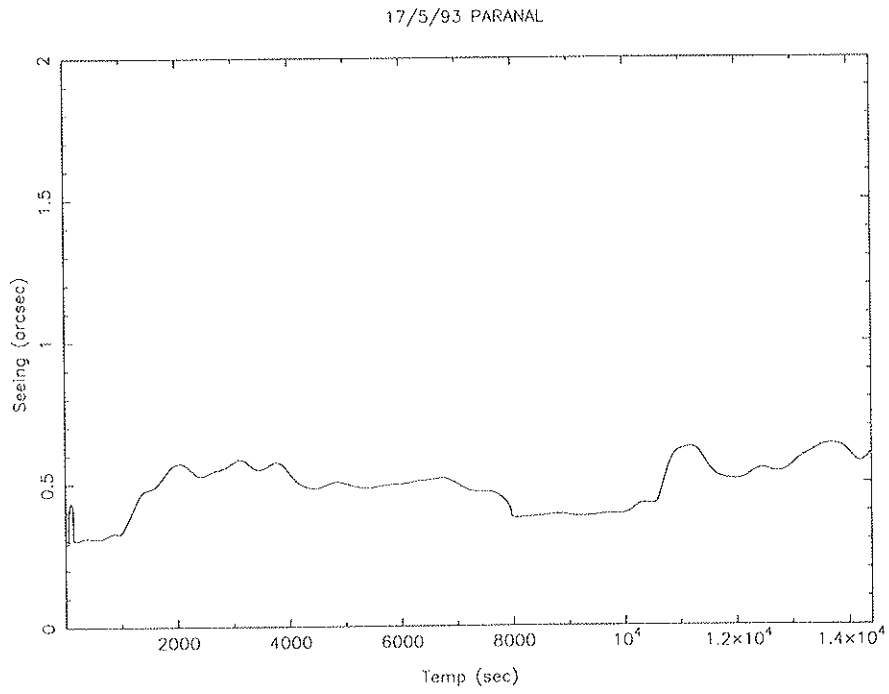


Figure 46: Time seeing evolution during the **17/5/93** night. Same as Fig.(43)

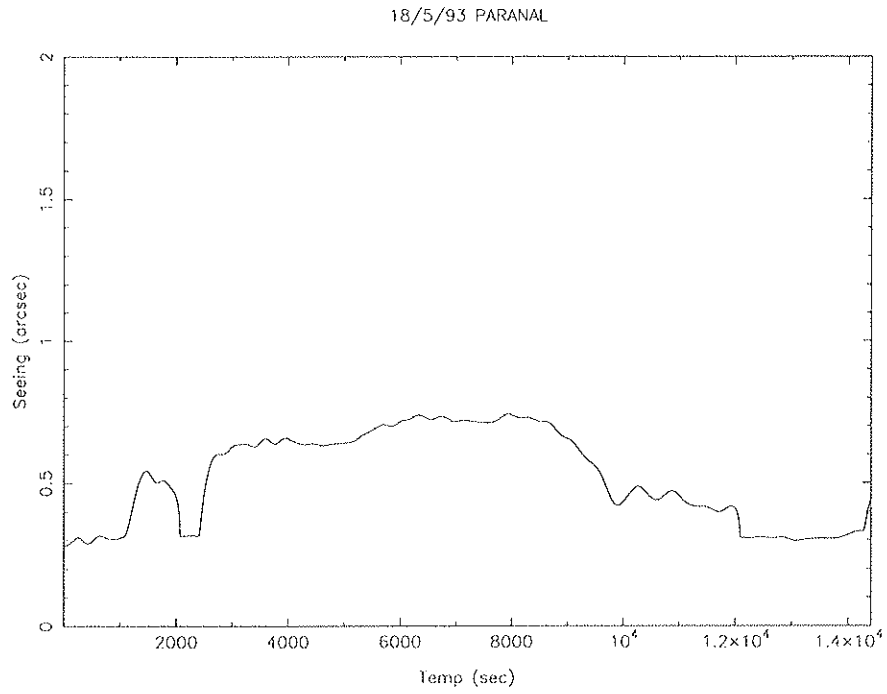


Figure 47: Time seeing evolution during the **18/5/93** night. Same as Fig.(43)

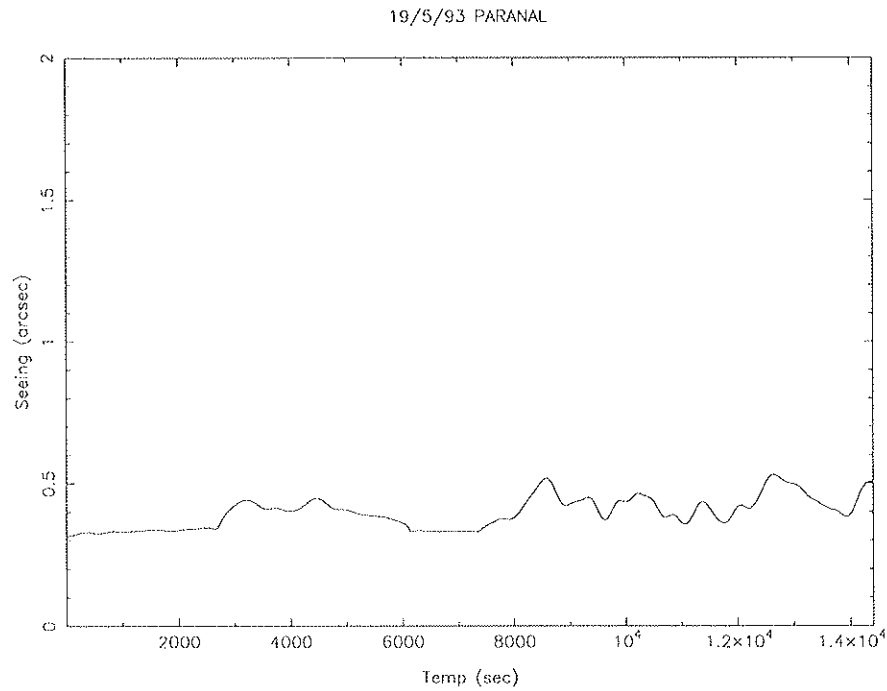


Figure 48: Time seeing evolution during the **19/5/93** night. Same as Fig.(43)

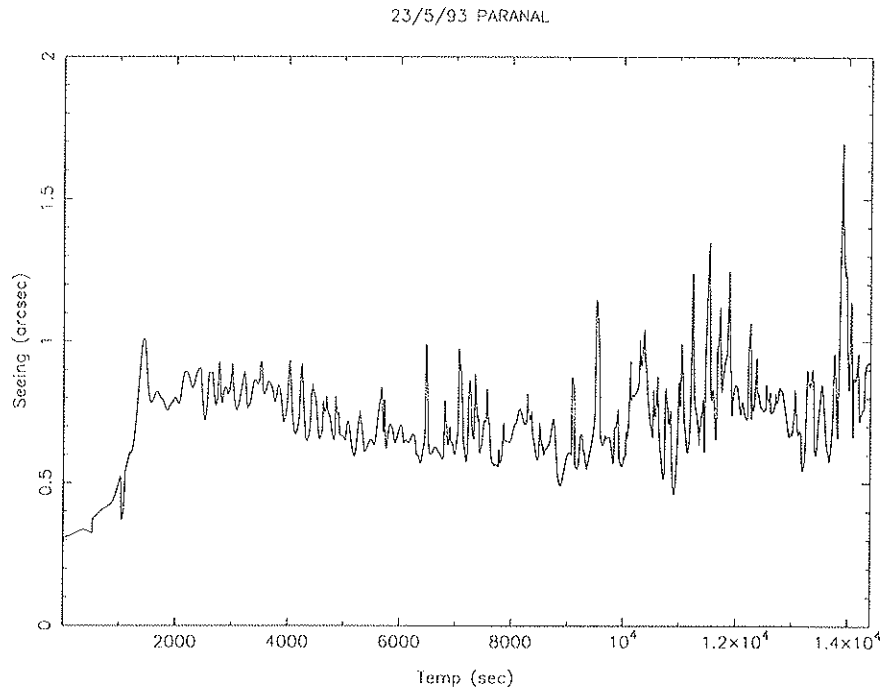


Figure 49: Time seeing evolution during the **23/5/93** night. Same as Fig.(43)

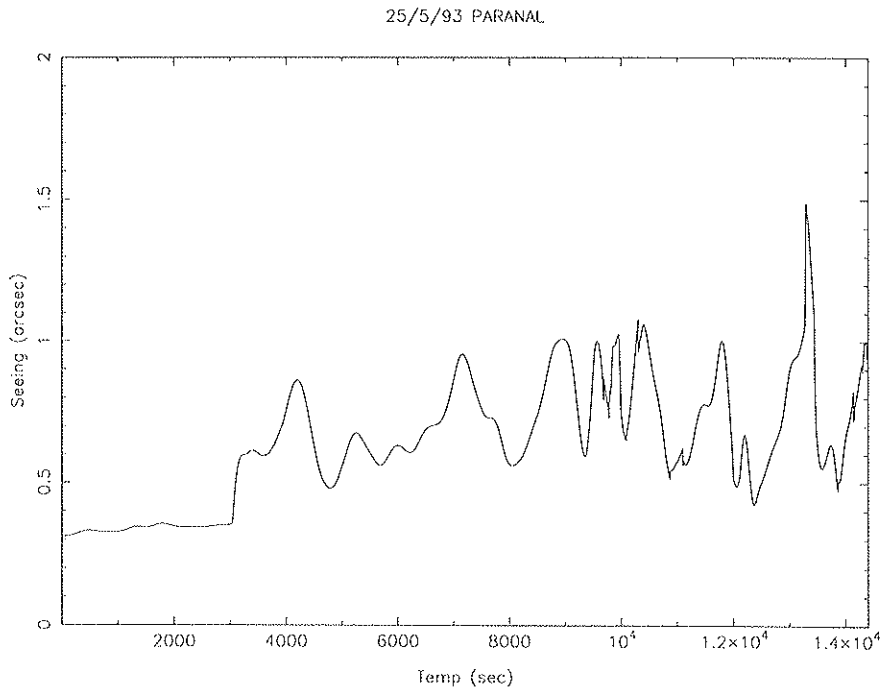


Figure 50: Time seeing evolution during the **25/5/93** night. Same as Fig.(43)

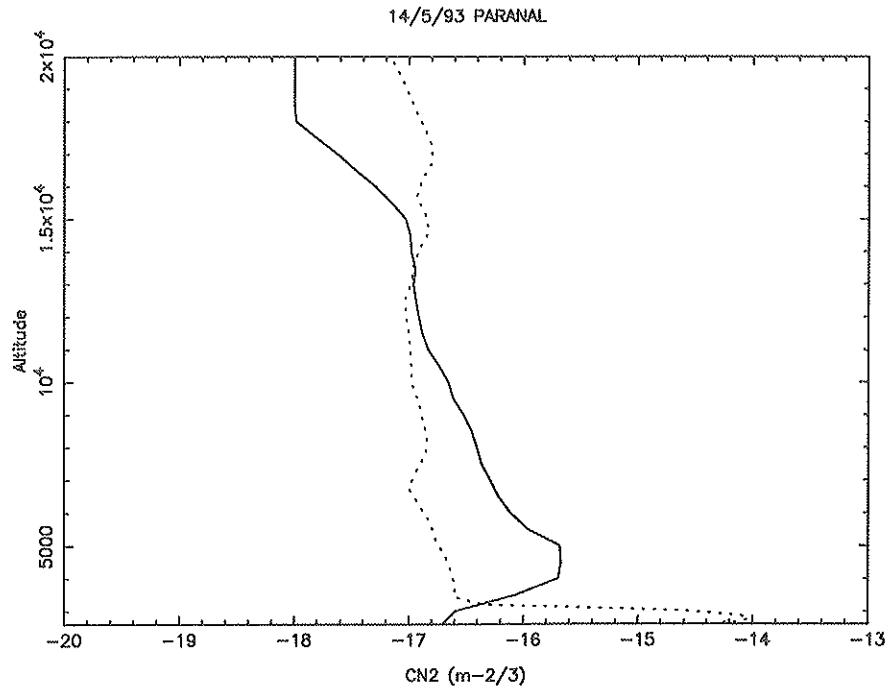


Figure 51: **14/5/93** night. C_N^2 profiles comparison between Scidar (full line) and Meso-Nh simulations after 4 h simulations (dashed line).

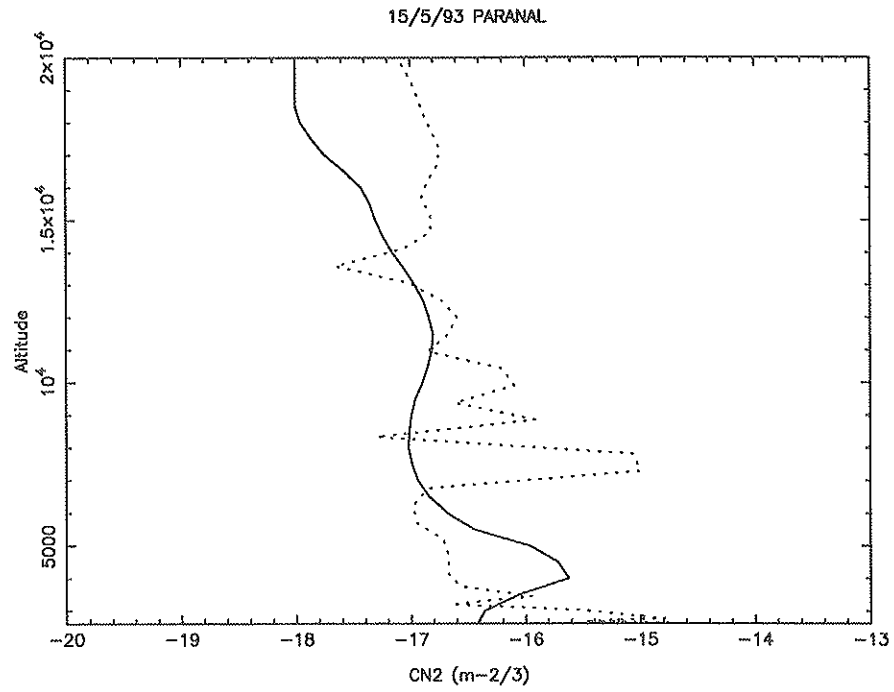


Figure 52: **15/5/93** night. Same as Fig.(51)

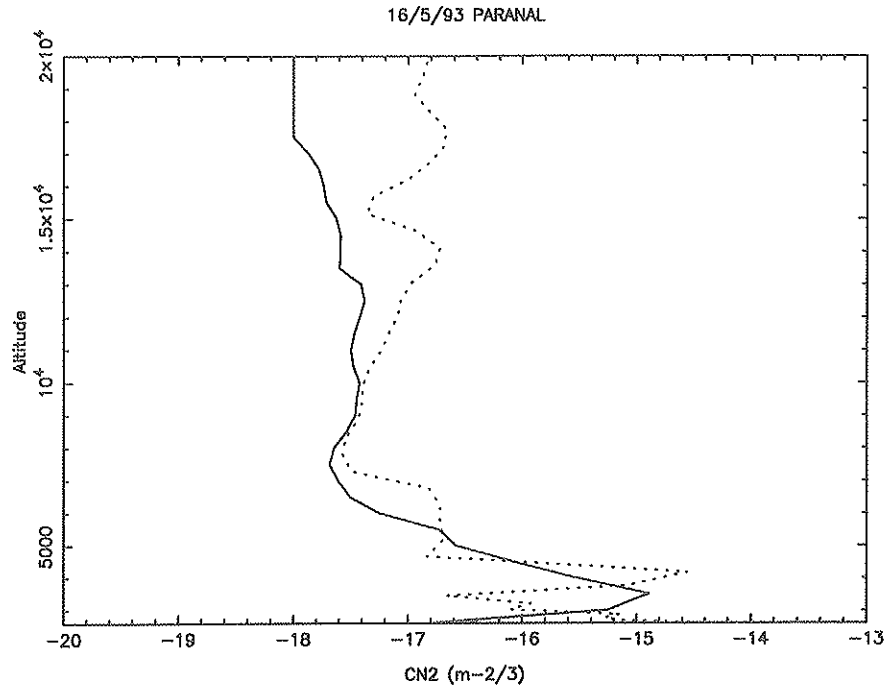


Figure 53: 16/5/93 night. Same as Fig.(51)

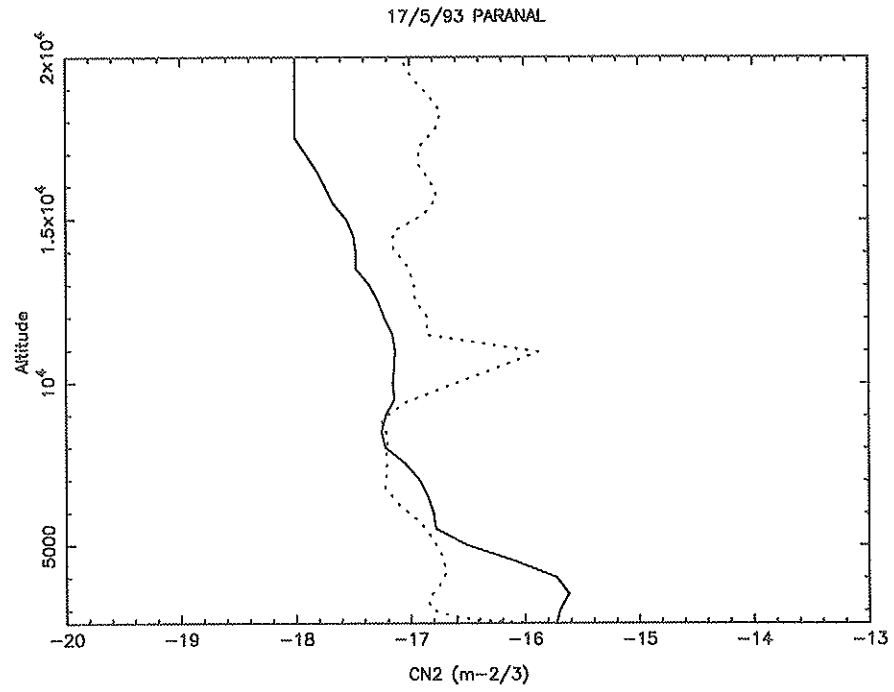


Figure 54: 17/5/93 night. Same as Fig.(51)

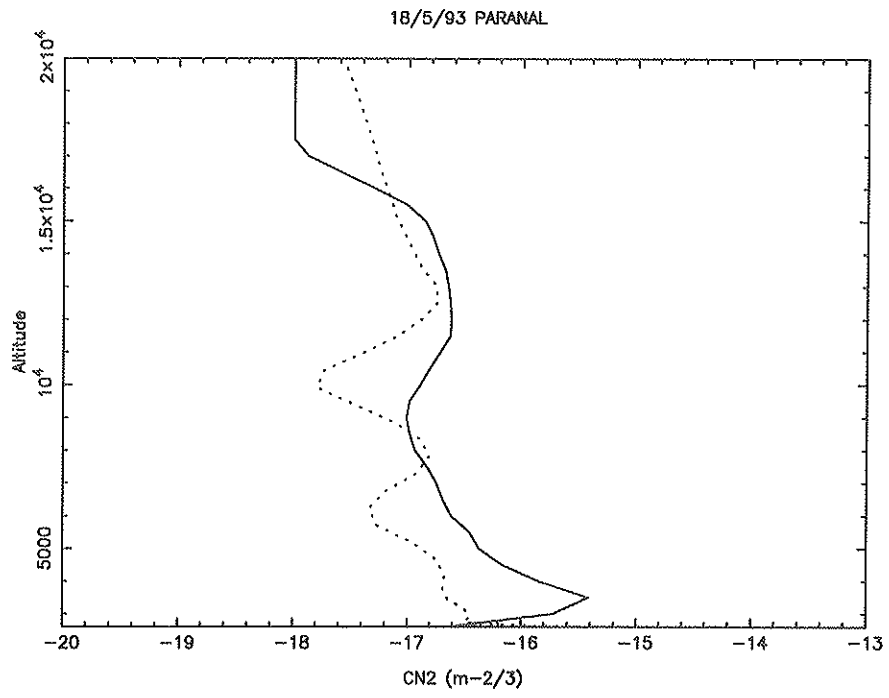


Figure 55: 18/5/93 night. Same as Fig.(51)

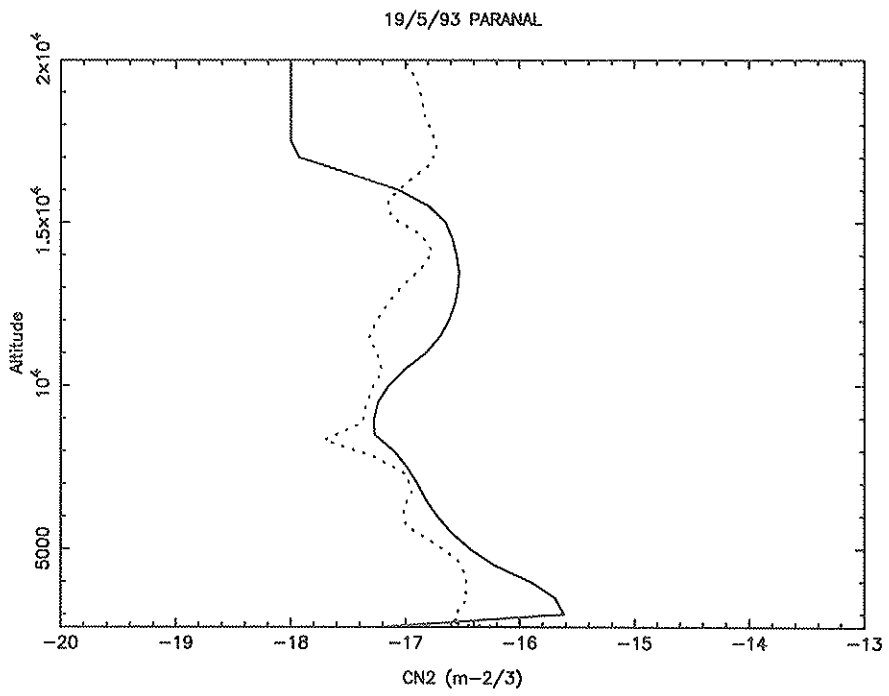


Figure 56: 19/5/93 night. Same as Fig.(51)

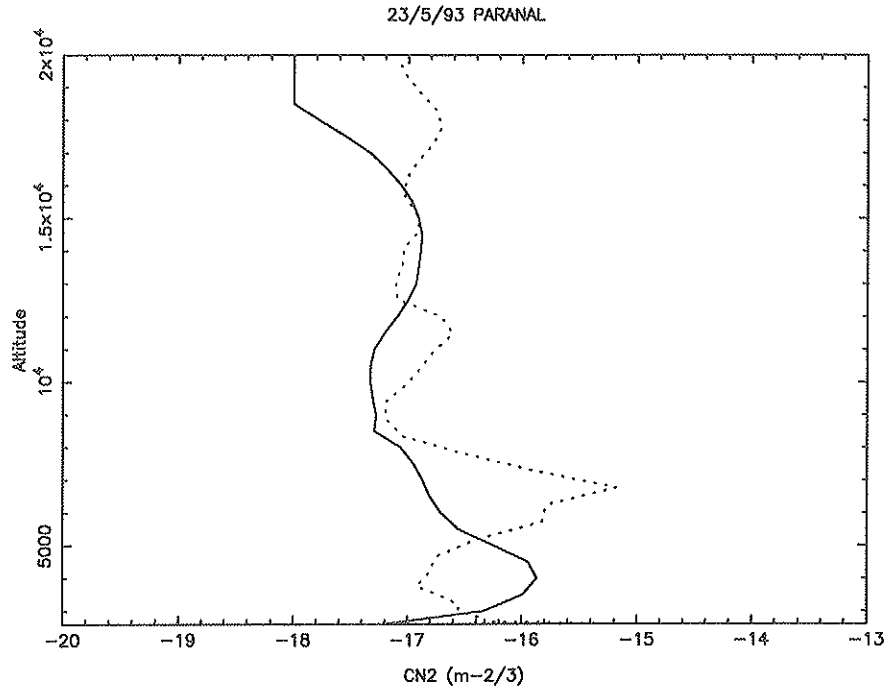


Figure 57: 23/5/93 night. Same as Fig.(51)

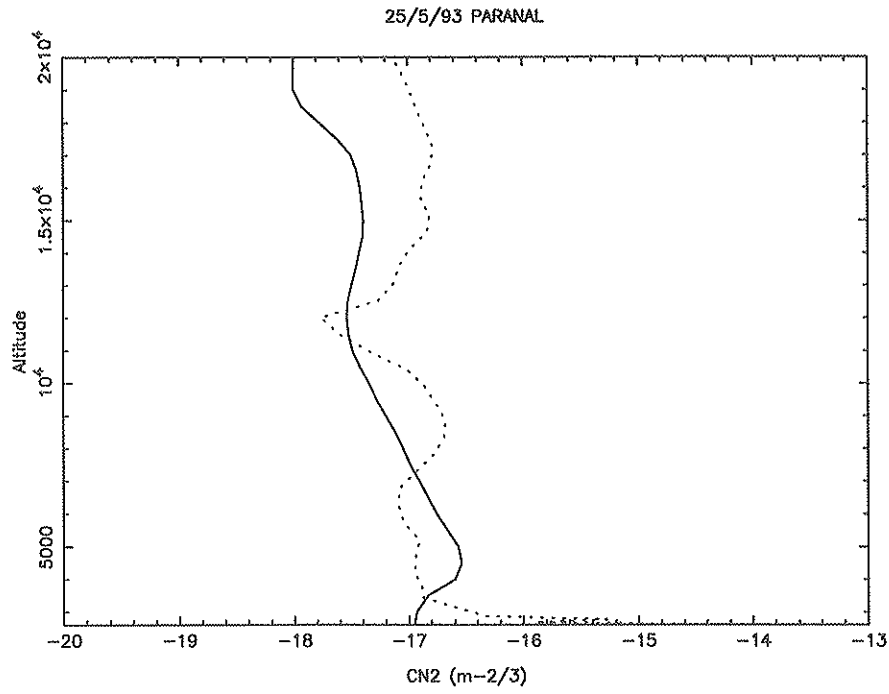


Figure 58: 25/5/93 night. Same as Fig.(51)

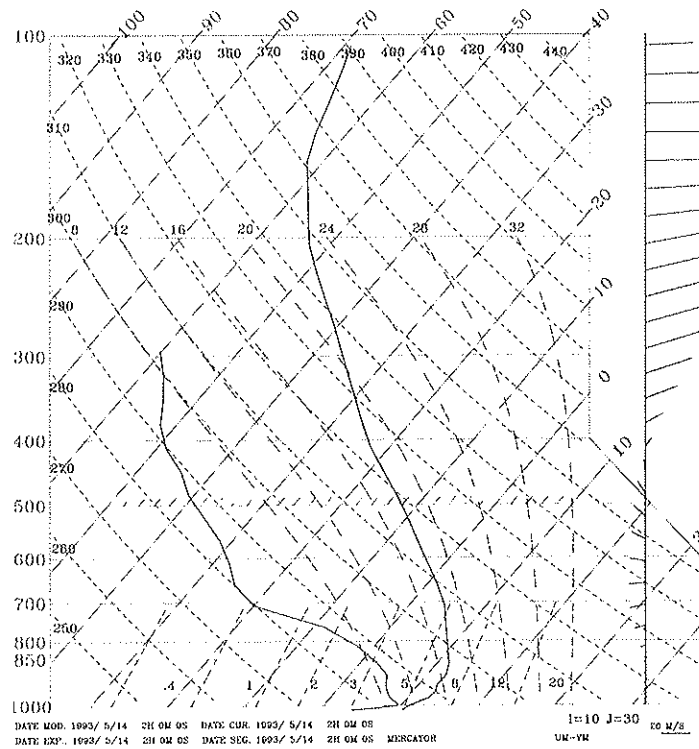


Figure 59: 14/5/93 night - Initialization emagram. Same as Fig.(9)

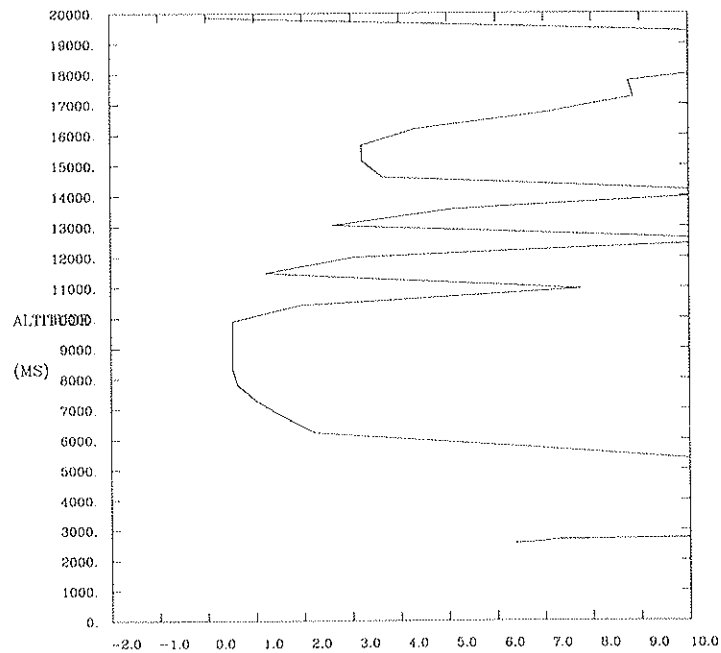


Figure 60: 14/5/93 night - Richardson number vertical profile above Paranal mountain at time $t=0$.

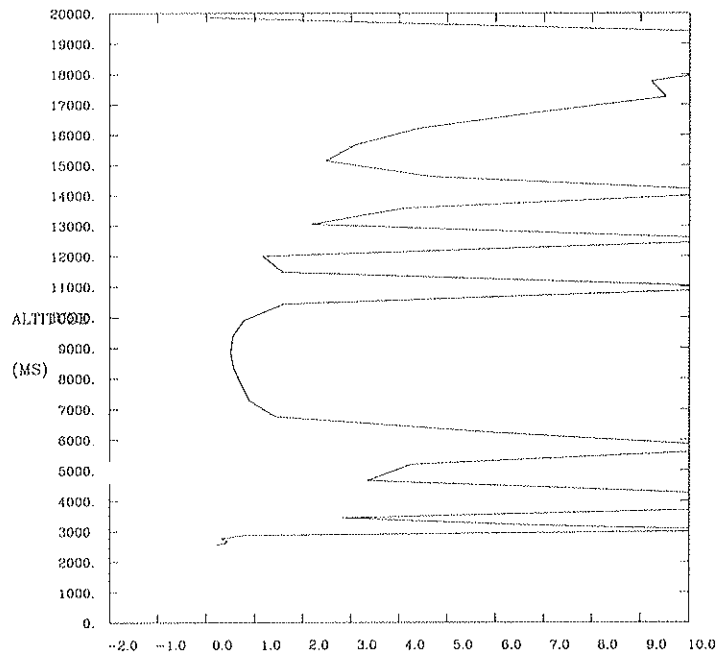


Figure 61: 14/5/93 night - Richardson number vertical profile over Paranal at time t=4 h. The model is now adapted to the orographic roughness.

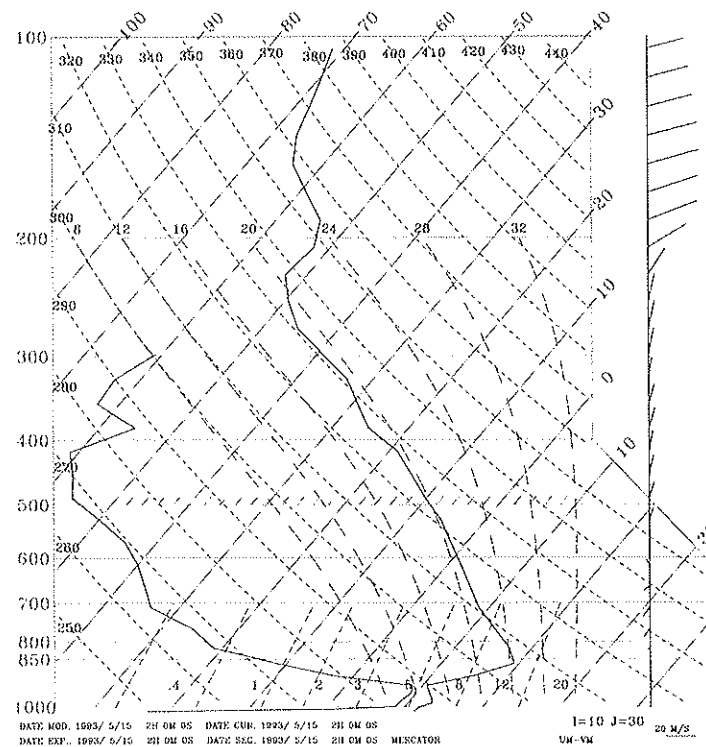


Figure 62: 15/5/93 night - Initialization emagram. Same as Fig.(9)

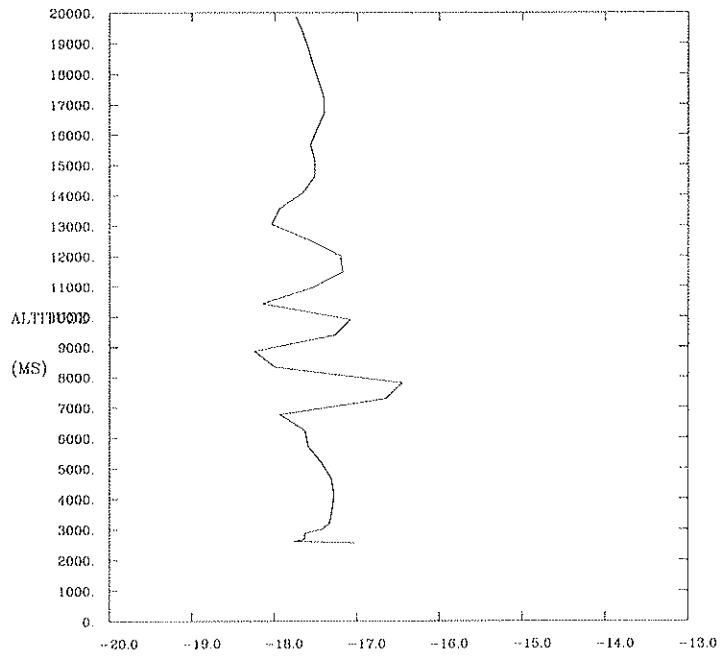


Figure 63: 15/5/93 night. C_N^2 vertical profile at the first time step

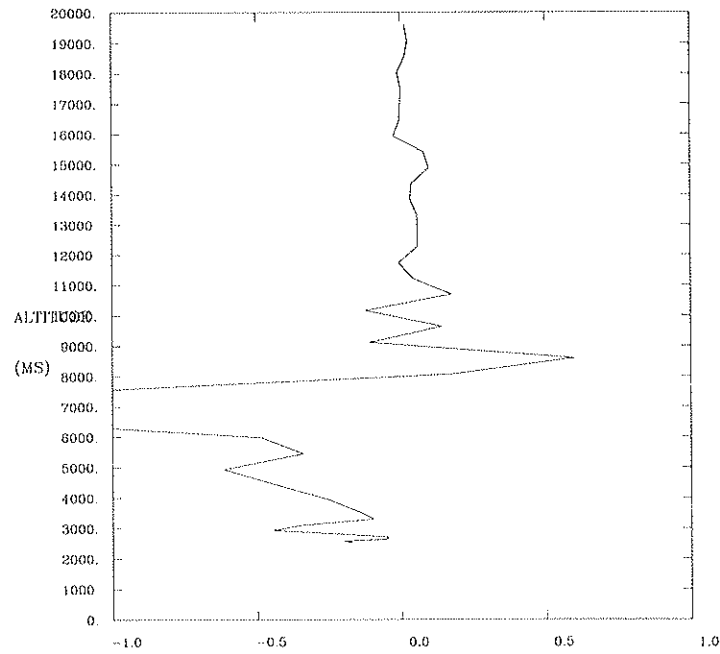


Figure 64: 23/5/93 night. Vertical wind fluctuations above Paranal mountain after 4 h simulation time

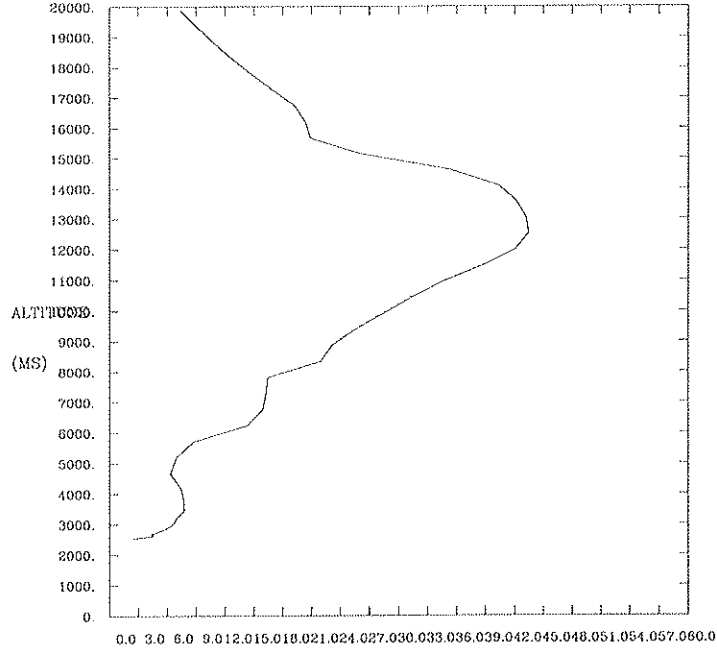


Figure 65: **23/5/93** night. Wind intensity vertical profile over Paranal mountain after 4 h simulation time

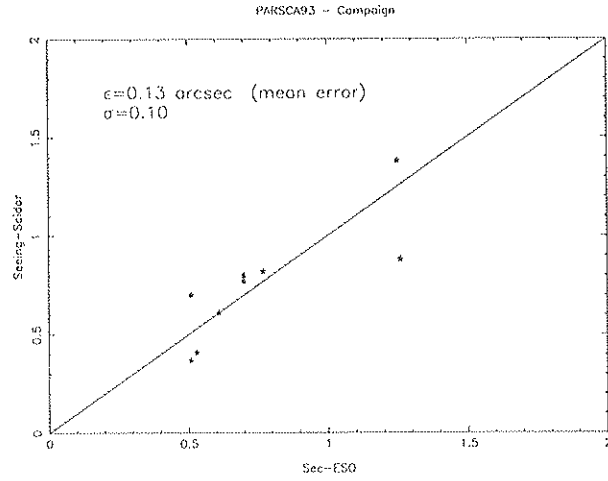


Figure 66: PARSCA93 campaign - Seeing measurements from SCIDAR and ESO-DIMM averaged on the same time range. The mean error is $\Delta\epsilon=0.13$ and the standard deviation is $\sigma=0.10$.

	$[1^h - 2^h]$	$[1^h - 3^h]$	$[2^h - 3^h]$	$[1^h - 4^h]$	$[2^h - 4^h]$	$[3^h - 4^h]$
α	1.57	1.47	1.43	1.50	1.47	1.52
a	0.92	0.94	0.96	0.94	0.94	0.93
r	0.87	0.88	0.88	0.88	0.88	0.87
r_c	0.09	0.20	0.29	0.18	0.22	0.14
σ	0.51	0.48	0.48	0.48	0.48	0.50
$P(r)$	0.83	0.63	0.49	0.66	0.60	0.74

Table 25: Summary of the statistical analysis following the **Method A**
 α = calibration coefficient, a = regression line slope, r = correlation coefficient, r_c = centered correlation coefficient, P = probability that two uncorrelated distribution x_i and y_i , belonging to the same parent distributions of the analyzed data, give a correlation coefficient larger than that observed. σ = standard deviation of the Meso-Nh distribution data with respect to the regression straight line

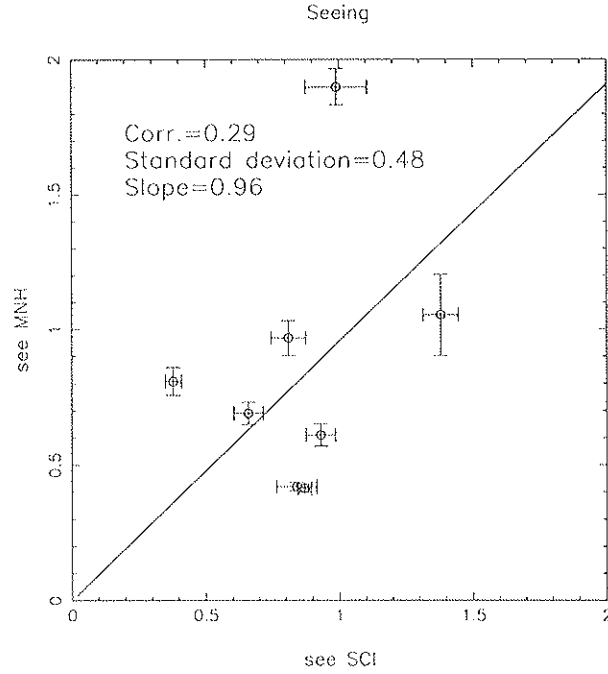


Figure 67: Statistical analysis summary for the $[2^h - 3^h]$ temporal window - **Method A** The seeing simulated is obtained by the integrations of C_N^2 profiles after calibration. In this case the calibration coefficient is $\alpha = 1.43$ (Table(25)).

$\beta = C_N^2$ correction coefficient= 4.48 - Vertical Levels [3-40]				
	$\varepsilon_{Tot}(SCI - MNH)$	$\varepsilon_{BL}(SCI - MNH)$	$\varepsilon_{FA}(SCI - MNH)$	$\varepsilon_{Tot}^*(SCI - MNH)$
a	0.97	0.73	1.19	0.96
r	0.88	0.73	0.77	0.88
r_c	0.33	0.30	0.06	0.29
σ	0.54	0.56	0.42	0.48
P(r)	0.43	0.46	0.89	0.49

Table 26: Statistical analysis summary following the **Method B (I)**. The first 100 m (first two levels) are rejected. β = calibration coefficient. For a, r, r_c , σ and P same as Table(25). ε_{Tot}^* is the $[2^h - 3^h]$ column of Table(25)) reported here.

$\beta = C_N^2$ correction coefficient= 2.86 - Vertical Levels [1-40]				
	$\varepsilon_{Tot}(SCI - MNH)$	$\varepsilon_{BL}(SCI - MNH)$	$\varepsilon_{FA}(SCI - MNH)$	$\varepsilon_{Tot}^*(SCI - MNH)$
a	0.94	0.83	0.91	0.96
r	0.88	0.79	0.77	0.88
r_c	0.20	0.13	0.06	0.29
σ	0.50	0.52	0.32	0.48
P(r)	0.63	0.76	0.89	0.49

Table 27: Statistical analysis summary following the **Method B (II)**. Same as Table(26) but with all the 40 vertical levels.

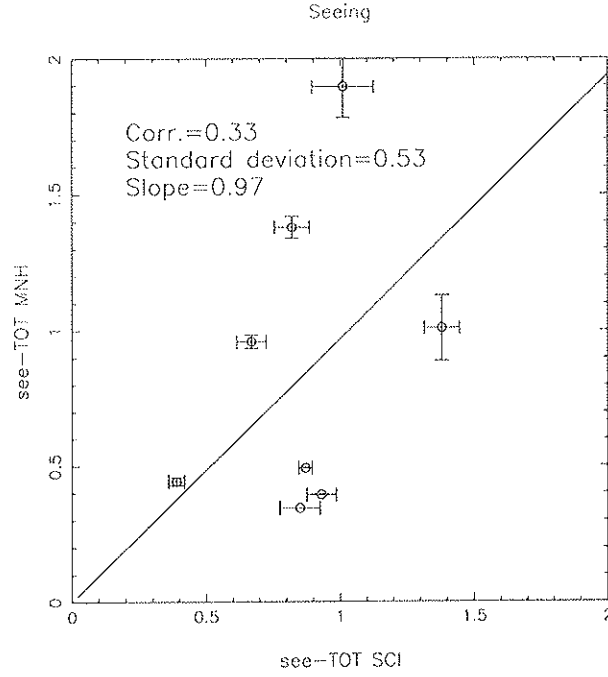


Figure 68: Statistical analysis summarize for the total seeing ε_{Tot} - **Method B (I)**. The same as Fig.(67). The calibration coefficient is $\beta = 4.48$ (Table(26))

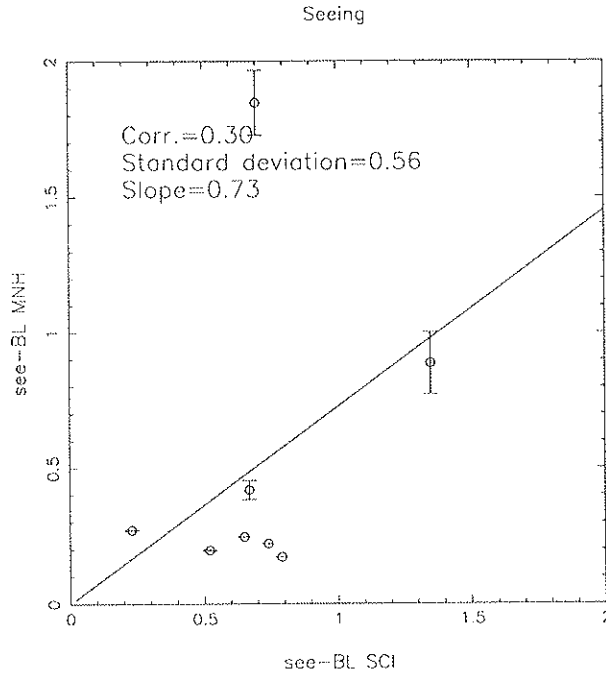


Figure 69: Statistical analysis summary for the boundary layer seeing ε_{BL} - **Method B (I)**. The same as Fig.(67). The calibration coefficient is $\beta = 4.48$ (Table(26))

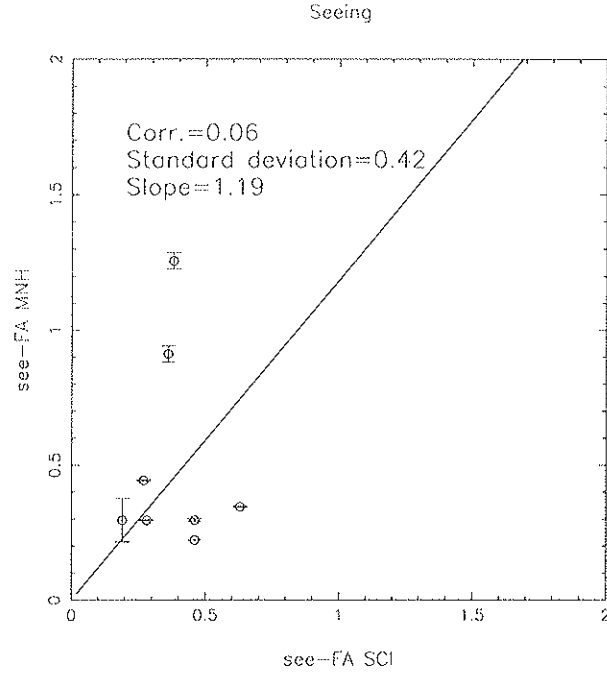


Figure 70: Statistical analysis summary for the free atmosphere seeing ε_{FA} - **Method B (I)**. The same as Fig.(67). The calibration coefficient is $\beta = 4.48$ (Table(26))

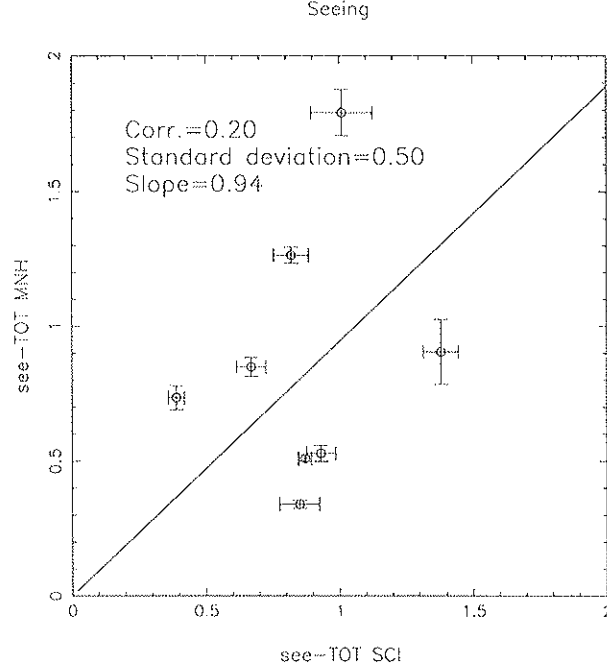


Figure 71: Statistical analysis summary for the total seeing ε_{Tot} - **Method B (II)**. The same as Fig.(67). The calibration coefficient is $\beta = 2.86$ (Table(27))

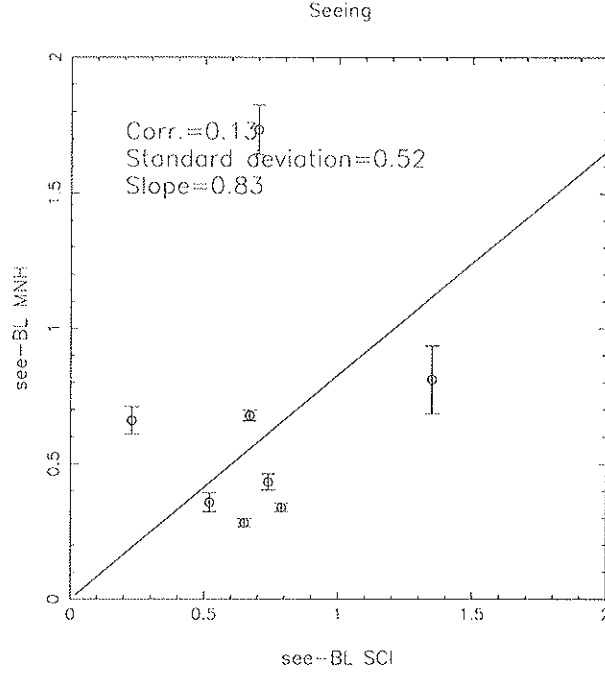


Figure 72: Statistical analysis summary for the boundary layer ε_{BL} - **Method B (II)**. The same as Fig.(67). The calibration coefficient is $\beta = 2.86$ (Table(27))

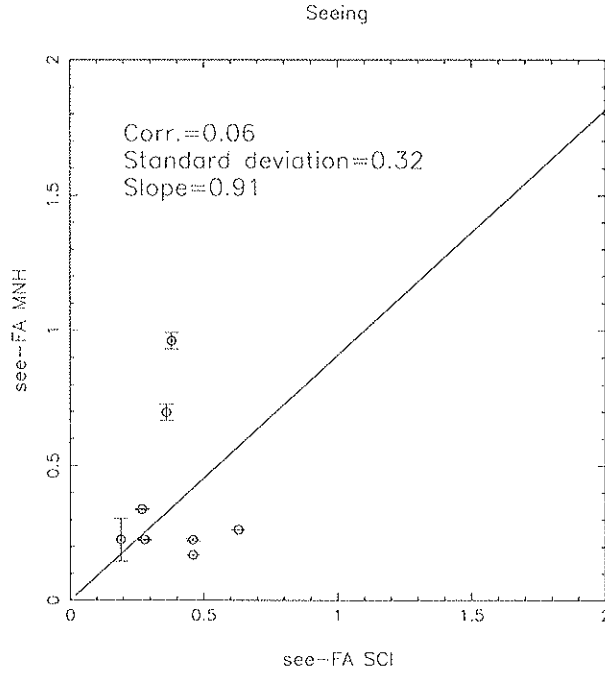


Figure 73: Statistical analysis summary for the free atmosphere seeing ε_{FA} - **Method B (II)**. The same as Fig.(67). The calibration coefficient is $\beta = 2.86$ (Table(27))

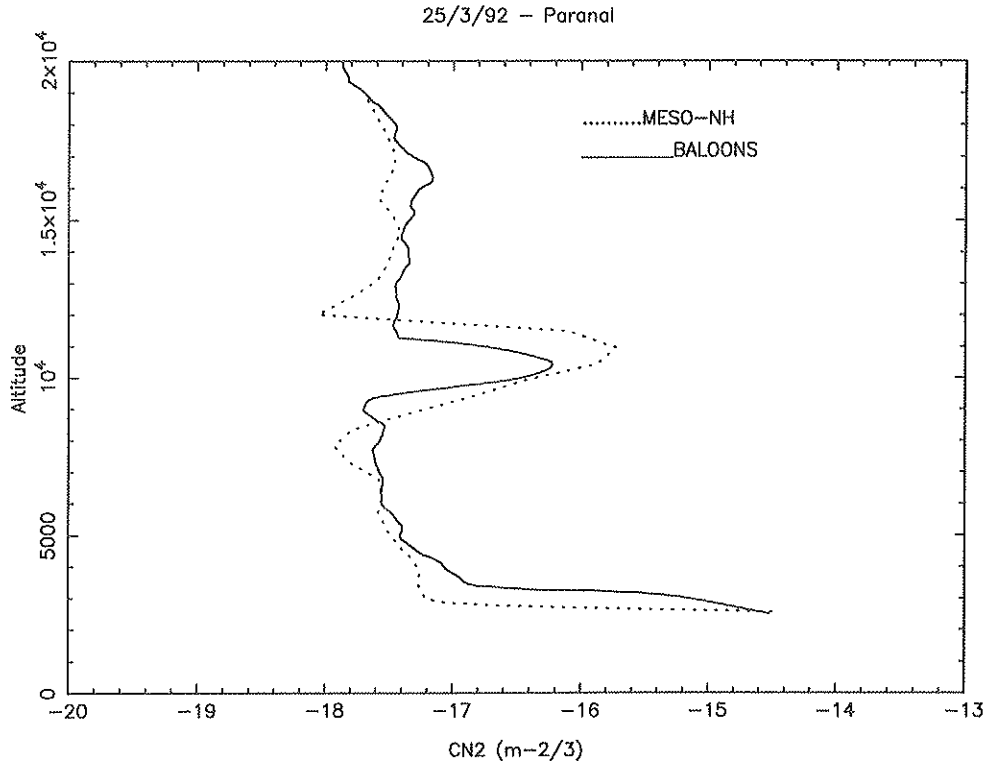


Figure 74: **25/3/92** night. C_N^2 profiles comparison from Balloons (full line) and Meso-Nh simulations after 3 h simulations (dashed line). Calibration coefficient $\beta = 1$.

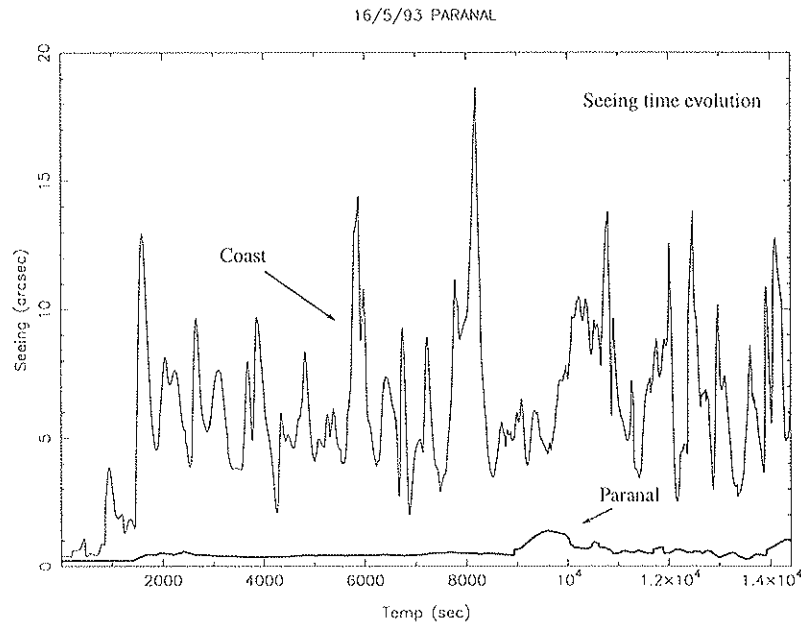


Figure 75: **16/5/93** night. Temporal seeing evolution over 4 h simulations time above the Paranal and mountain and the chilean coast.

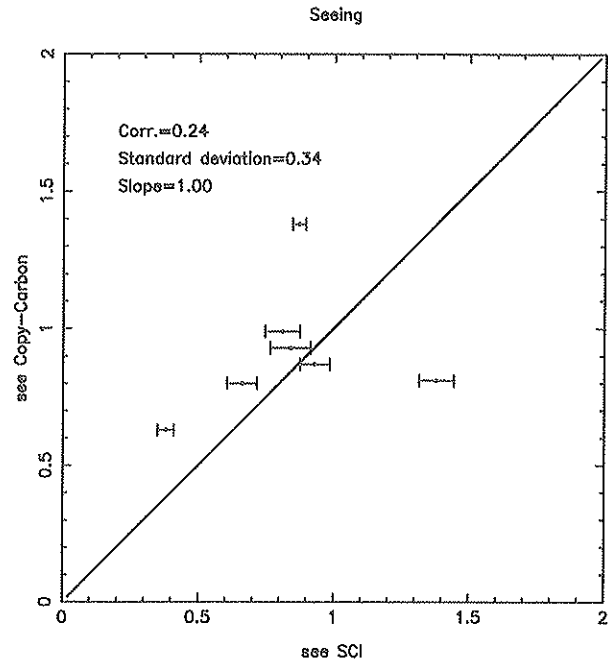


Figure 76: Statistical analysis comparison between the forecast by persistence and the numeric method.

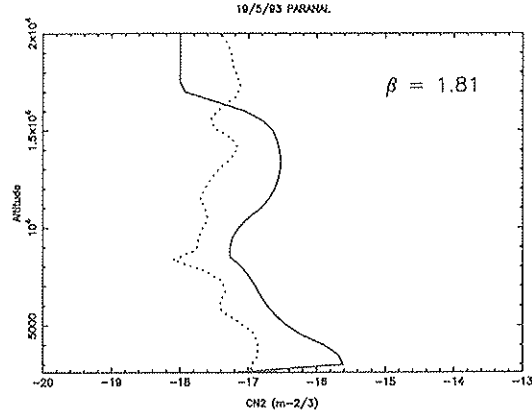


Figure 77: **16/5/93** night. C_N^2 profiles obtained by the Scidar measurements (full line) and Meso-Nh simulations (dashed line) with different calibration coefficients. The calibration coefficient is $\beta = 1.81$

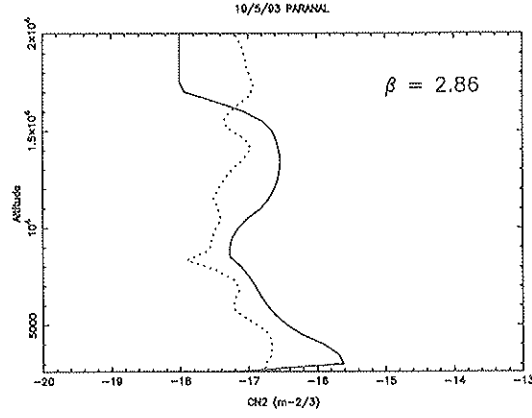


Figure 78: The same as Fig.(77) but $\beta = 2.86$

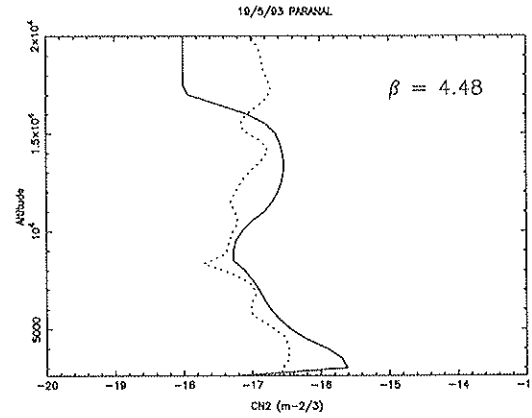


Figure 79: The same as Fig.(77) but $\beta = 4.48$

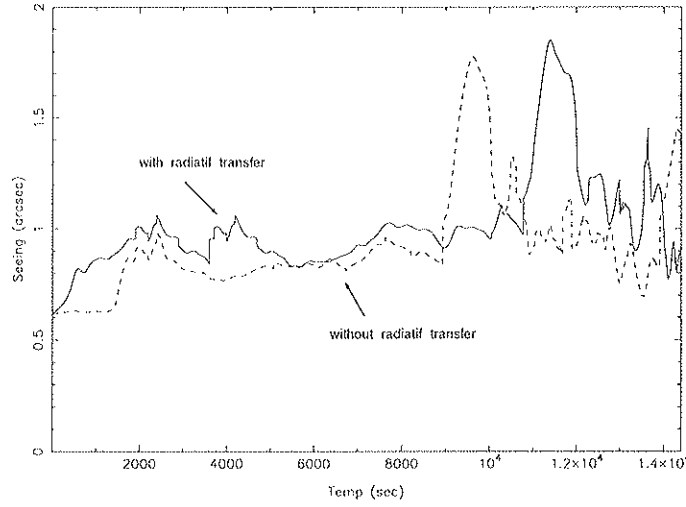


Figure 80: **16/5/93** Radiatif transfer simulation.

Time simulated seeing evolution over 4 h. **Full line**: the seeing obtained using the radiative schema. **Dashed line**: the same as Fig.(17). It is evident as the radiatif transfer, for the nightly stable condition it is not negligible.

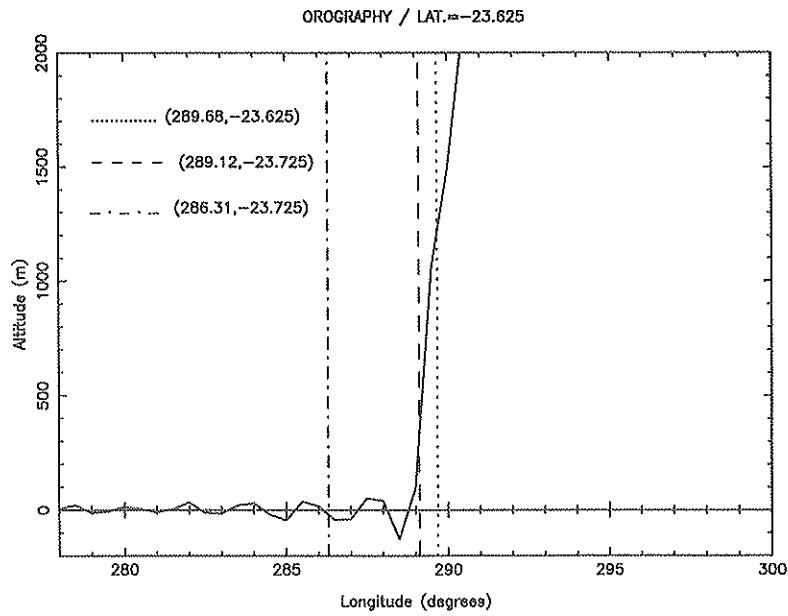


Figure 81: Vertical east-west section of earth orography. Latitude = -23.625.

Point line: longitude of the grid point (ESO1) where the ECMWF analysis studied during this feasibility study are extracted. **Dashed lines**: longitude of grid points (ESO2, ESO3) located far over the sea.

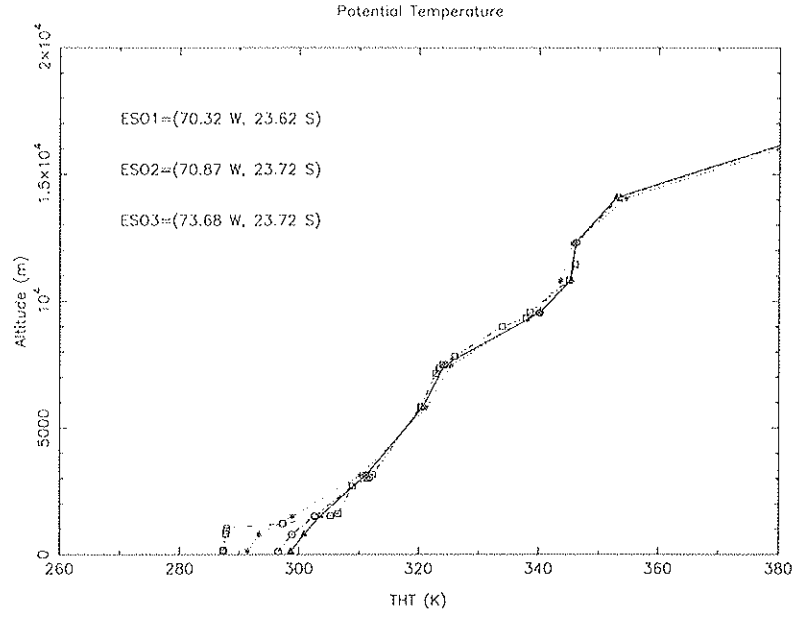


Figure 82: Potential temperature profiles issued from the ECMWF analysis extracted by grid points having the same latitude (-23.625) but different longitudes. ESO1 (triangle), ESO2 (cercle), ESO3 (star). Antofagasta radiosounding (square). It is well obvious as the profile over a grid point far over the sea (ESO3) better reconstructs the thermic inversion in the low part of the atmosphere.

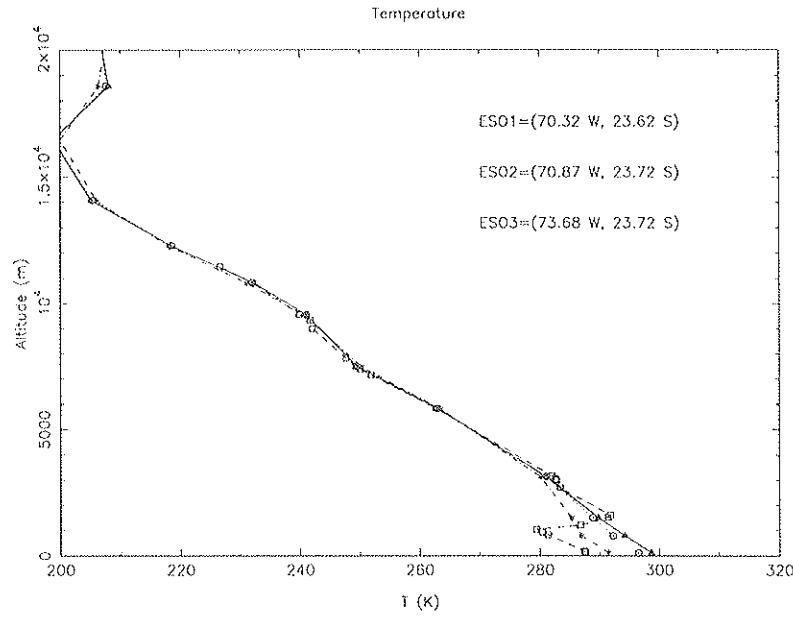


Figure 83: Absolute temperature profiles issued from ECMWF analysis extracted by different grid points. The same as Fig.(82)

SURF.(km)	Vert. Res. (m)	Horiz.Res. (m)	Sim. Time (sec)	Sample Time (sec)	CPU time (sec)	Price (Dm)
60 × 20	300	500 × 500	1800	2.5	4629	1388
60 × 20	600	500 × 500	1800	2.5	1945	583
60 × 20	300	1000 × 1000	1800	5	719	215
60 × 20	600	1000 × 1000	1800	5	296	88
60 × 60	300	500 × 500	1800	2.5	13219	3965
120 × 120	600	2000 × 2000	1800	10	400	120

Figure 84: Summary of price simulations related to different model configurations. The price reported in the last column is related to the listing price of the **Cray9000** (Meteo France) on September 1997. The comparison is made at the same simulation time (1800 sec).

ANNEX 4: Summary of the initialization used for the all night simulations

The nights are reported in the namelist `&NAM_LUNITn`. The variable CINEFILE has a general form `DddmVl`, where m = month and dd = day.

```

&NAM_REAL_PGD  CPGD_FILE='PODANDES9',
                LREAD_ZS = .TRUE.,      LREAD_ZOREL = .FALSE.,
                LREAD_ZOVEG = .TRUE.,    LREAD_RAD_PARAM = .TRUE.,
                LREAD_VEG_PARAM = .TRUE., LREAD_GROUND_PARAM = .TRUE. /
&NAM_DIMn_PRE  NIMAX=120, NCMAX=40, NKMAX=40 /
&NAM_CONF_PRE  MCARTESIAN=.FALSE., LBOUSS=.FALSE.,
                L2D=.TRUE., L1D=.FALSE.,
                CIDEAL='R300',
                LEPTURB=.FALSE., NVERB=5 /
&NAM_CONFn     LUSERV=.TRUE., NSV = 0 /
&NAM_GRID_PRE  XLAT0 = -24.61, XLON0 = -70.4,
                XRPK = 0., XBETA = 0. /
&NAM_GRIDn_PRE CGRID_TYPE = 'FUNCTN', XDZGRD=50., XDZTOP=600.,
                XZMAX_STRGRD=3000., XSTRGRD=30., XSTRTOP=0.,
                XLATCEN = -24.61, XLONCEN= -70.4 /
&NAM_LUNITn    CINIFILE='D145V1' /
&NAM_POST_PRE /
&NAM_DYNn_PRE /
&NAM_LBCn_PRE  CLBCX(1)='OPEN', CLBCX(2)='OPEN',
                CLBCY(1)='OPEN', CLBCY(2)='OPEN' /
&NAM_VPROP_PRE CTYPELOC='IJGRID', NILOC=20, NJLOC=20,
                CPUNU='ZZZ', CPUNV='ZZZ',
                LGEOSBAL=.TRUE. /
&NAM_Grn_PRE   CSORF='TSZ0', ZOREL=0.1, SST=284.2, XDTS=-1., XHUG=0.2 /
                1993      5      14      7200.00
'STANDARD'
140.
100200.
284.2
283.
14
100000.0      149.0662      2.215762
92500.00      133.5203      1.888624
85000.00      75.52237      1.280625
70000.      75.      13.
50000.      140.      12.
40000.      225.      7.
25000.      255.      62.
20000.      260.      40.
15000.00      270.3103      55.42081
10000.00      266.5624      30.53489
7000.000      269.1103      13.53163
5000.000      268.6082      11.53340
3000.000      280.5969      2.502639
1000.000      251.8718      3.440610
15
96700.      286.4      280.4
90800.      285.0      278.0
89700.      286.0      278.0
70000.      277.4      250.6
50000.      261.1      233.6
40000.      249.3      222.0
25000.      229.1      201.7
20000.00      219.6200      199.8603
15000.00      210.1900      196.6841
10000.00      203.4600      191.6616
7000.000      207.4900      189.5117
5000.000      209.7900      187.4943
3000.000      218.7300      184.3670
1000.000      233.4900      177.9153

```

```

&NAM_REAL_PGD CFQD_FILE='PGDANDES9',
               LREAD_ZS = .TRUE.,           LREAD_ZOREL = .FALSE.,
               LREAD_ZOVEG = .TRUE.,         LREAD_RAD_PARAM = .TRUE.,
               LREAD_VEG_PARAM = .TRUE.,     LREAD_GROUND_PARAM = .TRUE. /
&NAM_DIMn_PRE NIMAX=120, NJMAX=40, NKMAX=40 /
&NAM_CONF_PRE LCARTESIAN=.FALSE., LBOUSS=.FALSE.,
               L2D=.TRUE., L1D=.FALSE.,
               CIDEAL='RSOU',
               LPERTURB=.FALSE., NVERB=5 /
&NAM_CONFn LUSERV=.TRUE., NSV = 0 /
&NAM_GRID_PRE XLAT0 = -24.61, XLON0 = -70.4,
               XREF = 0., XBETA = 0. /
&NAM_GRIDn_PRE CZGRID_TYPE = 'FUNCTN', XZGRD=50., XDZTOP=600.,
               XZMAX_STRGRD=3000., XSTRGRD=30., XSTRTOP=0.,
               XLATCEN = -24.61, XLONCEN = -70.4 /
&NAM_LUNItH CINIPIFILE='D155V1' /
&NAM_POST_PRE /
&NAM_DYNn_PRE /
&NAM_LECn_PRE CLBCX(1)='OPEN', CLBCX(2)='OPEN',
               CLBCY(1)='OPEN', CLBCY(2)='OPEN' /
&NAM_VPROF_PRE CTYPELOC='IJGRID', NILOC=20, NJLOC=20,
               CPOND='ZZZ', CFUNV='ZZZ',
               LGEOSSAL=.TRUE. /
&NAM_GRn_PRE CSURF='TSZ0', ZOREL=0.1, SST=285.0, XDTS=-1., XHUG=0.2 /
1993          5          15 7200.00
'STANDARD'
140.
100200.
285.0
282.
27
100000.0      183.1358      3.425274
92500.00      186.5274      3.583532
85000.00      194.3552      2.333238
76300.      35.      9.
70000.      35.      9.
59000.      163.      6.
52100.      205.      9.
50000.      200.      10.
43600.      190.      15.
41000.      185.      14.
40000.      190.      14.
36400.      205.      14.
34300.      180.      12.
32700.      200.      16.
31700.      180.      16.
30500.      195.      18.
30000.      195.      18.
25000.      190.      19.
24100.      190.      19.
22800.      205.      21.
20000.00      247.4918      35.80470
15000.00      255.6195      36.69870
10000.00      255.0775      24.67120
7000.0000      249.9183      10.51886
5000.0000      302.4113      7.484818
3000.0000      337.8168      11.50413
1000.0000      30.25607      2.756175
30
98700.      286.4      281.9
93700.      284.0      282.8
92800.      283.6      281.5
91800.      285.4      282.1
90300.      288.2      271.2
87600.      292.6      266.9
85000.      292.6      254.1
84900.      292.6      254.1
84500.      292.4      254.0
70900.      281.6      238.9
50700.      265.5      218.4
50000.      264.5      233.5
49500.      263.9      247.1
49000.      263.1      216.9
41500.      254.1      211.1
40800.      250.7      223.1
37500.      246.3      211.1
33300.      241.5      207.8
30000.      234.3      211.7
27200.      227.7      211.0
25000.      223.9      204.4
21900.      218.9      195.9
20000.00      222.0200      200.8785
15000.00      207.5200      197.8870
10000.00      200.9400      191.8527
7000.0000      206.5100      189.5122
5000.0000      211.3100      187.4455
3000.0000      218.6900      184.3407
1000.0000      235.0300      178.7092

```

```

&NAM_REAL_PGD  CPGD_FILE='PGDANDES9',          LREAD_ZREL = .FALSE.,
                LREAD_Z9 = .TRUE.,              LREAD_ZOVEG = .TRUE.,
                LREAD_RAD_PARAM = .TRUE.,        LREAD_VEG_PARAM = .TRUE.,
                LREAD_GROUND_PARAM = .TRUE. /
&NAM_DIMn_PRE  NIMAX=120, NJMAX=40, NKMAX=40 /
&NAM_CONF_PRE  LCARTESIAN=.FALSE., LBOUSS=.FALSE.,
                LZD=.TRUE., LLD=.FALSE.,
                CIDEAL='RSOU',
                LPERTURB=.FALSE., NVERB=5 /
&NAM_CONFn     LUSERV=.TRUE., NSV = 0 /
&NAM_GRID_PRE  XLAT0 = -24.61, XLON0 = -70.4,
                XRPK = 0, XBETA = 0. /
&NAM_GRIDn_PRE CZGRID_TYPE = 'FUNCTN', XDZGRD=50., XDZTOP=600.,
                XZMAX_STRGRD=3000., XSTRGRD=30., XSTRTOP=0.,
                XLATCEN = -24.61, XLONCEN= -70.4 /
&NAM_LUNITH    CINIFILE='D165V1' /
&NAM_POST_PRE /
&NAM_DYNd_PRE  CLBCX(1)='OPEN', CLBCX(2)='OPEN',
                CLBCY(1)='OPEN', CLBCY(2)='OPEN' /
&NAM_VPROF_PRE CTYPLOC='IJGRID', NILOC=20, NJLOC=20,
                CFUNU='ZZZ', CFUNV='ZZZ',
                LGEOSBAL=.TRUE. /
&NAM_Grn_PRE   CSURF='TSZ0', ZOREL=0.1, SST=288.4, XDTS=-1., XHUG=0.2 /
1993           5           16       7200.00
'STANDARD'
140.
100400.
288.4
282.
28
100000.0      180.5334      2.970152
92500.00      178.5868      2.750891
85000.00      194.5630      1.229715
75700.        25.         10.
70000.        35.         7.
64900.        100.        3.
50000.        110.        4.
40000.        355.        4.
39700.        355.        4.
30000.        280.        8.
29500.        275.        8.
25000.        235.        16.
23800.        235.        22.
21500.        240.        35.
20000.        240.        36.
19100.        240.        37.
15800.        245.        33.
15000.        250.        27.
14200.        255.        24.
10000.        240.        21.
7440.         215.        4.
7000.         250.        2.
5000.         225.        5.
3310.         175.        4.
3000.         60.         3.
2480.         25.         10.
2000.         315.        6.
1950.         295.        7.
40
92500.        282.0      280.5
92000.        281.6      280.2
91500.        281.4      280.2
90000.        286.4      268.3
86900.        294.2      262.6
85000.        293.4      260.8
82600.        292.0      253.7
77900.        209.2      262.6
73200.        284.4      257.0
50000.        265.9      243.8
49400.        265.1      243.1
43100.        259.1      229.4
40000.        254.3      225.8
36600.        248.3      223.7
30000.        236.3      210.7
25600.        227.7      209.0
25000.        226.5      207.3
22600.        222.1      209.0
20000.        216.7      201.8
18000.        211.3      197.2
15000.        208.5      189.2
14300.        208.7      186.4
10300.        196.3      175.0
10000.        196.5      175.1
8570.         196.7      175.3
7560.         202.3      179.5
7000.         202.9      179.9
6500.         201.7      175.6
5100.         212.5      183.2
5000.         213.1      183.7
3540.         213.1      183.7
3330.         216.9      186.3
3030.         216.3      185.9
3000.         216.5      186.0
2640.         222.5      190.1
2020.         223.3      190.7
2000.         223.7      191.0
1900.         225.3      192.0
1000.         235.88     177.14

```

```

&NAM_REAL_PGD  CPGD_FILE='PGDANDES9',
                LREAD_ZS = .TRUE.,          LREAD_ZOREL = .FALSE.,
                LREAD_ZOVRG = .TRUE.,        LREAD_RAD_PARAM = .TRUE.,
                LREAD_VEG_PARAM = .TRUE.,    LREAD_GROUND_PARAM = .TRUE. /
&NAM_DIMn_PRE  NIMAX=120, NJMAX=40, NKMAX=40 /
&NAM_CONF_PRE  LCARTESIAN=.FALSE., LBOUSS=.FALSE.,
                LZD=.TRUE., LZID=.FALSE.,
                CIDEAL='RSOU',
                LPERTURE=.FALSE., NVERB=5 /
&NAM_CONFn     LUSERV=.TRUE., NSV = 0 /
&NAM_GRID_PRE  XLAT0 = -24.61, XLONG = -70.4,
                XREF = 0., XBETA = 0. /
&NAM_GRIDn_PRE CZGRID_TYPE = 'FUNCTN', XDZGRD=50., XDZTOP=600.,
                XZMAX_STRGRD=3000., XSTRGRD=30., XSTRTOP=0.,
                XLATCEN = -24.61, XLONCEN = -70.4 /
&NAM_LUNITn    CINIFILE='D17SV1' /
&NAM_POST_PRE  /
&NAM_DYNn_PRE  /
&NAM_LBCn_PRE  CLBCX(1)='OPEN', CLBCX(2)='OPEN',
                CLBCY(1)='OPEN', CLBCY(2)='OPEN' /
&NAM_VPROP_PRE CTYPELOC='IJGRID', NILOC=20, NJLOC=20,
                CFUNU='ZZZ', CFUNV='ZZZ',
                LGEOSBAL=.TRUE. /
&NAM_Grn_PRE   CSURF='TSZ0', ZOREL=0.1, SST=287.0, XDTS=-1., XHUG=0.2 /
1993           5           17       7200.00
'STANDARD'
140.
100300.
287.0
284.
15
100000.0       194.0616       2.175546
92500.00       189.9563       2.995480
85000.00       189.6228       3.276492
70000.         10.          11.
50000.         355.          8.
40000.         305.         10.
30000.         305.         19.
25000.         295.         24.
20000.         280.         41.
15000.         265.         28.
10000.00       280.4107       15.28131
7000.000       11.36668       6.977822
5000.000       351.5831       4.691023
3000.000       8.410797       13.33483
1000.000       16.27251       10.14840
33
100000.         286.6        283.6
95900.          283.2        282.4
95300.          283.0        282.2
93300.          292.2        265.0
92500.          295.6        266.8
91200.          297.0        267.0
85000.          294.0        250.5
80400.          290.0        264.8
75800.          288.6        253.0
70000.          283.6        243.2
69600.          283.0        242.8
50000.          266.3        228.3
43800.          257.9        222.4
40000.          252.9        210.3
32800.          241.7        207.9
30700.          238.3        223.4
30000.          236.7        225.8
28300.          232.7        225.6
27200.          229.9        222.8
26000.          227.5        220.6
25000.          226.1        212.1
24800.          225.5        209.7
20000.          218.5        199.1
15000.          208.7        189.3
13300.          203.1        185.9
10000.          201.3        183.4
8290.           198.5        180.1
7400.           201.1        180.6
7000.000        204.9600       189.5853
5000.000        210.1100       187.4803
3000.000        219.4300       184.3236
1000.000        235.7500       177.0780

```

```

&NAM_REAL_PGD  CPGD_FILE='PGDANDES9',
                LREAD_ZS = .TRUE.,      LREAD_ZOREL = .FALSE.,
                LREAD_ZOVEG = .TRUE.,    LREAD_RAD_PARAM = .TRUE.,
                LREAD_VEG_PARAM = .TRUE., LREAD_GROUND_PARAM = .TRUE. /
&NAM_DIMn_PRE  NIMAX=120, NJMAX=40, NKMAX=40 /
&NAM_CONF_PRE  LCARTESIAN=.FALSE., LBOUSS=.FALSE.,
                L2D=.TRUE., L1D=.FALSE.,
                CIDEAL='RSOU',
                LPERTURE=.FALSE., NVERB=5 /
&NAM_CONFn     LUSERV=.TRUE., NSV = 0 /
&NAM_GRID_PRE  XLAT0 = -24.61, XLON0 = -70.4,
                XRPK = 0., XBETA = 0. /
&NAM_GRIDn_PRE CZGRID_TYPE = 'FUNCTN', XDGGRD=50., XDZTOP=600.,
                XZMAX_STRGRD=3000., XSTRGRD=30., XSTRTOP=0.,
                XLATCEN = -24.61, XLONCEN = -70.4 /
&NAM_LUNITn    CINIFILE='D185V1' /
&NAM_POST_PRE  /
&NAM_DYNn_PRE  /
&NAM_LBCn_PRE  CLBCX(1)='OPEN', CLBCX(2)='OPEN',
                CLBCY(1)='OPEN', CLBCY(2)='OPEN' /
&NAM_VPROP_PRE CTYPELOC='IJGRID', NILOC=20, NJLOC=20,
                CFUNU='ZZZ', CFUNV='ZZZ',
                LGEOSBAL=.TRUE. /
&NAM_Grn_PRE   CSURF='TSZ0', ZOREL=0.1, SST=287.0, XDTs=-1., XHUG=0.2 /
1993           5           18       7200.00
'STANDARD'
140.
100200.
287.0
285.
15
100000.0      152.1342      0.7694154
92500.00      124.7735      1.192812
85000.00      122.2920      0.6741661
100200.      0.      0.
100000.      0.      0.
92500.      55.      2.
85000.      10.      3.
70000.      360.      13.
50000.      300.      0.
40000.      255.      7.
30000.      215.      17.
25000.      215.      16.
20000.      265.      24.
15000.      235.      21.
10000.      275.      18.
7000.      265.      9.
5000.000      214.7965      1.400893
3000.000      3.336700      9.496525
1000.000      333.2188      7.227039
22
100000.      286.8      284.3
93800.      283.0      281.9
93000.      282.6      281.7
92500.      284.6      280.5
91100.      291.4      265.2
88100.      297.0      263.6
85000.      294.6      267.8
78600.      288.8      264.6
70000.      284.2      240.7
54700.      272.5      239.4
50000.      266.1      242.4
45700.      259.5      240.4
40000.      253.3      225.1
34800.      247.3      206.7
30000.      238.9      208.8
27000.      231.7      209.6
25000.      227.5      205.2
22700.      222.1      199.8
20000.      218.9      195.9
15100.      212.1      183.0
15000.      211.9      182.8

```

```

&NAM_REAL_PGD  CPGD_FILE='PGDANDES9',
                LREAD_ZS = .TRUE.,      LREAD_ZOREL = .FALSE.,
                LREAD_ZOVEG = .TRUE.,    LREAD_RAD_PARAM = .TRUE.,
                LREAD_VEG_PARAM = .TRUE., LREAD_GROUND_PARAM = .TRUE. /
&NAM_DIMn_PRE  NIMAX=120, NIMAX=40, NKMAX=40 /
&NAM_CONF_PRE  LCARTESIAN=.FALSE., LBOUSS=.FALSE.,
                L2D=.TRUE., L1D=.FALSE.,
                CIDEAL='RSOU',
                LPERTURB=.FALSE., NVERB=5 /
&NAM_CONFn     LUSERV=.TRUE., NSV = 0 /
&NAM_GRID_PRE  XLAT0 = -24.61, XLON0 = -70.4,
                XRPK = 0., XBETA = 0. /
&NAM_GRIDn_PRE CZGRID_TYPE = 'FUNCTN', XZGRD=50., XZTOP=600.,
                XZMAX_STRGRD=3000., XSTRGRD=30., XSTRTOP=0.,
                XLATCEN = -24.61, XLONCEN = -70.4 /
&NAM_LUNITn    CINIFILE='D19SV1' /
&NAM_POST_PRE /
&NAM_DYNn_PRE /
&NAM_LECn_PRE  CLBCX(1)='OPEN', CLBCX(2)='OPEN',
                CLBCY(1)='OPEN', CLBCY(2)='OPEN' /
&NAM_VPROF_PRE CTYPELOC='IJGRID', NILOC=20, NJLOC=20,
                CFUNU='ZZZ', CFUNV='ZZZ',
                LGEOBAL=.TRUE. /
&NAM_Grn_PRE   CSURF='TSZ0', ZOREL=0.1, SST=288.8, XDTs=-1., XHUG=0.2 /
                1993      5      19      7200.00
'STANDARD'
140.
100300.
288.8
286.
18
100000.0      198.3020      1.875233
92500.00      160.8569      1.461095
85000.00      68.18753      0.2692582
70000.      340.      8.
67500.      345.      9.
58300.      305.      10.
50800.      305.      7.
50000.      300.      7.
40000.      275.      15.
36800.      270.      20.
32600.      280.      20.
30000.      280.      20.
26900.      270.      18.
25000.      265.      20.
20000.      255.      32.
19000.      260.      29.
17300.      255.      36.
25
100000.      288.8      283.8
99900.      288.8      282.7
93700.      284.6      281.3
87400.      291.6      272.8
85000.      293.4      269.7
70000.      282.0      256.8
68800.      281.0      254.3
59400.      277.4      241.1
50000.      267.3      244.2
48500.      265.3      242.5
45400.      262.9      235.0
40000.      255.5      232.3
30300.      238.7      220.7
30000.      238.3      220.4
25000.      228.7      212.9
22400.      223.3      206.1
20000.      217.9      199.5
16600.      210.1      191.5
15000.00      210.3400      192.4896
10000.00      197.8800      190.7564
7000.000      203.6700      189.6207
5000.000      212.6200      187.3716
3000.000      217.0200      184.3522
1000.000      234.6900      178.5343

```

```

&NAM_REAL_PGD CPGD_FILE='PGDANDES9',
LREAD_ZS = .TRUE., LREAD_ZOREL = .FALSE.,
LREAD_ZOVEG = .TRUE., LREAD_RAD_PARAM = .TRUE.,
LREAD_VEG_PARAM = .TRUE., LREAD_GROUND_PARAM = .TRUE. /
&NAM_DIMn_PRE NIMAX=120, NJMAX=40, NKMAX=40 /
&NAM_CONF_PRE LCARTESIAN=.FALSE., LBOUSS=.FALSE.,
L2D=.TRUE., L1D=.FALSE.,
CIDEAL='RSOU',
LPERTURB=.FALSE., NVERB=5 /
&NAM_CONFn LUSERV=.TRUE., NSV = 0 /
&NAM_GRID_PRE XLAT0 = -24.61, XLONG = -70.4,
XRPK = 0., XBETA = 0. /
&NAM_GRIDn_PRE CZGRID_TYDE = 'FUNCTN', XDZGRD=50., XDZTOP=600.,
XZMAX_STRGRD=3000., XSTRGRD=30., XSTRTOP=0.,
XLATCEN = -24.61, XLONCEN = -70.4 /
&NAM_LUNItN CINIPFILE='D235V1' /
&NAM_POST_PRE /
&NAM_DYNn_PRE /
&NAM_LBcN_PRE CLBCX(1)='OPEN', CLBCX(2)='OPEN',
CLBCY(1)='OPEN', CLBCY(2)='OPEN' /
&NAM_VPROF_PRE CTYPESLOC='IJGRID', NILOC=20, NJLOC=20,
CFUNU='ZZZ', CFUNV='ZZZ',
LGEOSBAL=.TRUE. /
&NAM_Grn_PRE CSURF='TSZ0', ZOREL=0.1, SST=288.0, XDTS=-1., XHUG=0.2 /
1993 5 23 43200.00
'STANDARD'
140.
100000.
288.0
285.
26
100000.0 186.7591 2.195450
92500.00 183.2337 2.273719
85000.00 186.9744 1.309809
61500. 335. 7.
50900. 280. 10.
50000. 280. 10.
48500. 285. 10.
42100. 260. 17.
40000. 265. 19.
30100. 295. 26.
30000. 295. 26.
25000. 285. 34.
20300. 280. 44.
20000. 280. 43.
15200. 275. 43.
15000. 275. 43.
12900. 260. 28.
12500. 265. 21.
11800. 265. 25.
10800. 285. 20.
10000. 285. 20.
7000.000 279.1008 11.57557
5000.000 250.4962 5.304046
3000.000 235.2493 10.51331
1000.000 255.9566 14.18348
28
92500. 282.2 281.3
89400. 280.6 280.0
85600. 289.4 271.4
85200. 289.8 271.7
85000. 289.8 271.7
80900. 289.4 261.0
72300. 282.4 254.5
70500. 283.0 235.8
56000. 269.7 230.7
52900. 268.3 220.2
50000. 264.9 218.0
41500. 251.9 231.6
40000. 250.1 230.1
31800. 236.3 222.5
30000. 233.7 216.5
26200. 226.3 213.4
25000. 224.9 211.0
22800. 224.5 200.2
20000. 220.5 192.8
15000. 209.7 185.0
10000. 200.3 174.7
8750. 198.7 176.8
8090. 200.3 174.7
7000.000 206.0900 189.5749
5000.000 210.6800 187.4411
3000.000 217.2700 184.3616
1000.000 233.8500 178.1012

```



```

&NAM_REAL_PGD  CPGD_FILE='PGDANDES9',
                LREAD_ZS = .TRUE.,          LREAD_ZOREL = .FALSE.,
                LREAD_ZOVEG = .TRUE.,        LREAD_RAD_PARAM = .TRUE.,
                LREAD_VEG_PARAM = .TRUE.,    LREAD_GROUND_PARAM = .TRUE. /
&NAM_DIMn_PRE  NIMAX=120, NJMAX=40, NKMAX=40 /
&NAM_CONF_PRE  LCARTESIAN=.FALSE., LBOUSS=.FALSE.,
                L2D=.FALSE., L1D=.FALSE.,
                CIDEAL='RSOU',
                LPERTURB=.FALSE., NVERB=5 /
&NAM_CONFn     LUSERV=.TRUE., NSV = 0 /
&NAM_GRID_PRE  XLAT0 = -24.61, XLON0 = -70.4,
                XRPK = 0., XBETA = 0. /
&NAM_GRIDn_PRE CZGRID_TYPE = 'FUNCTN', XZGRD=50., XDZTOP=600.,
                XZMAX_STRGRD=3000., XSTRGRD=30., XSTRTOP=0.,
                XLATCEN = -24.61, XLONCEN = -70.4 /
&NAM_LUNITn    CINIFILE='D255V1' /
&NAM_POST_PRE /
&NAM_DYNn_PRE /
&NAM_LBCn_PRE  CLBCX(1)='OPEN', CLBCX(2)='OPEN',
                CLBCY(1)='OPEN', CLBCY(2)='OPEN' /
&NAM_VPROP_PRE CTYPELOC='IJGRID', NILOC=20, NJLOC=20,
                CFUNU='ZZZ', CFUNV='ZZZ',
                LGROSHAL=.TRUE. /
&NAM_Grn_PRE   CSURF='TSZ0', ZOREL=0.1, SST=287.6, XDTS=-1., XBUG=0.2 /
1993           5           25       7200.00
'STANDARD'
140.
100400.
287.6
281.
15
100000.0      133.2595      1.839348
92500.00      113.0573      1.966977
85000.00      67.94540      1.758551
70000.      20.      4.
50000.      295.      13.
40000.      295.      20.
30000.      290.      48.
25000.      285.      52.
20000.00      280.0036      45.01442
15000.00      281.4201      43.05149
10000.00      280.7964      24.46257
7000.000      266.6691      10.84831
5000.000      287.8116      7.162995
3000.000      298.4471      8.233104
1000.000      284.1691      23.21557
20
92500.      281.4      279.9
91200.      280.4      280.0
90000.      279.4      279.3
88200.      286.8      268.7
85000.      291.4      266.7
84200.      291.8      265.5
74000.      283.4      258.7
71400.      282.8      245.0
70900.      282.6      244.9
70000.      282.0      244.5
50000.      262.7      239.7
42000.      251.9      240.0
40700.      250.1      236.0
40000.      249.3      235.3
38300.      247.7      226.8
32500.      242.1      221.5
31000.      241.7      221.9
30000.      239.9      221.1
25000.      232.1      210.9
22800.      226.7      212.6
20000.00      219.2000      213.0090
15000.00      207.5700      201.8898
10000.00      201.2600      191.7445
7000.000      204.8600      189.5802
5000.000      207.6600      187.5717
3000.000      217.3800      184.3544
1000.000      233.4800      177.9101

```